Open-Closed Magnetic Field Line Boundary Identification Using Directional Derivatives of SuperDARN Convection Flow

by

SNM Azizul Hoque

A thesis submitted in partial fulfillment of the requirements for the degree of

Doctor of Philosophy

Department of Physics

University of Alberta

Abstract

This thesis is a case study analysis to better understand magnetospheric dynamics and in particular dynamics of the open-closed magnetic field line boundary (OCB). The directional derivatives of ionospheric convection flow speed are measured along streamlines using SuperDARN HF radar to determine the open-closed magnetic field line boundary (OCB). It is found that the peak in the directional derivative of SuperDARN flow along a flow streamline may be associated with magnetic reconnection between open and closed field lines and thus is a signature of the OCB.In the first case study, the peak in the directional derivative of SuperDARN flow is compared in all magnetic local time sectors with other OCB proxies such as ultra-violet auroral emission boundaries and particle precipitation boundaries during the southward interplanetary magnetic field condition. The OCB proxy determined with the the directional derivative of SuperDARN flow is found to be consistent with other OCB proxies during the interval. In the second case study, the proposed technique is further evaluated during two different substorm events, with each event interval lasting two hours. The latitudinal locations of the peak in the directional derivative of SuperDARN flow are in agreement with the spectrographic imagers poleward boundaries of ultra-violet emissions in the dawn and dusk sectors during the substorm intervals. In the final part of the thesis, multiple peaks in the

directional derivative of flow during the substorm interval are examined and compared with ultraviolet detectors in the midnight sector. The occurrence of multiple flow peaks in the directional derivative of flow depends on the convection cell pattern which in turn depends upon the IMF B_y condition. The result indicates that the secondary peaks agree with the ultraviolet measurements in the midnight sector. Therefore, SuperDARN convection flow directional derivatives might be useful for determining the OCB globally.

Dedicated to my mentor

Dr. A. H. Moinuddin Ahmed SIRE

Acknowledgements

I would like to thank my supervisor Dr. Frances Fenrich for offering me the opportunity to study in the Space Physics Group. I am very much grateful to her for providing expenses to attend international conferences and meetings. She was always ready to help me on all kinds of questions and curiosities. Its a great honor for me to work with her as a graduate student. I would like to extend my thanks to members of my supervisory committee Dr. Richard Marchand and Dr. Kim Chow and as well as my external examiner Dr. Kathryn McWilliams for their careful examination of my thesis and their useful comments. I would like to give special thanks to Sarah Derr, graduate program assistant, for all her help during my PhD. My family always have given me wonderful thoughts during my research. I am grateful to my mother, Nurun Naher, and my knowledgeable father, Dr. Aminul Hoque, for supporting me during my research. Words cannot express the thanks I owe my wife, Sabrina, and my daughter, Ishana, for all the sacrifices they have made for me. I also need to thank Sohel Bhuiyan, my colleague, for providing useful knowledge on MATLAB codes and Latex formatting of my thesis. I gratefully acknowledge the University of Alberta and the Natural Sciences and Engineering Research Council of Canada for providing my financial support.

Contents

List of Tables

List of Figures

List of Symbols and Abbreviations

ACE	Advanced Composition Explorer
ACF	Autocorrelation Function
$\overrightarrow{B}$	Magnetic Field Vector
CARISMA	Canadian Array for Realtime Investigations of Magnetic Activity
CDF	Common Data Format
Δf	Doppler frequency shift of Radar Backscatter
DMSP	Defense Meteorological Satellite Program
$\overrightarrow{E}$	Electric Field Vector
$\overrightarrow{E}_{\parallel}$	Parallel Electric Field
$\overrightarrow{E}_{\perp}$	Perpendicular Electric Field
ε_0	Dielectric Constant in Vacuum
$\overrightarrow{F}$	Force
FAC	Field Aligned Current
FFT	Fast Fourier Transformation
FUV	Far Ultraviolet
FWHM	Full Width Half Maximum
HF	High Frequency
IDL	Interactive Data Language
IMAGE	Imager for Magnetopause-to-Aurora Global Exploration
IMF	Interplanetary Magnetic Field
ISEE	International Sun/Earth Explorer Spacecraft
$\overrightarrow{J}$	Current Density
K_B	Boltzman constant
$\overrightarrow{k_s}$	Wave Number of the Scattered Wave
$\overrightarrow{k_t}$	Wave Number of the Transmitted Wave

LBH	Lyman-Birge-Hopfield
λ_D	Debye Length
λ_r	Radar Operating Wavelength
MFE	Magnetic Field Experiment
MHD	Magnetohydrodynamic
MLAT	Magnetic Latitude
MLT	Magnetic Local Time
μ_0	Magnetic Permeability of Free Space
N_D	Debay Sphere
n_e	Electron Density
OCB	Open Closed Magnetic Field Line Boundary
PAPB	Poleward Auroral Precipitation Boundaries
ϕ	Magnetic Flux
Φ	Electrostatic Potential
POLAR	Polar Orbiting ISTP Spacecraft
PPB	Particle Precipitation Boundary
ρ	Net Charge Density
R_e	1 Earth Radius
R_m	Magnetic Reynolds Number
SI	Spectral Imager
σ_H	Hall Conductivity
σ_P	Hall Conductivity
$\sigma_\parallel$	Parallel Conductivity
STARE	Scandinavian Twin Auroral Radar Experiment
SuperDARN	Super Dual Auroral Radar Network
SWB	Spectral Width Boundary
T	Temperature
UT	Universal Time
UVI	Ultra Violet Imager
$\overrightarrow{v}$	Particle velocity
V	Speed of Plasma Flow
V_A	Alfvén speed
V_D	Doppler Velocity Plasma Drift
WIC	Wideband Imager Camera

Chapter 1

Introduction

1.1 Preliminary Remarks

The relation between the Sun and the terrestrial magnetic field was recognized about a century ago [3]. One property of the Sun is the solar wind, the ionized and magnetized gas flowing from the Sun with typical speeds of $\sim$ 500 km/s. Energy is transported into the Earth's magnetosphere due to the interaction of the solar wind with the magnetosphere. One way in which this energy is transferred is via magnetic reconnection as the interplanetary magnetic field carried by the solar wind meets the Earth's magnetic field on the dayside of the magnetosphere. In this process, terrestrial closed field lines become open to the solar wind and are convected into the Earth's nightside where they reconnect to become closed field lines again. The boundary between the open and closed magnetic field lines is known as the open-closed field line boundary (OCB) and this boundary separates the polar cap from the auroral zone. Thus it is important to know where the open-closed boundary is to understand magnetospheric dynamics and the process of energy transportation from the solar wind to the magnetosphere. A number of techniques have been developed to identify the open-closed magnetic field boundary; they will be discussed at the end of Chapter 2.

A basic knowledge of magnetospheric physics can be acquired in text books such as Baumjohann and Treumann (1997) [4] and Kivelson and Russell (1995) [3]. The remaining sections in the introduction consist of the necessary background and theory related to the thesis topic. Here the basic concepts of space physics, the ionosphere, and the magnetosphere are introduced. Reconnection and substorms are important phenomena related to the topic of the thesis and will be discussed at the end of this chapter.

This thesis investigates and evaluates a new technique for identifying the open-closed field line boundary. The technique utilizes directional derivatives of the convection flow speed as measured by ground-based coherent scatter high frequency (HF) radars such as the Super Dual Auroral Radar Network (SuperDARN), which will be discussed in Chapter 2. In Chapter 3 the proposed technique is tested with existing OCB proxies during a steady southward IMF interval. In Chapter 4 the proposed technique is evaluated under variable solar wind conditions during auroral substorm events. The occurrences of multiple peaks in the directional derivative of flow are examined in Chapters 5. The conclusions of these investigations are discussed in Chapter 6 and some future directions for this research are suggested.

1.2 Background and Theory

1.2.1 Basic Definitions and Concepts

The concept of an open-closed magnetic field line boundary is related to the solar wind, the magnetosphere, and the ionosphere. Therefore, the basic concepts of these three regions are presented here. Figure 1.1 is a schematic of

Earths magnetosphere showing currents, fields, and plasma regions.

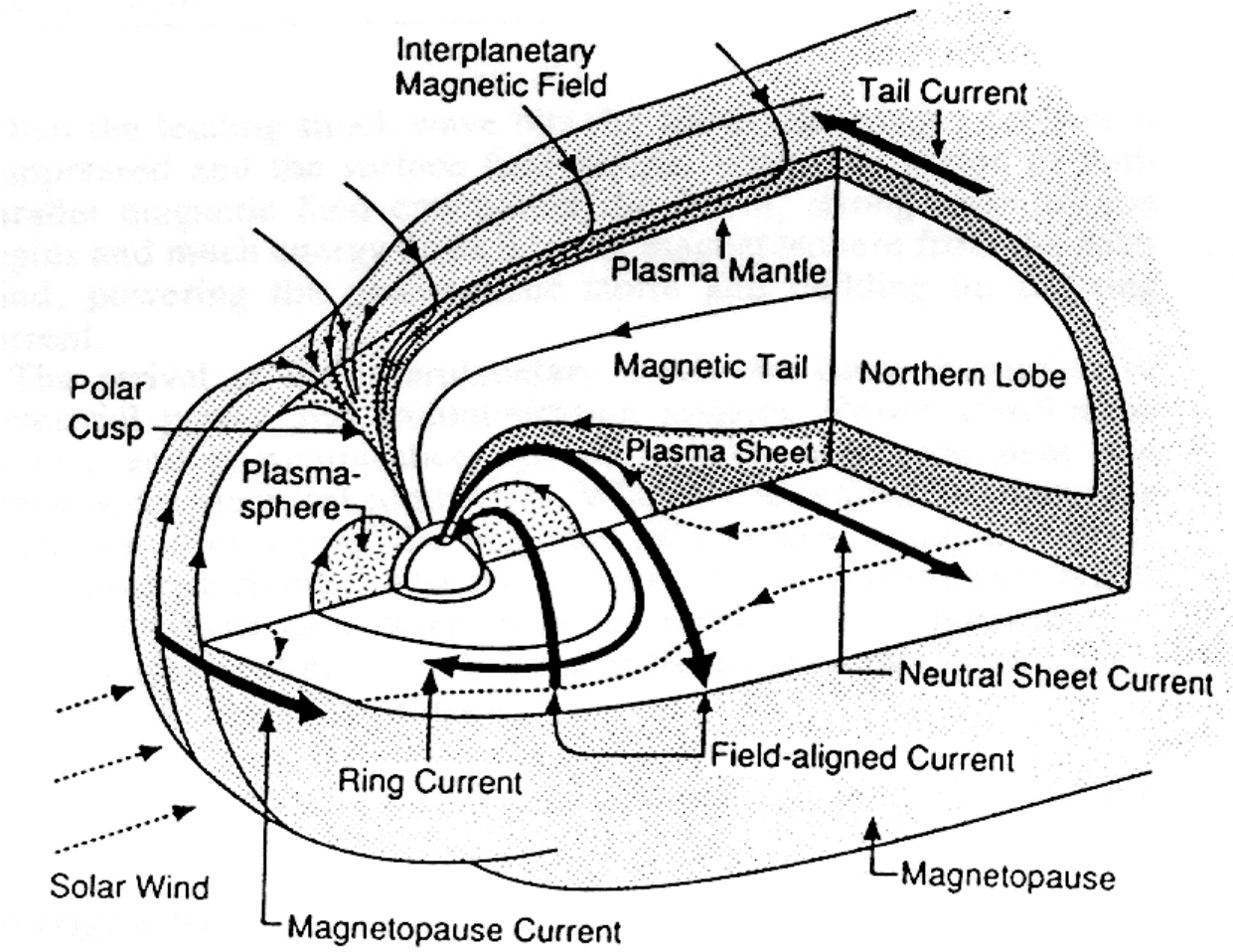

Figure 1.1: Three dimensional cutaway view of Earth's magnetosphere [1].

1.2.1.1 The Solar Wind

The existence of the solar wind was first proposed by E. Parker (1958) [5]. Solar wind is a high speed particle stream composed of mostly electrons and protons which continuously blows out from the Sun's outer atmosphere, the corona, into interplanetary space. The solar wind carries with it the solar magnetic field which is known as the interplanetary magnetic field (IMF). The

IMF is frozen into the solar wind as it follows the ideal magnetohydrodynamic (MHD) fluid treatment [6]. At the Earth, the IMF has a typical magnitude of $\sim$ 5 nT and varies in direction. When the solar wind hits the terrestrial magnetic field, it cannot pass through, and is slowed down and deflected [7]. The region where the solar wind impacts the magnetosphere is called the bow shock region. Solar wind can penetrate the Earth's magnetic field by a process called magnetic reconnection that will be discussed in section 1.3.

1.2.1.2 The Magnetosphere

Earth has a dipolar magnetic field. Due to interaction with the solar wind, the Earth's magnetic field is compressed on the dayside and extended on the nightside [8]; [9]. On the dayside, a typical distance of the magnetopause from the center of the Earth is 9-11 R_e [10] whereas the magnetosphere extends beyond 1000 R_e on the nightside [11]. There are four main current systems in the magnetosphere: the magnetopause current, the ring current, the tail and neutral sheet current, and the field aligned current. Earth's magnetic field and plasma pressure from the solar wind creates the magnetopause current across the dayside magnetopause. The ring current flows westward around the Earth in the inner magnetosphere due to the differential drifts of ions and electrons. The tail current flows across the magnetopause on the nightside from dusk to dawn and then it is closed via the neutral current which flows from dawn to dusk in the equatorial plane. The field aligned current flows along the magnetic field which connects the polar ionosphere directly to the magnetospheric current system.

The plasma in the magnetosphere is comprised of electrons, protons, and small fractions of He^+ and O^+ ions. The Earth's plasma environment is not the same inside the magnetosphere, it is subdivided into different regions based on the plasma and magnetic field characteristics. The magnetosheath is the region

outside of the magnetosphere between the bow shock and the magnetopause. The plasma sheet is the region of the magnetosphere where most of the magnetotail plasma is concentrated. Field lines threading the plasma sheet map to the auroral zone because energized plasma sheet particles are able to precipitate into the ionosphere creating luminous auroral displays. The outer high latitude portion of the magnetotail is the magnetotail lobe, where the plasma density is very much reduced. Near to Earth, at a distance of 2.5–7.0 R_e, which depends on the geomagnetic activity [12], a region called the plasmasphere overlaps the Van Allen radiation belt on dipolar field lines. The plasmasphere corotates with the Earth and reaches its outer boundary, the plasmapause. The Van Allen radiation belt consists of trapped high-energy ion and relativistic (electrons reach speeds greater than 0.86 of the speed of light) electron plasma.

The morphology of the magnetosphere is greatly affected by the interplanetary field. If the interplanetary magnetic field (IMF) has a negative B_z component, then magnetic merging occurs on the dayside of the Earth creating open field lines, i.e., field lines that have one footprint on the Earth and one footprint in the solar wind. During periods of an open magnetic field configuration, plasma and magnetic flux from the solar wind transport mass, momentum, and energy into the magnetotail. The release of energy from a highly energized state to a more relaxed state produces a wide range of energetic phenomena such as substorms, trapped particles, and energetic plasma precipitation into the atmosphere. Note that other solar wind IMF conditions such as northward IMF and B_y dominated IMF also result in magnetic merging at the magnetopause and can transport mass, momentum and energy into the magnetosphere. However, the coupling between the solar wind and the magnetosphere is much less during these IMF conditions than during southward IMF and do not result in a substorm.

1.2.1.3 The Ionosphere

The ionosphere begins at $\sim$ 80–90 km above the Earth's surface. It is the atmospheric region where sufficient ionization can exist due to a decrease in collisions between particles. Solar ultraviolet radiation and energetic particle precipitation from the magnetosphere creates the ionization. Negative ion formation (electrons attach to neutral atoms) and recombination (between positive ions and electrons) reduce ionization, keeping the system in equilibrium.

The ionosphere has three distinct layers of variable thickness, with different electron/ion concentrations-the D (60–90 km), E (90–140 km) and F layers. The maximum ionization occurs in the F region which is subdivided into two regions during the daytime. The F1 layer extends from 140 to 210 km and the F2 layer from 210 to 1000 km altitude. The F1 and F2 layers merge and become a single F region at night. The F2-region contains the densest plasma in the Earth's environment with an electron density up to 10^6 cm^{-3}. The above values are taken from Baumjohann and Treumann (1997) [4].

Birkeland currents are field aligned currents (FAC) that flow along the magnetic field lines connecting the magnetosphere to the ionosphere. Currents in the E-region ionosphere also flow perpendicular to the magnetic field. Current that flows parallel to the electric field are called Pederson currents and current that flows perpendicular to both electric and magnetic fields in the direction of $-\overrightarrow{E}\times\overrightarrow{B}$ are called Hall currents. Using Ohms law, the current in the ionosphere is:

$$\overrightarrow{J} = \sigma_P \overrightarrow{E}_{\perp} - \sigma_H \left(\overrightarrow{E} \times \overrightarrow{B}\right)/B + \sigma_{\parallel} \overrightarrow{E}_{\parallel},$$

where σ_H, σ_P, and $\sigma_{\parallel}$ are the Hall, Pederson, and parallel conductivities, respectively. In the E-region ions are slower than electrons in their $\overrightarrow{E}\times\overrightarrow{B}$ drift because of collisions with neutral particles and other ions resulting in the Hall

and Pederson currents. At higher altitudes where the ion-neutral collision frequency is low, no perpendicular currents are produced as the ions and electrons $\overrightarrow{E} \times \overrightarrow{B}$ drift in the same direction.

Because of its high electron density, the ionosphere is very important for high frequency coherent scatter radars such as SuperDARN. Using the refraction and reflection property of HF radars, plasma properties in the ionospheric F and E regions can be studied. However, the electron density in the F region is much higher than in the E region, hence, refraction occurs mostly in the F region [13]. The F region is the collisionless region as the air density is lower than that of other regions in the ionosphere, and free electrons and ions cannot recombine readily.

1.2.1.4 Plasmas in Space

The solar wind, magnetosphere, and ionosphere are entirely composed of plasma. Plasma is an ionized gas which has equal numbers of positive and negative charged particles and, therefore, on average is quasi-neutral. Quasi-neutrality is the first criterion for defining a plasma. The plasma density must be sufficiently low so that the short range collision will be negligible while at the same time the total number of particles should be large enough to behave in a collective manner (comprising a system). In such a case, long range Coulomb interactions are dominant. The force range of a charged particle is the Debye length $\lambda_{D:}$

$$\lambda_D = \left(\frac{K_B T \varepsilon_0}{n_e e^2} \right)^{\frac{1}{2}}. \tag{1.1}$$

where ε_0 is the dielectric constant of free space and K_B is the Boltzman constant. T, e, and n_e represent temperature, charge, and electron density, respectively. Hence, the potential around a point charge is screened out by oppositely

charge particles when the radius r > λ_D. To fulfill the condition for a collective shielding effect, a characteristic scale variation L for macroscopic parameters must be larger than the Debye length λ_D:

$$L \gg \lambda_D. \tag{1.2}$$

To fulfill the condition of collective behavior of plasma, a sufficient number of particles need to be present inside the sphere considered, called the Debye sphere,

$$N_D = \frac{4\pi}{3} n_e \lambda_D^3, \tag{1.3}$$

where N_D is the plasma parameter.

Equation 1.3 leads to the second criterion of plasma behavior. This can be used to define a third criterion which is related to the frequency of short-range collisions between charged particles. According to the third criterion, the electron plasma frequency is much greater than the electron-neutral collision frequency. Combining equations 1.1 and 1.3 yields:

$$N_D \sim \left(\frac{n_e}{T^3}\right)^{-\frac{1}{2}}, \tag{1.4}$$

which states that the collisions decrease with increasing temperature and decreasing density. This leads to the statement that if plasma is disturbed by an external influence, electrons, being lighter than other charged particles, tend to neutralize the medium of ionized gas. The solar wind and magnetosphere are collisionless systems as plasma in these regions have low density and high temperature. The ionospheric E-region and regions below have high plasma densities relative to the solar wind and the magnetosphere, hence, they are collision regions. The conductivity parallel to the magnetic field increases strongly with altitude due to decreasing collisions with neutral gas. The F region is considered to have infinite conductivity with no collisions as the density of neutral

gas is negligible. It is worthwhile to note that the magnetic field lines can be considered to be equipotential to the electric field, as conductivity parallel to the magnetic field is much higher than the conductivity perpendicular to the magnetic field.

1.2.2 Theoretical Approaches

Typically the dynamics of a plasma system are described with one of four different approaches. The single particle approach is the easiest approach but the solution of the equation of motion does not consider the internal field from other charged particles in motion. However, this approximation is useful for describing the dynamics of low density plasma. In the one-fluid magnetohydrodynamic (MHD) approach, plasma is considered to be a conducting fluid rather than a system of individual particles, thus, the macroscopic behavior of the plasma is considered and electromagnetic effects are taken into account. In the multi-fluid MHD approach, different particle species are considered as a single fluid permitting the study of heavy and light particles (e.g., ions and electrons). MHD theory has some limitations when the plasma is considered to be collisionless. These limitations can be overcome by assuming the plasma conductivity is nearly infinite. Highly conducting fluids are ideally suited to the MHD approximation. In the fourth approach, the kinetic theory of plasma, a distribution function of identical particles is studied in phase space. This approach is the most complex of the four approaches. In this section, the first two approaches will be used to describe plasma dynamics.

An ideal MHD conducting plasma fluid follows energy conservation laws as well as electromagnetic theory. Maxwells equations and the Lorentz force law are used here to explore the behaviour of electromagnetic fields in plasma.

If an electric field, $\overrightarrow{E}$, and a magnetic field, $\overrightarrow{B}$, act on a particle with charge q

and velocity $\overrightarrow{v}$, the particle experiences a force $\overrightarrow{F}$:

$$\overrightarrow{F} = q\overrightarrow{E} + q(\overrightarrow{v} \times \overrightarrow{B}), \tag{1.5}$$

where $q\overrightarrow{E}$ is the Coulomb force and the second term on the right is the Lorentz force.

1.2.2.1 Maxwells Equations

According to Faraday's law, a time varying magnetic field and a space varying electric field are related by:

$$\nabla \times \overrightarrow{E} = -\frac{\partial \overrightarrow{B}}{\partial t}. \tag{1.6}$$

This equation tells us that the change in magnetic field drives an electromotive force through a coiled wire.

The relation between a magnetic field, the electric field and the current density $\overrightarrow{J}$ is:

$$\nabla \times \overrightarrow{B} = \mu_0 \overrightarrow{J} + \mu_0 \varepsilon_0 \frac{\partial \overrightarrow{E}}{\partial t}, \tag{1.7}$$

Where μ_0 and ε_0 are the magnetic permeability of free space and dielectric constant in a vacuum, respectively.

According to the low frequency approximation for an ideal MHD fluid, displacement current is neglected. Equation 1.7 then reduces to the familiar Ampère law:

$$\nabla \times \overrightarrow{B} = \mu_0 \overrightarrow{J}. \tag{1.8}$$

The electric field obeys Poisson's equation:

$$\nabla . \overrightarrow{E} = \rho/\varepsilon_0, \tag{1.9}$$

where ρ is the net charge density.

The absence of magnetic monopoles is governed by the following equation:

$$\nabla . \overrightarrow{B} = 0. \tag{1.10}$$

1.2.2.2 Biot-Savart Law

The Biot-Savart law can be expressed as:

$$d\overrightarrow{B} = \frac{\mu_o I d\overrightarrow{s} \times \hat{r}}{4\pi r^2} \tag{1.11}$$

Where $d\overrightarrow{s}$ is infinitesimal length of conductor carrying electric current I and and $\hat{r}$ is the unit vector to specify the direction of the vector distance r from the current to the magnetic field point. The magnetic field in the magnetotail lobes and the neutral sheet current are related by the Biot-Savart's law.

1.2.2.3 Diffusion and Frozen Flux

If the plasma moves with velocity $\overrightarrow{v}$ across the magnetic field, the current density according to Ohm's law is:

$$\overrightarrow{J} = \sigma_0(\overrightarrow{E} + \overrightarrow{v} \times \overrightarrow{B}) \tag{1.12}$$

From Faraday's law and Ohm's law,

$$\frac{\partial \overrightarrow{B}}{\partial t} = \nabla \times (\overrightarrow{v} \times \overrightarrow{B}) + \frac{1}{\mu_o \sigma_0} \nabla^2 \overrightarrow{B}. \tag{1.13}$$

Equation 1.13 describes the change in magnetic field due to convection and diffusion. $\nabla \times (\overrightarrow{v} \times \overrightarrow{B})$ represents the change in the field due to convection

and $\frac{1}{\mu_o \sigma_0} \nabla^2 \overrightarrow{B}$ refers to the 'magnetic diffusion.' When the second term on the right side of equation 1.13 is dominant, the equation becomes a diffusion equation. During the diffusion process, field lines overlap with other field lines and join together vectorially, and the total structure of the magnetic field changes. Therefore, there is no coupling between the magnetic field and the plasma flow. If the plasma is in motion with infinite conductivity, Ohm's law from equation 1.12 becomes:

$$\overrightarrow{E} = -\overrightarrow{v} \times \overrightarrow{B} \tag{1.14}$$

For parallel and perpendicular components, equation 1.14 becomes:

$$\overrightarrow{E_\perp} = -\overrightarrow{v} \times \overrightarrow{B} \tag{1.15}$$

$$\overrightarrow{E_\parallel} = 0 \tag{1.16}$$

Equations 1.15 and 1.16 imply that an infinitely conducting plasma will flow such that the electric field in the rest frame of the plasma is zero. Therefore, the plasma does not move relative to the field and the field is frozen-in.

The magnitude ratio of the first and second terms of equation 1.13 is defined as the magnetic Reynolds number; it determines whether the medium is diffusion dominated or flow dominated. The magnetic Reynolds number R_m can be expressed as:

$$R_m = \frac{\left| \nabla \times \left(\overrightarrow{v} \times \overrightarrow{B} \right) \right|}{\left| \frac{1}{\mu_0 \sigma_0} \left(\nabla^2 \overrightarrow{B} \right) \right|} = \mu_0 \sigma_0 L V, \tag{1.17}$$

Where the Reynolds number is proportional to the conductivity σ_0, the velocity $\overrightarrow{v}$, and the length scale L. When the Reynolds number is high, the diffusion term can be neglected and the frozen-in flow prevails. For the solar wind, where

the field and plasma flow together, the Reynolds number is high ($\sim 7{\times}10^{16}$), considering L is the overall size of the plasma system and hence negligible diffusion takes place. On the other hand, diffusion dominates in a local region of magnetic field reversal, or a current sheet where the characteristic length related to the magnetic field is small. From the diffusion equation, the time scale for diffusion is $t_d = L^2\mu_0\sigma_0$. When the time-scale for the removal of the field line from the locality, $t_A = L/V_A$ (where $V_A = \frac{B}{\sqrt{\mu_o\rho}}$ is the Alfvén speed), is comparable with t_d, the frozen-in flux concept becomes locally invalid and R≈1. During the diffusion process, the magnetic field is no longer frozen-in and plasma can freely stream across the magnetic field inside the diffusion region, while outside the region, the frozen-in field concept generally holds.

1.3 Concept of Magnetic Reconnection

Frozen-in flux and diffusion are equally important during the process of magnetic merging. If antiparallel field lines are frozen into the plasma and both plasma and field lines move toward the current sheet that separates them, then the magnetic field may vanish at the centre due to diffusion at the point where the Reynolds number is equal to or close to one. The outflowing plasma is transported from the newly reconnected region. The center of the point of diffusion is called a magnetic neutral point. The reconnection process continues as long as oppositely directed flux tubes are pushed toward each other.

1.3.1 Plasma Convection in the Magnetosphere and the Ionosphere

Magnetic reconnection is one of the primary drivers of convection, therefore, the change in convection measured by the HF SuperDARN radar can determine where reconnection is occurring and can determine the location of the open-closed boundary, to be discussed in section 1.3.2 and in Chapter 2. The

concurrent motion of plasma and frozen-in field lines is called convection. In other words, convection is due to the $\overrightarrow{E} \times \overrightarrow{B}$ drift of ions and electrons which eventually moves the plasma which in turn moves the field lines because they are frozen-in. In the outer magnetosphere, plasma and field line motions are driven by the kinetic energy of the solar wind. Convection in the magnetosphere is mirrored in the ionosphere except near regions of field aligned current, because if there is no field aligned current the field lines are equipotential and thus electric fields in the magnetosphere are mirrored in the ionosphere and these electric fields drive the $\overrightarrow{E} \times \overrightarrow{B}$ convection. The F-region can be considered collision free with infinite conductivity and in most of the E-region the electrons are collisionless and $\overrightarrow{E} \times \overrightarrow{B}$ drift of electrons occurs as in the F-region. But convection in ionospheric lower altitudes is not same as in the magnetosphere because the region is dominated by collisions of charged particles with neutral particles.

1.3.2 Magnetospheric Dynamics and the Open-Closed Field Line Boundary (OCB)

By the process of magnetic reconnection, energy and momentum are transferred from the solar wind to the magnetosphere [14]. When solar wind with a southward IMF hits the earths magnetopause, magnetic merging between the IMF and the terrestrial magnetic field occurs, as illustrated schematically in Figure 1.2. Reconnection occurs at the field line labeled 1 where the geomagnetic field line attached to the earth is now reconnected with the interplanetary field line. The reconnected open magnetic field lines (denoted by 2–5) will be pulled by the solar-wind antisunward and the associated plasma is convected over the polar region until magnetic reconnection occurs at the nightside of the Earth where the two field lines meet again (denoted by 6). The reconnected field lines are transported back to the frontside of the magnetosphere (toward

the sunward direction). The circulation of the magnetic field lines in the southward IMF produces a two-cell pattern at the Earth's polar cap (Figure 1.2).

Inside the polar cap region the field lines are open and the plasma moves anti-sunward as the open field lines convect with the solar wind anti-sunward. At lower latitude in the auroral oval, the field lines are closed and move sunward to return flux to the dayside of the Earth. Hence, due to reconnection on the nightside, the plasma flowing toward the Earth and around to the dayside generates a two-cell convection pattern in the polar region for southward IMF. Although the flow of plasma is not thermally driven, as the flow is governed by large-scale electric and magnetic fields, this double-vortex flow pattern is referred to as "convection." The convection pattern is equivalent to an electric potential pattern from the definition of $\overrightarrow{E} \times \overrightarrow{B}$ drift. The convection velocity v is related to the electrostatic potential, as shown in equation 1.18 and 1.19. The $\overrightarrow{E} \times \overrightarrow{B}$ drift is perpendicular to both $\nabla\Phi$ and $\overrightarrow{B}$.

$$\overrightarrow{\mathrm{E}} = -\nabla\Phi \tag{1.18}$$

and

$$\overrightarrow{v} = -\frac{\nabla\Phi \times \overrightarrow{\mathbf{B}}}{\mathrm{B}^2} \tag{1.19}$$

Plasma flow can be measured from ground based HF SuperDARN radar, and this is discussed in chapter 2. About 10 percent of the magnetic flux from the solar wind that impacts the magnetosphere cross-section will undergo reconnection while the rest of the solar wind magnetic flux will be swept around the magnetosphere by the magnetosheath flow [3].

The exact motion of field lines depends not only on the motion of the solar wind but also on several factors such as the IMF orientation and dynamic

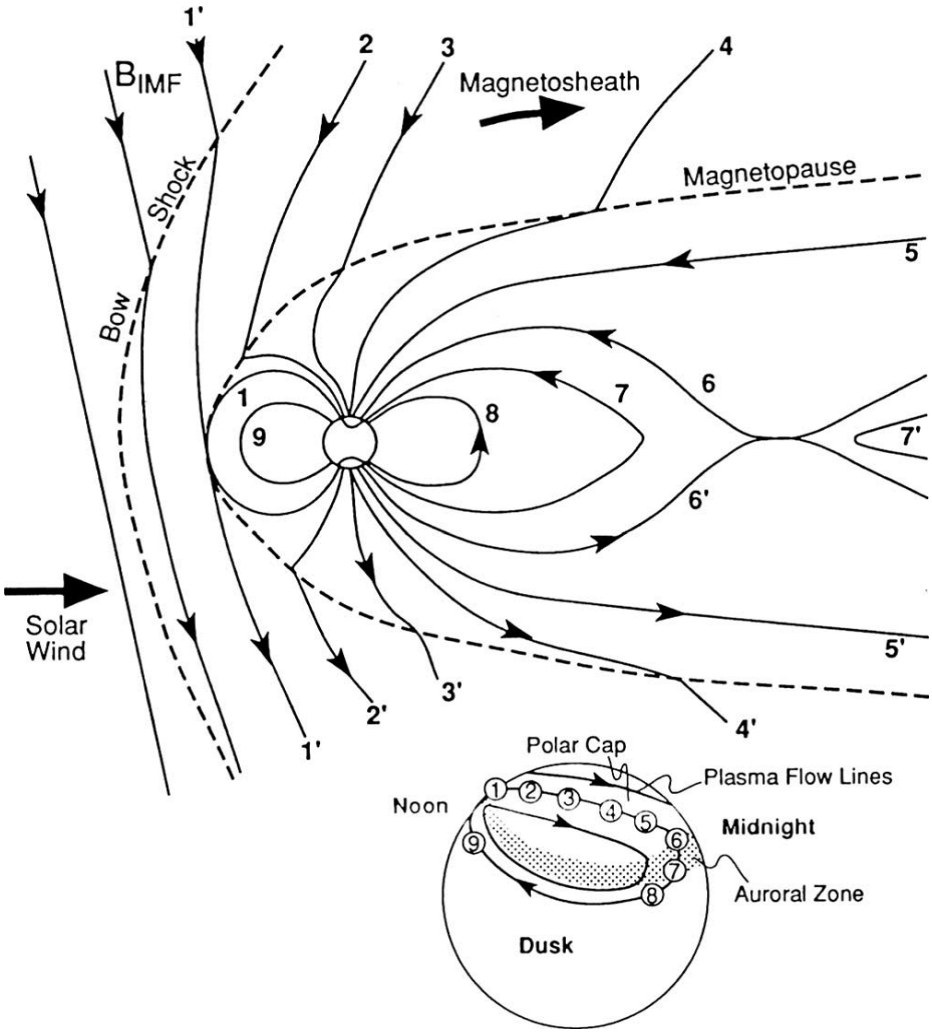

Figure 1.2: Schematic figure of field line merging and reconnection at the magnetopause in the noon–midnight plane. An IMF field line (1′) reconnects at the magnetopause with a terrestrial field line (1). Field lines (6) and (6′) reconnect at the magnetotail. Field lines labeled as 7, 8 and 9 are the terrestrial closed field lines whereas field lines labeled as 2 and 3 are the open field lines connected with solar wind. The open and closed field lines in the magnetosphere have footprints in the ionospheric polar region as shown at the bottom of the figure [2].

pressure of the solar wind. The separation between the last closed field lines and the first open field lines is called the open-closed field line boundary (OCB) (Figure 1.2). The location of the OCB is determined by the relative rate of dayside merging and nightside reconnection. When the dayside merging rate is

dominant, open field lines will be added faster in the high latitude ionosphere than are field lines closed by nightside reconnection, hence, the location of the OCB will move toward lower latitude [15];[16]. Therefore, to understand the energy transportation among solar wind-magnetosphere-ionosphere systems, the location of the OCB must be known.

1.3.3 Types of Magnetic Reconnection

Magnetic reconnection converts magnetic energy into kinetic and internal energy in the plasma, and allows the transfer of magnetic flux and mass from the two inflow regions to move across the separatrices into the reconnected outflow regions. Two approaches to a theory of magnetic reconnection are described. The first approach is that magnetic reconnection is a steady process; it assumes reconnection occurs continuously in a steady state manner based on the MHD theory [17]; [18]; [19]; [20]. Figure 1.3 shows a simple model of magnetic reconnection at the neutral line. The electric field (out of the page) drives plasma flow. The circled shaded region is the diffusion region while the current sheet region outside of the reconnection region is not diffusion dominated. According to this approach, the flow breaks into two parts: the frozen field dominated inflow region where conductivity is infinite, and the diffusion dominated outflow region. The boundary conditions are different for each solution. According to the Sweet-Parker two dimensional configuration [17]; [18], plasma inflow and outflow are balanced (and the diffusion region is extended to the length of the scale). According to the model, the reconnection process is slow, as the outflow velocity is equal to the Alfvén velocity and the inflow velocity $V_i = \frac{V_{Ai}}{\sqrt{R_M}}$. The reconnection rate is slow because the system length L is large compared to the width of the diffusion region. To overcome the low rate of diffusion, Petschek [19] proposed that system length L is equal to the length of the region where the opposite fields meet, rather than the total system length. In reality, Petschek's reconnection provides an upper limit to the

reconnection rate. A recent study shows that a fast reconnection needs to occur after a period of slow accumulation of magnetic energy [21]. Nevertheless, the steady state two dimensional reconnection approach shows that the magnetic energy is converted to plasma energy with an accelerated plasma flow [22].

All the steady models have limitations; it is assumed that inflow regions are symmetric except for the magnetic-field directions and it is assumed that the magnetic fields in the two inflow regions are purely anti-parallel, which, in reality, is not the case. Also, temporal variations are not considered in steady reconnection models. In the second approach magnetic reconnection is treated as a time-dependent process that involves an electric field at a separator; it is usually referred to as driven reconnection. Tearing mode instability is one approach [23]; [24]. Several neutral lines are produced as a uniform current sheet breaks into a series of current sheets – this event is posited to explain the phenomena occurring on the magnetopause [25] and magnetotail [26] reconnection. With the help of a tearing mode instability the substorm onset mechanism was explained [27]; [28]. However, none of the models can predict when and where the reconnection will occur.

Despite the two different approaches to explain magnetic reconnection, it is evident that reconnection results in a plasma jet flowing out of the diffusion region and in changes in magnetic topology.

1.3.4 The Rate and Location of Magnetospheric Reconnection

The magnetic reconnection rate can be measured at a single point on the magnetopause [29] or in the ionosphere [30]. The flux rate added to the polar cap is related to the reconnection electric field, E_{rec} for a particular segment (dl)

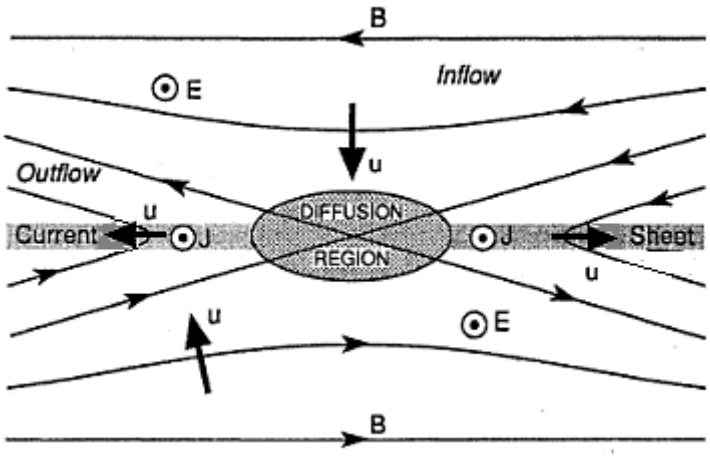

Figure 1.3: Schematic of magnetic reconnection at the current sheet; a bold arrow indicates the plasma flow [2].

of the polar cap boundary:

$$\frac{d\phi}{dt} = E_{rec}.dl \tag{1.20}$$

Where $\frac{d\phi}{dt}$ is the flux transfer rate. The reconnected electric field is related to the ionospheric convection velocity of the plasma [31] using equations 1.18 and 1.19.

The rate of magnetic reconnection therefore can be calculated using the ionospheric data from the SuperDARN radar network for the Earth's dayside [31] and nightside [32] reconnected regions.

Recent observations from the Cluster mission shows that in the accelerated plasma, mainly electrons are observed from the outflow region at the magnetotail during unsteady reconnection [33]. During steady reconnection, large scale electron acceleration was recorded by the Cluster spacecraft in the Earth's magnetotail [34]. Both observations indicate that plasma flow (measured from $\overrightarrow{E} \times \overrightarrow{B}$) detected from the spacecraft at the plasma sheet is observed as a high speed

bulk flow of plasma from the X-line. The spatial and temporal measurement of magnetic reconnection is practically impossible in the reconnection X-line region due to the deviation of the reconnection location and the motion of the spacecraft. The location containing the footprint of the X-line can be measured in the ionosphere using a network of radar and spacecraft; this will be discussed in Chapter 2. The area containing the footprint of the reconnected lines can be monitored continuously as the large directional derivative of flow. In this thesis, the directional derivative of convection flow speed, using ionospheric data from the SuperDARN HF radar network, are used to determine the location of the OCB proxy. Details of the methodology are presented in Chapter 2.

1.4 Substorm

In this thesis the observations of open-closed field line boundaries are studied during periods of quiet conditions and substorm conditions. As magnetic energy is stored and released from the magnetotail during the substorm growth phase and expansion phase, respectively, substorm dynamics might be related to the dynamics of magnetotail reconnection [32].

Substorms are global reconfigurations of the magnetosphere in which solar wind energy previously stored in the Earth's magnetotail for a long period of time is released abruptly producing particle heating and kinetic energy [35]. Though the energy originally comes from the solar wind, it must be first transferred to the magnetosphere. Magnetospheric plasma phenomena, like aurora and associated currents, are greatly influenced during the interval. The most accepted model of the substorm includes a growth phase associated with a southward turning IMF and a substorm expansion phase that occurs after the growth phase [36]. Samson et al. (1992) [37] shows that substorms are likely triggered by current disruption processes around 6-10 R_e. Though it has been unclear

whether substorms are initiated by the process of magnetic reconnection at $\sim$ 20-30 R_e or by a near-Earth dipolarization process [37], recent satellite observations indicate that substorms are likely triggered by tail reconnection at $\sim$ 20 R_e [38]. Nevertheless, in all cases of substorms the IMF must have been pointing southward for some period of time prior to the substorm to convect the field line toward the magnetotail and build up the magnetic pressure in the tail lobes, stretching the magnetotail.

When the IMF B_z component is positive, the closed magnetospheric configurations differ greatly [39]. The magnetosphere is never 'closed' as there are always open field lines and there is always some form of reconnection occurring somewhere on the magnetopause, regardless of IMF direction.

1.4.1 Formation of Aurora

Auroral emissions in the ionosphere occur due to the precipitation of electrons originating from the magnetosphere. There are two types of aurora: diffuse and discrete. Diffuse aurora form continually as electrons fall into the loss cone of the inner magnetosphere. Discrete aurora can be seen when energetic electrons precipitate along field-aligned currents and create significant auroral displays on the nightside of the ionosphere. Auroral emissions can be detected in ultraviolet, visible, and infrared spectra. OCB proxies can be measured from the poleward edge of ultraviolet emissions, and will be discussed in section 1.5.2 and 1.5.3, and also in Chapter 2.

1.5 Discussion of Previous Work on the OCB proxies

One mode of energy transfer from the solar wind into the Earth's magnetospheric region occurs via the process of magnetic reconnection between the solar wind interplanetary magnetic field (IMF) and the terrestrial magnetic field which results in the transfer of geomagnetic flux from the day side to the night side of the Earth [14]. It is important to know where the open-closed boundary is in order to study magnetic reconnection and the transfer of energy from the solar wind to the magnetosphere. A number of techniques have been developed as proxies for the open-closed magnetic field boundary, such as an optical signature of precipitation from all-sky cameras and spacecraft imagers [40]; [41], the particle precipitation boundary (PPB) measured by low-altitude spacecraft [42]; [43], and the SuperDARN spectral width boundary (SWB) [44]; [45]. All techniques used for identification of the open-closed boundary are proxies as there is no absolute measure of the actual open-closed field line boundary. In this thesis, the term OCB and OCB proxy are used interchangeably when referring to these techniques and in all cases OCB proxy is implied.

1.5.1 DMSP

The most reliable way to determine the OCB is to take measurements of particle precipitation boundaries (PPBs). PPBs measured by Defense Meteorological Satellite Program (DMSP) satellites are considered the best proxy of the OCB, although the open/closed separatrix is sampled infrequently at a single location rather than estimating boundaries globally and continuously during each overflight (the orbital period is around 100 minutes).

1.5.2 Polar UVI Observations

High latitude spacecraft observation overcomes the problem of global and continuous measurement of the OCB proxy by determining high energy (few KeV) electron precipitation. As the precipitating particles create auroral luminosity (discussed in chapter 1, section 1.4.1), optical imagers are employed to observe the OCB proxies, assuming a relationship between the auroral oval and the OCB [41].

The ultra violet imager (UVI) on the Polar satellite [46] was launched in February 1996 and ended operation in April 2008. The UVI optical sensor on the Polar spacecraft consisted of four UVI filters: two filters could detect photon flux as a function of wavelength in the range 130.4–135.6 nm for atomic oxygen emission lines and two filters could detect Lyman-Birge-Hopfield (LBH) bands in the 140–180 nm range. The LBH short filter and the LBH long (LBHL) filter, centered at $\sim$ 150 nm and $\sim$ 170 nm, respectively, could detect molecular nitrogen emissions. LBH filters were used to determine the OCB proxies at the night side of the Earth with a typical spatial resolution of about 30–40 km.

1.5.3 IMAGE FUV Observations

The far ultraviolet (FUV) imager used in NASA's Imager for Magnetopause-to-Aurora Global Exploration (IMAGE) spacecraft observations can be used to find an OCB proxy. The IMAGE spacecraft, in operation from May 2000 to December 2005, was constructed with three detectors on board, with each sensor sensitive to a different wavelength interval [47] ; [48]. The FUV instrument on the IMAGE craft was constructed with two spectrographic imagers (SI-12 and SI-13) and a wideband imager (WIC). The SI-12 camera is sensitive in the 128 nm band to measure proton precipitation while SI-13 can detect 135.6 nm oxygen emission bands resulting from energetic electron precipita-

tion. Narrow band UV emission (130–140 nm) corresponds to an OCB proxy in the post-midnight to dawn sector while wideband auroral UV emission in the range 140–180 nm is an effective OCB proxy in the other MLT sectors [49].

1.5.4 Doppler Spectral Width Boundary (SWB)

The Doppler spectral width of SuperDARN backscatter has been tested to find the OCB over large areas of the ionosphere for Earth's day side [44] and night side [50]. A boundary between low spectral width echoes at lower latitude and high spectral width echoes at higher latitude can be used as an OCB proxy because the backscatter power at low spectral width corresponds to closed field lines. The latitudes of SuperDARN SWB and DMSP PPBs are compared in the night, morning and afternoon sectors [51]; [52]; [53]; [54]; [49]. The surveyors concluded that the SWB is a good proxy for the OCB in the noon and pre-midnight sector [54] while the SWB is equatorward in the morning and afternoon sector [54]; [53]. A routine and reliable technique to monitor the OCB at all magnetic local time has yet to be developed. Some of the physical factors that affect the spectral width are still not understood (e.g., see a review by Chisham et al., [55]), although studies show that the SWB might be related to intense particle precipitation [44] and large scale ionospheric convection patterns [56].

Chapter 2

Instrumentation and Data Analysis Methods

2.1 Introduction

It is well established that magnetic reconnection drives a convection cycle in the magnetosphere that maps into the ionosphere (e.g., Cowley (1998) [57] for a review). Therefore the boundary between open and closed field lines might be observable in the ionospheric convection pattern. This chapter provides the methodology of a new directional derivative of convection flow speed technique which is used to determine the open-closed magnetic field line boundary (OCB) that separates the polar cap from the auroral zone. The Super Dual Auroral Radar Network (SuperDARN) dataset is used to calculate the directional derivative of the convection flow speed for determination of the OCB proxy. In this thesis, the OCB proxy measured from the directional derivatives of SuperDARN convection flow is expressed as the SuperDARN OCB. Details of SuperDARN instrumentation and operation are discussed in the next section.

In situ satellite-born instrumentation that includes the Defense Meteorological Satellite Program (DMSP), the Imager for Magnetopause-to-Aurora Global

Exploration (IMAGE) and the Polar spacecraft, depending on their availability, are used to determine the OCB and compare the results with those obtained using the directional derivative of SuperDARN convection flow technique. In addition, data from the Advanced Composition Explorer (ACE) satellite are used to investigate the solar wind conditions during the events of interest. Portions of this chapter will include a description of these satellite instruments and the data analysis methods used in this thesis to determine the OCB from these instruments.

It is important to check if the spacecraft and SuperDARN are at the right position at the right time to collect data, because areas of interest need to be investigated from SuperDARN under particular solar wind conditions and the results need to be compared with those obtained with other experimental techniques. It is very difficult to obtain simultaneous measurements of the OCBs with directional derivatives of convection flow speed techniques and other established techniques. Case studies of such measurements using ground and space based instrumentation are the topic of later chapters. SuperDARN data are used in all events considered in this thesis along with data from available satellite borne-instruments.

2.2 Principles of Coherent Scatter Radar

Coherent scatter radars such as SuperDARN detect a backscatter signal from plasma irregularities within a medium. The scattered signal is coherent because half the radar wavelength matches the size of the irregularity on a scale of a few to 10 meters. The theory of scattering is based on the Bragg condition and principles of the conservation of momentum and energy [58]. If irregularities in the medium have wave number k_m, the radar scatters according to the

conservation of momentum:

$$\overrightarrow{k_t} = \overrightarrow{k_s} + \overrightarrow{k_m}, \tag{2.1}$$

Where $\overrightarrow{k_t}$ is the wave number of the transmitted wave, and $\overrightarrow{k_s}$ is the wave number of the scattered wave. For backscatter, $\overrightarrow{k_m} = 2\overrightarrow{k_t}$ because $\overrightarrow{k_t} = -\overrightarrow{k_s}$. Thus, for a radar backscatter, the irregularity (spatial resolution) must have a size of half the radar operating wavelength to achieve constructive interference in the direction of the radar [58]. From the principle of conservation, the radar's line of sight Doppler frequency shift, equivalent to the measurement of the irregularity, is equal to the difference between the transmitted and backscattered frequencies. These are the primary conditions to obtain information on the line of sight Doppler velocity, backscattered power, and spectral width measurements in coherent radars such as those in the SuperDARN. Another requirement for measuring ionospheric irregularities is that the transmitted signal must be orthogonal to the field-aligned irregularity. SuperDARN observes in a nearly vertical magnetic field and fulfills this requirement.

Research has shown that most ionospheric irregularity is the result of plasma instability [58]. Earlier (1970s and 1980s) coherent scatter radars, such as the Scandinavian Twin Auroral Radar Experiment (STARE), measured E-region ionospheric irregularities in the very high frequency range (VHF) [13]. However, instead of $\overrightarrow{E} \times \overrightarrow{B}$ drift velocity, plasma temperature dependent two stream drift instabilities were often detected by STARE [59]; [60]. Coherent scatter radars such as those used in SuperDARN can measure plasma instability in the auroral F-region where ion and electron motion are equivalent and therefore the perpendicular drift is the $\overrightarrow{E} \times \overrightarrow{B}$ velocity. Hence the motion of irregularities in the ionospheric F-region can be used to measure of ionospheric plasma convection, as discussed in section 2.3.

2.3 The Super Dual Auroral Radar network

The Super Dual Auroral Radar Network (SuperDARN) [13] is an international collaboration involving 11 countries and 32 high frequency (HF) radars. These radars monitor ionospheric convection over the northern and southern polar regions. Currently 21 radars are engaged in the northern hemisphere and 11 radars monitor the southern hemisphere. The fields of view of the northern hemisphere radars are shown in Figure 2.1. A detailed description of the SuperDARN is given in Greenwald et al., (1995) [13]. Each SuperDARN radar is an array of 16 antennas operating in the 8–20 MHz band. The radar beam can be steered into 16 azimuthal beam directions spanning a total of 52 degrees. Along each beam direction, the radar can detect backscatter from 75 different range gates with 45 km resolution beginning at an initial range of 180 km. Earlier radars were identical in operational concept whereas newer radars have a different antenna design and some radars can operate at dual frequencies simultaneously. The radar transmits a short sequence of pulses in the HF band and samples the returned backscatter. The pulse sequence is designed to produce multi lag autocorrelation functions as a function of range. If significant backscatter occurs, the autocorrelation functions (ACF) are fitted to calculate backscattered power, spectral width, and Doppler velocity of the plasma density irregularities in the ionosphere. All SuperDARN radars typically operate at a temporal resolution of 1–2 minutes. The temporal resolution is 2 minutes in the data presented in this thesis.

HF signals are scattered in the E and F regions of the ionosphere due to field aligned electron density irregularities in the ionosphere. High frequency signals refract through ionospheric layers. If emitted HF signals are propagating perpendicular to the magnetic field B and they encounter electron density irregularities, the signal will return to the radar, as discussed in Section 2.2. Ir-

regularities in the F region are at rest with respect to the background of plasma convection [61]. Hence the Doppler velocity represents ionospheric plasma flow.

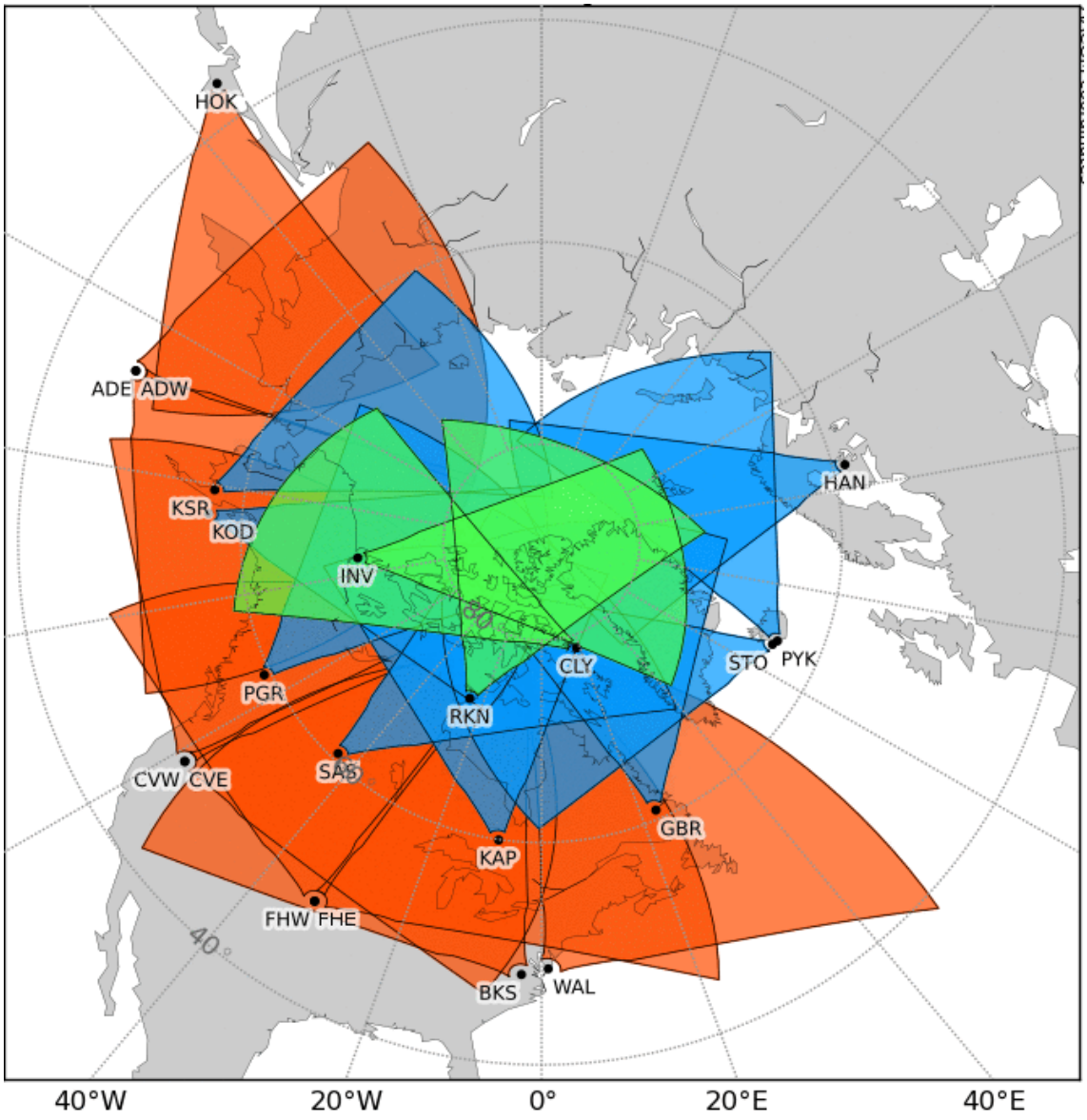

Figure 2.1: The most recent field-of-view (FOV) of the Super Dual Auroral Radar Network (SuperDARN) in the northern hemisphere plotted in geomagnetic coordinates in July, 2013. The green, blue and orange colors represent FOV of SuperDARN at polar cap, high latitude and mid latitude respectively. [`superdarn.org`]

2.4 Global Convection Measurement

The 2-dimensional convection velocities obtained from SuperDARN are required to calculate directional derivatives of the convection flow speed. HF radar detects the motion of ionospheric irregularities that result from a shift in the Doppler frequency Δf of the radar backscatter. The line-of-sight (l-o-s) Doppler velocity plasma drift V_D of the irregularity is related to the Doppler frequency shift:

$$V_D \approx \frac{\Delta f \lambda_r}{2}, \tag{2.2}$$

Where λ_r is the operating radar wavelength.

HF radar pairs can produce 2-dimensional convection velocities if they overlap each other (have common volume areas) by merging the l-o-s Doppler velocities from beams of these radar pairs. Large-scale ionospheric convection can be derived by repeating the procedure for all overlapping radar pairs [13]. However, overlapping fields of view with good backscatter are typically not available on a global scale, so a powerful "map potential" technique [62] is used to generate global convection maps at two minute time resolution. The convection maps are a spherical harmonic fit of the observed Doppler velocity measurements with a statistical model based on the prevailing interplanetary magnetic field (IMF). To get a global-scale view of ionospheric convection, distributions of electrostatic potential in the ionosphere Φ are fitted according to the available line-of-sight velocity measurements at the time of interest according to equations 1.18 and 1.19. A detailed description of the spherical harmonic fit of the observed Doppler velocity measurements with the statistical model can be found in Ruohoniemi and Baker (1998) [62], Ruohoniemi and Greenwald (1996) [63], and references therein.

The order of the fit is a variable parameter; higher order fits produce convection maps closer to the statistical model [55]. In this thesis, the order of fit is adjusted to 6 which is a lower order of fit. Therefore, the resultant convection maps are less dependent on the statistical model and more dependent on the observed backscatter [64]; [63].

Figure 2.2 shows an example of a convection potential map at 8:02 UT (universal time) on November 04, 2001 taken from Virginia Tech website [`superdarn.org`]. The order of fit is 8 in Figure 2.2. As discussed earlier the plasma irregularities detected from SuperDARN radars drift at the $\overrightarrow{E} \times \overrightarrow{B}$ velocity. As ionosphere and magnetosphere map to each other, the cross-magnetospheric electric potential is identified in Figure 2.2. The contours of constant electrostatic potential (solid and dashed lines) also represent flow streamlines. Input IMF conditions with suitable time-lags from spacecraft are utilized to determine the proper statistical model. The top-right side of Figure 2.2 shows the z and y components of the IMF and the magnitude of the IMF B_z component in units of nano-Tesla (nT).

It is well established that the ionospheric convection pattern is related to the IMF direction and orientation [65]; [57]. The overall convection pattern is two-celled, with anti-sunward flow across the polar cap and returned sunward flow in the lower latitude in dawn and dusk sectors of the ionosphere. The typical two-cell convection pattern might be distorted by the IMF B_y component in such a way that the dawn (dusk) cell is dominant for negative (positive) B_y; this will be discussed in Chapter 5. The reverse convection cell [66]; [67] and the four cell convection pattern [68] can be observed from the SuperDARN during strong northward IMF conditions.

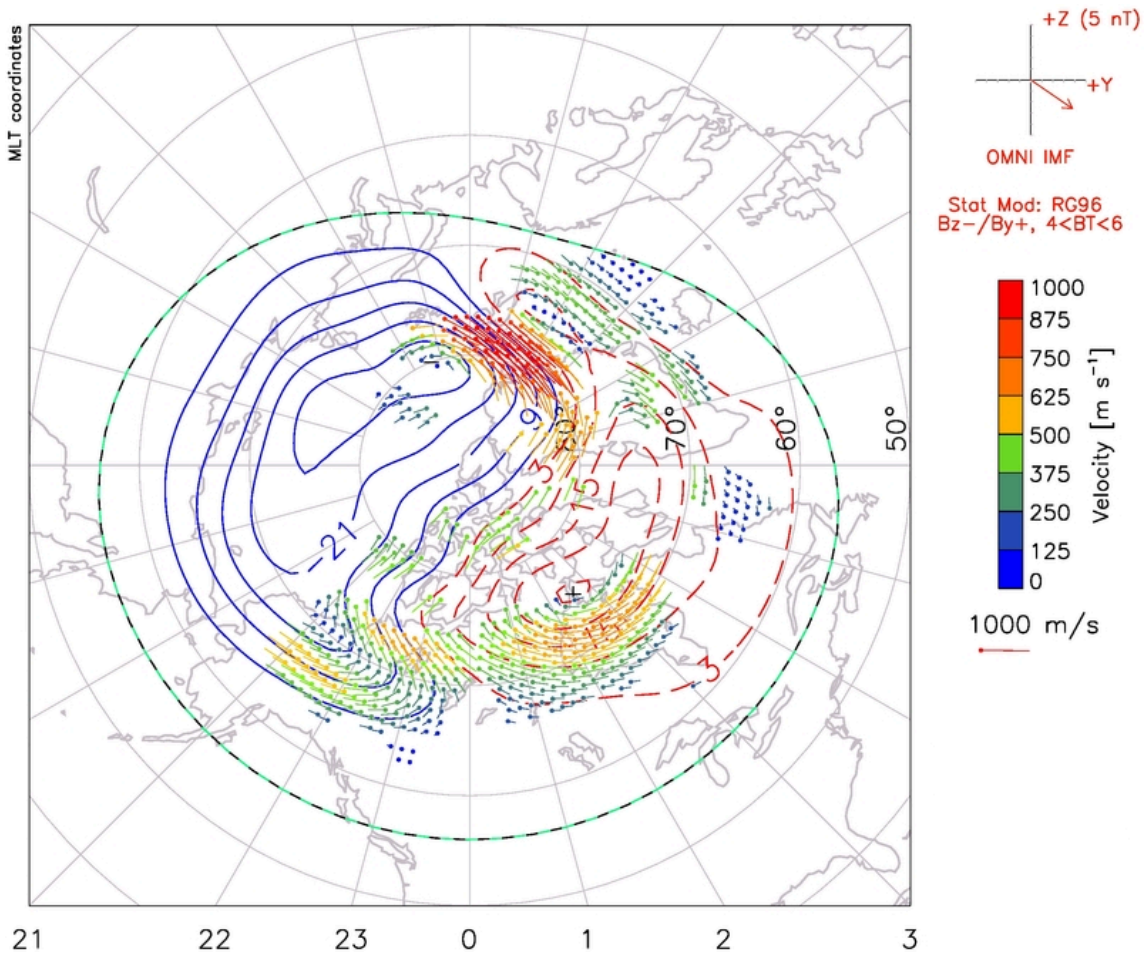

Figure 2.2: Global convection map estimated from SuperDARN observations on November 04, 2001, at 08:02 UT. The order of fit is adjusted to 8. Radial co-ordinates represent magnetic latitude differences starting from 50° and the radial lines represent MLT (magnetic local time) meridians, with noon at the top and midnight at the bottom. The dots at the beginning of the vectors indicate the vector locations, the lines show the vector direction, and the colors and length of the lines show the vector magnitude. The velocity scale is shown at the right side of the Figure. Solid (dotted) contours are associated with negative (positive) values of electrostatic potential. IMF condition is at the top-right corner of the Figure. [`superdarn.org`]

2.5 Methodology

As discussed in Chapter 1 reconnection occurs when the frozen in flux condition breaks down and diffusion takes place when two anti-parallel magnetic field lines shear and merge [2]. Reconnection can occur when the IMF has other orientation. Crooker showed that the requirement of magnetic field line merging is not strictly on anti-parallel fields but also occurs with anti-parallel components of the field lines [69]. Reconnection can occur when IMF is east or west oriented [70] or when the IMF is northward [71].

Fenrich et al., [72] and Crooker [69] showed that dayside reconnection occurs over large regions of the magnetopause and over a large range of magnetic local time. Ionospheric footprints of dayside magnetic merging regions are located from $\sim$ 7 to $\sim$ 18 MLT in the dayside during the southward IMF and dusk directed IMF (when the IMF B_y is positive) [72]. Using MHD model, White et al., [73] and Siscoe et al., [74] showed that the magnetospheric sash which is a region of magnetic merging extends from the dayside cusp to the near-Earth tail.

Magnetic field lines can be reproduced from the global magnetospheric models such as Fedder-Lyon MHD global simulation model ([75]; [76]). Field line tracings of the last closed and first open field lines at select points along the OCB were determined from the MHD global model [72]. The field line tracings and measuring the corresponded ionospheric open closed boundary locations are therefore an established technique from the MHD global model [72] ;[77]. The location of reconnection and the rate of reconnection is controlled by the physical boundary conditions [75]. It is found that the the location of the OCB extends from dawn to dusk for southward IMF [76]. Russell et al., [78] tested Fedder-Lyon MHD model with Polar MFE measurements and found an

excellent agreement in terms of magnetic field reconnection and plasma measurements.

As shown in Figure 1.2 the newly reconnected field line is bent at the reconnection location and therefore there is a curvature force that accelerates plasma away from the reconnection region. From the ISEE spacecraft observation, large plasma flow speed was observed during the reconnection process and it was therefore concluded that a velocity enhancement in the outflowing plasma can occur at the outflow region of magnetic-field reconnection [29]. As discussed in section 1.3.3, reconnection models indicate that the inflow energy is magnetic rather than kinetic. Moreover, half of the inflowing magnetic energy is converted into kinetic energy in the outflow [79]. From the diffusion equation it is evident that the some of the inflow magnetic energy transforms into heat. Therefore plasma flow decreases prior to reconnection in the magnetotail. The strong increase in plasma flow within the reconnection outflow region occurs on newly reconnected field lines and thus may be used as a signature of the OCB.

Viscous-like interaction is another mechanism that may influence magnetospheric plasma convection during the interaction between the solar wind and the Earth's magnetosphere [80]. Circulation of plasma throughout the magnetosphere may occur due to the solar wind flow over the surface of the magnetosphere [81]; [80]. Crooker showed that during northward IMF the reversed sun-ward convection near noon occurs due to magnetic reconnection at the cusp region [39]. Early studies showed that the four convection cells, two reverse cell at higher latitude originated from lobe reconnection and two convection cell at lower latitude driven by viscous process can occur [65]; [39]. However studies suggested that the four cell convection is uncommon event [82]. Although with the use of SuperDARN, the existance of a reverse convection cell and the four

convection cell pattern have been shown [66]; [68]. Typically the potential drop is $\sim$ 5 kV in reverse convection cell and it takes $\sim$ 12 minute to form after a northward turning IMF [68]. Therefore not all magnetic reconnection corresponds to an OCB.

The structure and dynamics of ionospheric convection measured by SuperDARN have been used to test reconnection theories and measure reconnection rates. Given that plasma flows are affected by reconnection as discussed above, it may be possible to use measurements of changes in the SuperDARN convection flow speeds to identify the foot-points of reconnection and the OCB associated with reconnection. The following paragraphs illustrate how ionospheric convection flow varies along a convection streamline in the nightside ionosphere.

The convection flow derived from the SuperDARN convection map potential along 21 kV and 27 kV contours are plotted in Figures 2.3 and 2.4. The Figure 2.3 shows the convection map when the cross polar cap potential is 64 kV and the order of fit is adjusted to 6. The velocity scale is shown at the left side of the Figure. The 1-2-3 and 1$\prime$-2$\prime$-3$\prime$ closed line represents 21 kV and 27 kV potential contour respectively.

Since the point of interest is only in the region where ionospheric backscatter exists, the discussion is limited to the convection velocity from point 1 (1$\prime$) to point 3 (3$\prime$) along the 21 (27) kV contour. It is noted that although the flow at point 2 along the 21 kV contour is at a local maximum ($\sim$ 700 m/s) the flow minima are located at point 1 and 3 along the 21 kV potential contour (Figure 2.3 and the top panel of Figure 2.4). Similarly the flow minima are located at 1$\prime$ and 3$\prime$ along the 27 kV contour while the maximum flow ($\sim$ 600 m/s) is located at point 2$\prime$ (Figure 2.3 and the top panel of Figure 2.4). Note

that the flow streamlines, therefore, converge from point 1 (1′) to point 2 (2′) corresponding to a positive rate of change of the flow speed; and diverge from point 2 (2′) to point 3 (3′) corresponding to a negative rate of change of flow speed (Figure 2.4 top-bottom). This is consistent with the calculated Super-DARN directional derivatives shown in Figure 2.5. Also note that the peak in the positive directional derivative, i.e. the maximum positive slope in the flow speed vs. position curves shown in the top two panels of Figure 2.4, occur just downstream of the flow minima. These large positive peaks in the directional derivatives of the convection flow may represent the OCB, to be discussed in the next section. However, not all peaks in the directional derivative of the flow can be associated with the OCB and/or reconnection.

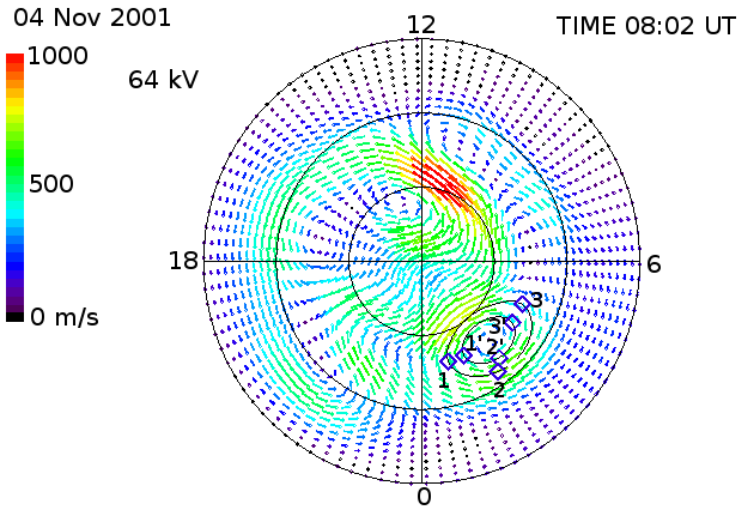

Figure 2.3: Top: Global convection map from SuperDARN observations adjusted to 6 order of fit on November 04, 2001, at 08:02 UT. Radial co-ordinates represent magnetic latitudes from 90 ° to 60° and the radial lines represent MLT meridians, with noon at the top and midnight at the bottom. The flow speed scale is shown at the right side of the Figure. The two solid contours 1-2-3 and 1′-2′-3′ are associated with 21 kV and 27 kV electrostatic potential respectively.

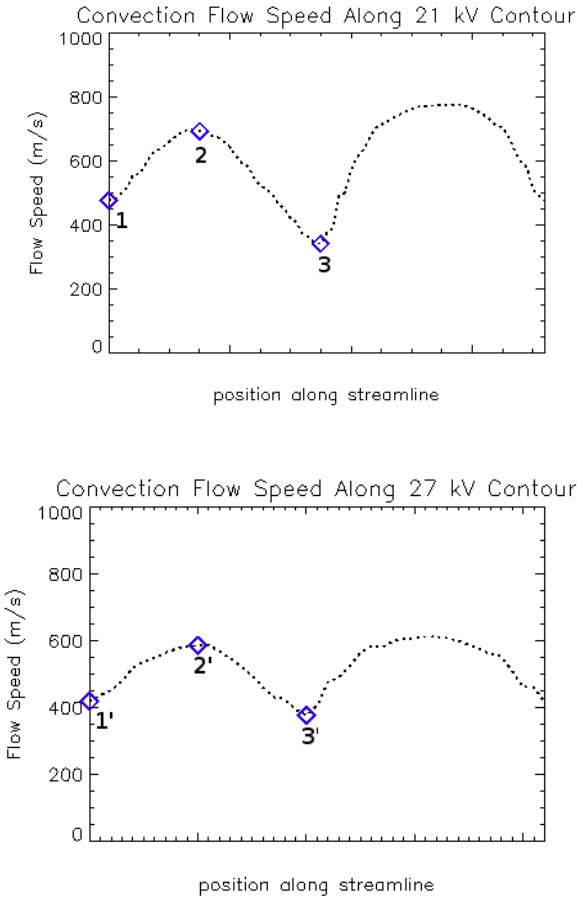

Figure 2.4: Top: Convection flow along 21 kV contour at 08:02 UT on November 04, 2001. Point 1 and 3 are marked as the minimum convection flow while and point 2 is marked as the maximum convection flow. Bottom: Convection flow along 27 kV contour at the same time point. Point 1′ and 3′ are marked as the minimum convection flow while and point 2′ is marked as the maximum convection flow.

2.5.1 Directional Derivative of the Convection Flow Speed Technique

Convection map velocities and electrostatic potential values are output from the generic SuperDARN convection mapping code to a magnetic latitude, magnetic longitude grid fixed with respect to the Earth. To account for the rotation of the grid with the Earth, the convection velocity components at each time point are interpolated to a fixed magnetic latitude, magnetic local time (MLT) grid. The result is a time series of the convection velocity components at each fixed magnetic latitude, magnetic local time grid point. The magnetic latitude/local time grid is a 30×180 array with 1° resolution in the latitudinal direction from 60°-90°, and 2° resolution in the longitudinal direction, or .13 hours in MLT. The time series at each grid point is then low pass filtered at 0.5 mHz (equivalent to $\sim$ 33 minute period) to remove high frequency variations in the convection map velocities. To simplify plotting and to make the directional derivative calculation consistent at different latitudes, the grid point locations and the input velocity vectors are converted from the magnetic latitude, magnetic local time coordinate system to an x-y Cartesian coordinate system. In this x-y Cartesian coordinate system, the x-axis corresponds to the 18 and 6 MLT meridians and its scale ranges in value from -30 to 30 units where one unit of distance along the x-axis corresponds to one degree latitude. Likewise, the y-axis corresponds to the 0 and 12 MLT meridians and its scale also ranges from -30 to 30 units with one unit of distance corresponding to one degree. The origin of the x-y coordinate system is the north magnetic pole at 90 degrees magnetic latitude. It is a straight forward calculation to convert the grid coordinates and the convection velocities from the input magnetic local time, magnetic latitude coordinate system to this new x-y coordinate system.

At each grid point the streamline gradient in convection flow is subsequently

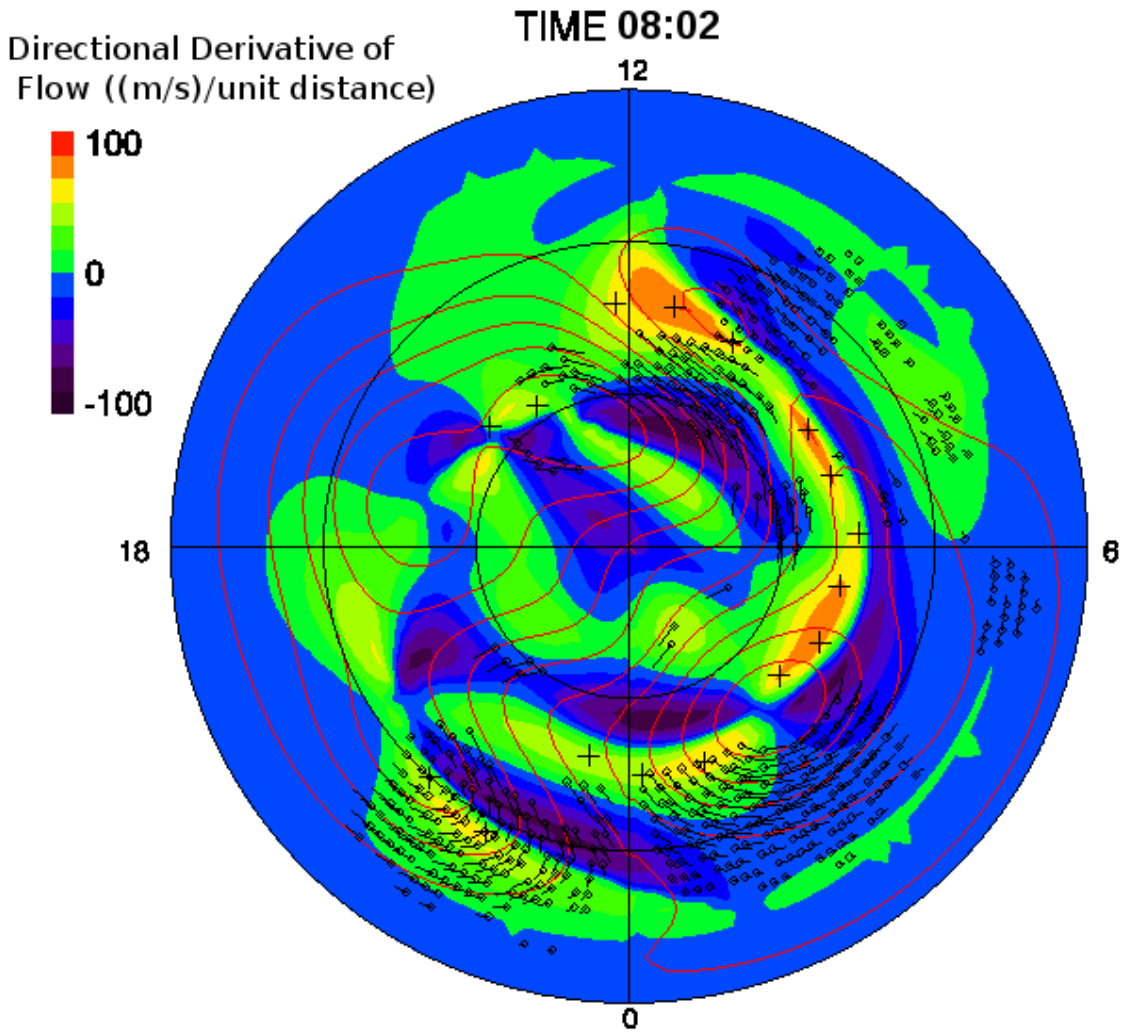

Figure 2.5: Directional derivative of SuperDARN convection flow map at 08:02 UT in magnetic latitude (MLAT)–magnetic local time coordinates. Solid black circles represent 60°, 70°, and 80° MLAT, and radial lines represent MLT meridians at midnight, morning, noon, and evening, with noon at the top and midnight at the bottom. The square dots at the beginning of the vectors indicate the vector locations and the lines show the vector direction and magnitude. The red contours on the left (right) side are associated with negative (positive) values of electrostatic potential. The magnitudes of the potential contours ranges from 3 kV to 27 kV with 6 kV increment between lines. The plus signs indicate the 'peak' of the directional derivative of plasma flow along the MLT meridian. The directional derivative of the convection flow speed scale is shown at the top-left side of the Figure.

calculated by determining the change in flow speed over a small distance along the streamlines. The directional derivatives values are derived at the same grid points (1° in latitude and 2° in longitude) as the input convection velocities and electric potential values, however, to get a proper measure of the derivative of the flow speed, a smaller distance along the streamlines is required when calculating the change in flow speed. The distance over which the change in flow is calculated is tested at different levels and is adjusted to 0.2 units of distance along the x and y directions, respectively. Other distances were tested and the derivatives were found to be the same for distances smaller than 0.2 units. Note that in order to calculate these derivatives, values of the flow speed were interpolated at the 0.2 unit intervals. The minimum curvature algorithm (MIN_CURVE_SURF function in IDL) is applied to interpolate-at 0.2 unit resolution. The directional derivative of flow speed is defined by:

$$(\frac{\overrightarrow{\mathrm{V}}}{\left|\overrightarrow{\mathrm{V}}\right|}.\nabla)\mathrm{V} \tag{2.3}$$

where V and $\overrightarrow{\mathrm{V}}$ are the speed and velocity of plasma flow along the convection streamline, respectively. Since the change in flow is taken over 0.2 unit intervals in the x-y coordinate system, the directional derivative of flow is given in units of $\frac{\mathrm{m/s}}{\mathrm{unit\,distance}}$ in the x-y coordinate system.

In the x-y coordinate system equation 2.3 becomes:

$$\frac{\left(V_x\hat{i}+V_y\hat{j}\right)\cdot\left(\frac{\partial V}{\partial x}\hat{i}+\frac{\partial V}{\partial y}\hat{j}\right)}{\sqrt{V_x^2+V_y^2}} \tag{2.4}$$

Where V_x and V_y are the component of $\overrightarrow{V}$ along x and y directions respectively and $\hat{i}$ and $\hat{j}$ are the unit vectors along x and y directions. Note that the magnetic field $\overrightarrow{B}$ is approximately perpendicular to the x-y plane (along z axis).

Figure 2.5 illustrates via color contours the map of directional derivatives of convection flow speed calculated from the band pass of the original flows of the convection map shown in Figure 2.3. The green to red contours correspond to positive values of the convection flow gradient, i.e. increasing flow speed along the streamline, while the blue to black contours correspond to negative values of the convection flow gradient, i.e. decreasing flow speed along the contour. Some inconsistency between the flows of the convection map plot (Figure 2.3) and the calculated flow gradient (Figure 2.5) may occur because the directional derivative of flow are calculated from the band pass of the original flows. Inconsistency might also be partially due to the finite resolution of the grid and issues with the contour plot routine in IDL. We postulate that the positive peak in the directional derivative of flow along a flow streamline, marked as a yellow to red contour (Figure 2.5), may be associated with magnetic reconnection between open and closed field lines and thus is a signature of the OCB. Since the convection map velocities are only reliable in regions where ionospheric backscatter exists [64], the peaks in the directional derivative are considered in the analysis only in the vicinity of regions where ionospheric backscatter exits. Note that the higher and lower orders of fit were tested and key features in the directional derivative of the convection flow speed maps remained consistent however the higher order fits showed more small scale structure in the directional derivative of the convection flow speed maps [64]; [63]. Potential OCB locations are indicated by plus signs along the meridians in Figure 2.5. To obtain the latitudinal locations of the OCB for each MLT sector, equivalent to 180 grid points, the latitudinal location of the peak value at each MLT grid point is identified and then these are averaged over each hour in MLT. The location of the plotted point is in the center of each MLT hour.

Generally a single 'peak' or maximum positive value of the SuperDARN convection flow directional derivative along any MLT meridian is observed and

marked as an OCB. Any other 'peaks' will be secondary peaks. The maximum peak is considered as the potential OCB unless there is no data in the vicinity (Figure 2.5). Secondary peaks may be observed particularly in the midnight region which will be discussed in Chapter 5.

The universal time of signal acquisition is indicated at the top of Figure 2.5 while magnetic midnight, dawn, noon, and dusk are indicated as 0 (at the bottom), 6 (on the right-hand side), 12 (at the top), and 18 (on the left hand side) MLT, respectively. In this thesis, all the directional derivatives of the convection flow speed figures are presented in a magnetic latitude– magnetic local time coordinate system with the indicated lines of constant latitude drawn at 10 degree increments from 60° to 90°. Directional derivative of flow measurements are color-coded according to the color-scale, ranging from -100 to 100 $\frac{\text{m/s}}{\text{unit distance}}$ on the left of Figure 2.5. The dusk (dawn) potential contours, marked as solid red lines, are negative (positive) contours drawn at 6 kV increments from 3 kV to 27 kV. The original unfiltered convection map velocities in regions of ionospheric backscatter are shown with small open square symbols and black lines indicating magnitude and direction.

2.6 Satellite Instrumentation and Data Analysis

Previous work on OCB proxies with various methods was presented in chapter 1, section 1.4. In this section the details of the spacecraft instruments and how the data is analyzed to determine the OCB for the events of this thesis are discussed. This section also provides one example time point for DMSP PPB, and SuperDARN Doppler Spectral width from the November 04, 2001 event, to be discussed in chapter 3. One example time point for Polar UVI is also

shown from the February 05, 2000 event, to be discussed in chapter 4.

2.6.1 DMSP

PPB measurements are taken by the SSJ/4 spectrometer instruments onboard the Defense Meteorological Satellite Program (DMSP) satellites [83]. The data provide the energy spectrum of electrons and ions that cause the aurora and other high latitude phenomena. The data set consists of electron and ion particle fluxes between 30 eV and 30 KeV as they flow past the spacecraft toward the Earth. DMSP satellites move in a low altitude polar orbit with the nominal altitude of 830 km. The algorithms used to determine Earth's night side and day side PPBs from DMSP energy spectra are discussed in Newell et al. (1991) [84]; [85]; [86]; [85]; [86]. The night side boundary represents the poleward edge of subvisual drizzle while the day side boundary represents a transition from a closed to an open precipitation region [87]. These two boundaries are collectively known as the poleward auroral precipitation boundaries (PAPB). Figure 2.6 shows one example of an electron and ion spectrogram measured by F15 spacecraft to measure the location of the OCB on November 04, 2001 (the event is discussed in Chapter 3). From the DMSP PPBs the OCB is defined as the b6 boundary on the nightside measured from the electron spectrogram. When going from closed to open field lines, the b6 boundary can be defined from a large drop in electron fluxes below the detectable level or can be characterized by the first encounter of a polar rain signature. The ion spectrogram can be used to determine OCB in polar cusp region. The identified boundaries and energy spectrum are obtained from the Johns Hopkins University Applied Physics Laboratory: `http://sd-www.jhuapl.edu/Aurora/dataset_list.html`. In Figure 2.6, the spacecraft was moving poleward and encountered electron precipitation at $\sim$ 10:07:05 UT. The electron flux increased at $\sim$ 10:07:44 UT, and thereafter gradually increased until $\sim$ 10:09:33 UT. A drop in flux after the interval

was identified as the OCB [85]; [86]; [87]. Based on the time, the final drop in electron flux occurred at 70.7° magnetic latitude. In Chapter 3 the Super-DARN OCB are compared with the pre-defined DMSP particle precipitation boundaries, obtained from the online DMSP database.

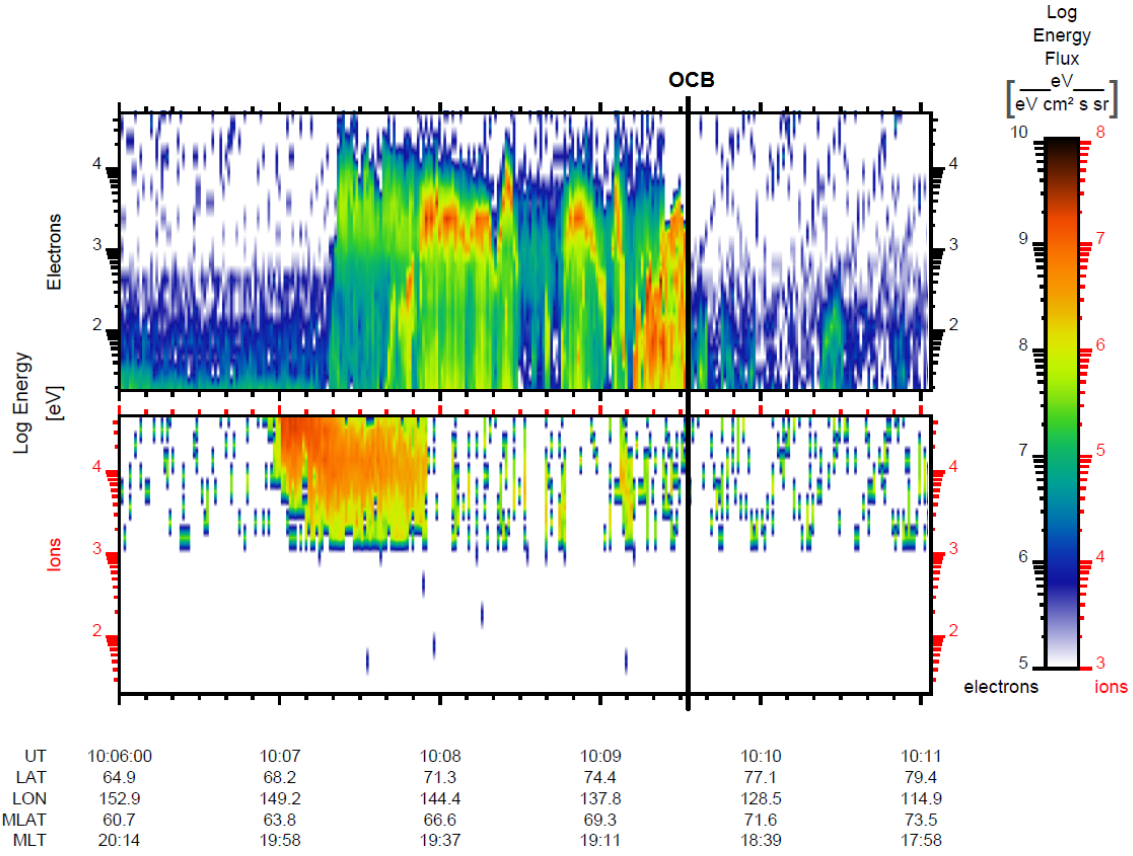

Figure 2.6: Spectrograms of electron and ion for the interval 10:06–10:13 UT from the DMSP F15 spacecraft. The b6 boundary is identified from the electron spectrogram.

2.6.2 Polar UVI Observations

In this thesis, the Polar UVI data are taken during the interval of 1996 to 2000 because the high temporal resolution and wide field of view in this period are advantages in identifying auroral emissions [88]. The integration time of polar UVI filters can vary. On February 05, 2000, the temporal resolution of the

LBHL filter was $\sim$ 37 s. The satellite suffers wobble, much shorter than the integration time (approximately $\sim$ 6s). The Polar orbital plane slowly drifted southward, therefore, the OCB could be determined in the northern hemisphere before the year 2000. The full width half maximum (FWHM) technique, proposed by Carbary et al., (2002) [89] was used to determine the OCB from the Polar UVI emissions.

The Polar UVI auroral latitudinal profiles are similar to the Gaussian shapes [90]. Polar UVI data is provided by the University of Washington under the direction of Dr. G. Parks. The data is in common data format (CDF) and can be obtained from the website `ftp://cdaweb.gsfc.nasa.gov/pub/data/polar/uvi/uvi_level1/`. The STUDIO software provided by the Polar UVI team was used to process the Polar UVI data. STUDIO is written in IDL language. The output data from the software provides the auroral image with a number of data fields, including magnetic latitude, magnetic local time in the AACGM coordinate system [91].

Each Polar UVI image is divided into 24 one-hour MLT segments. The latitudinal intensity profile, starting from 50° was constructed for each MLT segment. The latitude profiles are fitted with single Gaussian peak of the auroral oval with a quadratic background. The detail of single Gaussian fit procedure is discussed by Carbary et al., [89]. Figure 2.7 shows the Polar UVI image at 22:06 UT on February 05, 2000. The Gaussian fitting function can be used if the fractional standard deviation of the fit to each intensity profile is lower than 0.20. The poleward auroral boundary can be estimated using the full-width-at-half-maximum (FWHM) of the Gaussian peak. The poleward boundary of the oval is the location of centre of the peak plus the FWHM. The value of the poleward boundary of the auroral oval on one hour local time bins is considered as the OCB proxy. If the auroral boundaries are poorly fitted or do not meet

the criteria of fitting the boundary then they are not used as an OCB proxy [89].

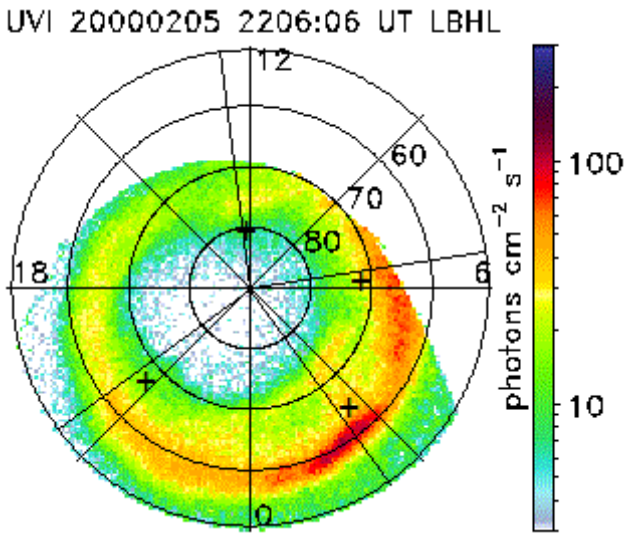

Figure 2.7: Polar UVI image at 22:06 UT on February 05, 2000 in magnetic latitude (MLAT)–magnetic local time coordinates. Solid black circles represent MLAT starting from 50°, and radial black lines represent MLT meridians at midnight, morning, noon, and evening, with noon at the top and midnight at the bottom. The solid lines represent the four MLT segments at 2.5, 6.5, 12.5 and 20.5 MLT. The plus signs indicate the locations of OCB measured from the Gaussian fitting technique. Auroral intensity is color coded according to the scales located at the right of the Figure.

Figure 2.8 shows four latitudinal profiles with OCB locations. Each profile is one hour long in MLT. Figures 2.7 and 2.8 show the locations of OCBs are at 63°, 71.6°, 80°, and 68° at 2.5, 6.5, 12.5, and 20.5 MLT, respectively (Green solid lines in all panels in Figure 2.8).

From the statistical study, disagreement between the DMSP and Polar UVI boundaries may reach up to 3.5°, although typically the difference is nearly zero [89].

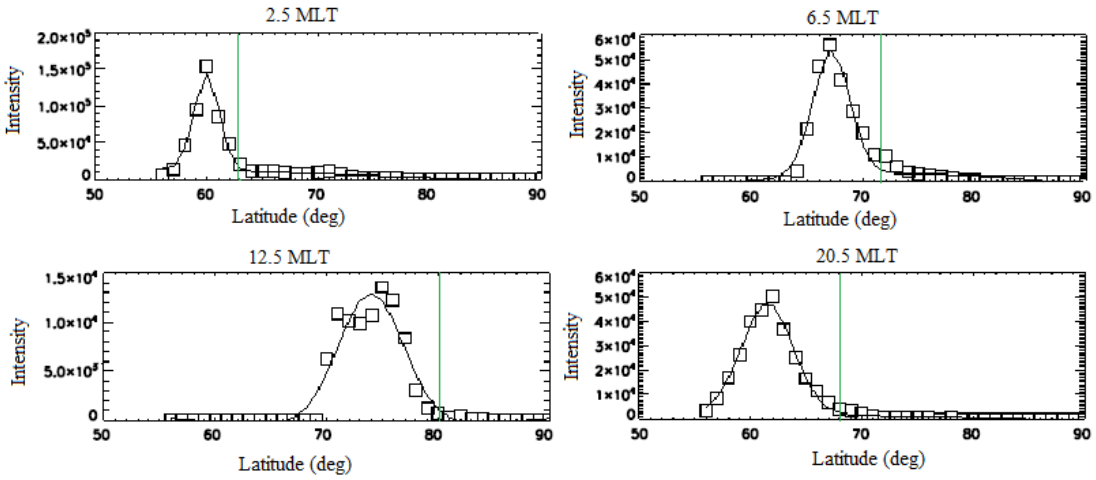

Figure 2.8: The square symbols represent intensities averaged into a 1-hour MLT sector at different latitudes. The curve represents single Gaussian fit with quadratic background and the green solid line denotes the latitudinal location of OCB at 2.5, 6.5, 12.5 and 20.5 MLT.

2.6.3 IMAGE FUV Observations

Boakes et al., [92] and Longden et al., [93] implement a function with two Gaussian components instead of one Gaussian component to get the better fit of the intensity profile and implemented the technique on IMAGE FUV measurements. The OCB detected by the IMAGE-FUV was obtained from the British Antarctic Survey website [91].The most poleward boundary of the auroral oval are calculated from the double Gaussian function with some criteria and can be obtained from the website `www.antarctica.ac.uk/bas_research/our_research/az/magnetic_reconnection`. The calculated boundaries are calibrated with the DMSP satellite data to estimate the OCB. The temporal resolution of the IMAGE FUV instrument was about 2 min, similar to that of SuperDARN.

Figure 2.9 shows the images of UV aurora detected by three FUV detectors. Like the OCBs measured from the directional derivative of the convection flow

speed, OCBs measured from the three IMAGE detectors are also shown along each MLT meridian (Figure 2.9) recorded at 8:16:36 UT on November 04, 2001. Detected from the three cameras, the brightest UV emission occurs in the midnight sector and the emissions extend to approximately 75° magnetic latitude. The peak intensity is 1500 Rayleigh. Intensity varies in the meridian direction, however, emission is observed in similar latitudes. From morning to afternoon, the intensity is diminished. Observations from the two spectrographic imagers indicate that the luminous region spans a much larger range of magnetic latitude and magnetic meridians than the wideband UV auroral emission (to which the WIC camera is sensitive), and is particularly extended in the dusk sector.

In all panels of Figure 2.9, the OCBs are indicated by filled white dots. The spatial resolution measured from the WIC channel (Figure 2.8b) is better than that of the spectrographic imagers (Figure 2.9a and 2.9c) [94] . WIC and SI-13 detectors detected electron auroral emissions whereas SI-12 measured emissions in the 128 nm band that originated from proton precipitation.

2.6.4 Doppler Spectral Width Boundary

An earlier study showed that the two statistical distributions of the Doppler spectral velocities within a range gate, Lorentzian and Gaussian distribution are typically found in different locations in the ionosphere [44]. The spectral width boundary (SWB) is defined as a sharp transition from low to large spectral widths in the Doppler backscatter. A Gaussian distribution with a mean value of $\sim$ 200 m/s is generally seen poleward of the SWB while an exponential distribution with a mean value of $\sim$ 50 m/s can be seen equatorward of the SWB. As the probability distribution of the spectral width values above and below the spectral width boundary are broad, latitudinal transitions measured from the threshold technique [95] are crucial to determine [51]. Therefore the uncertainty of determining the SWB is related with the thickness of the tran-

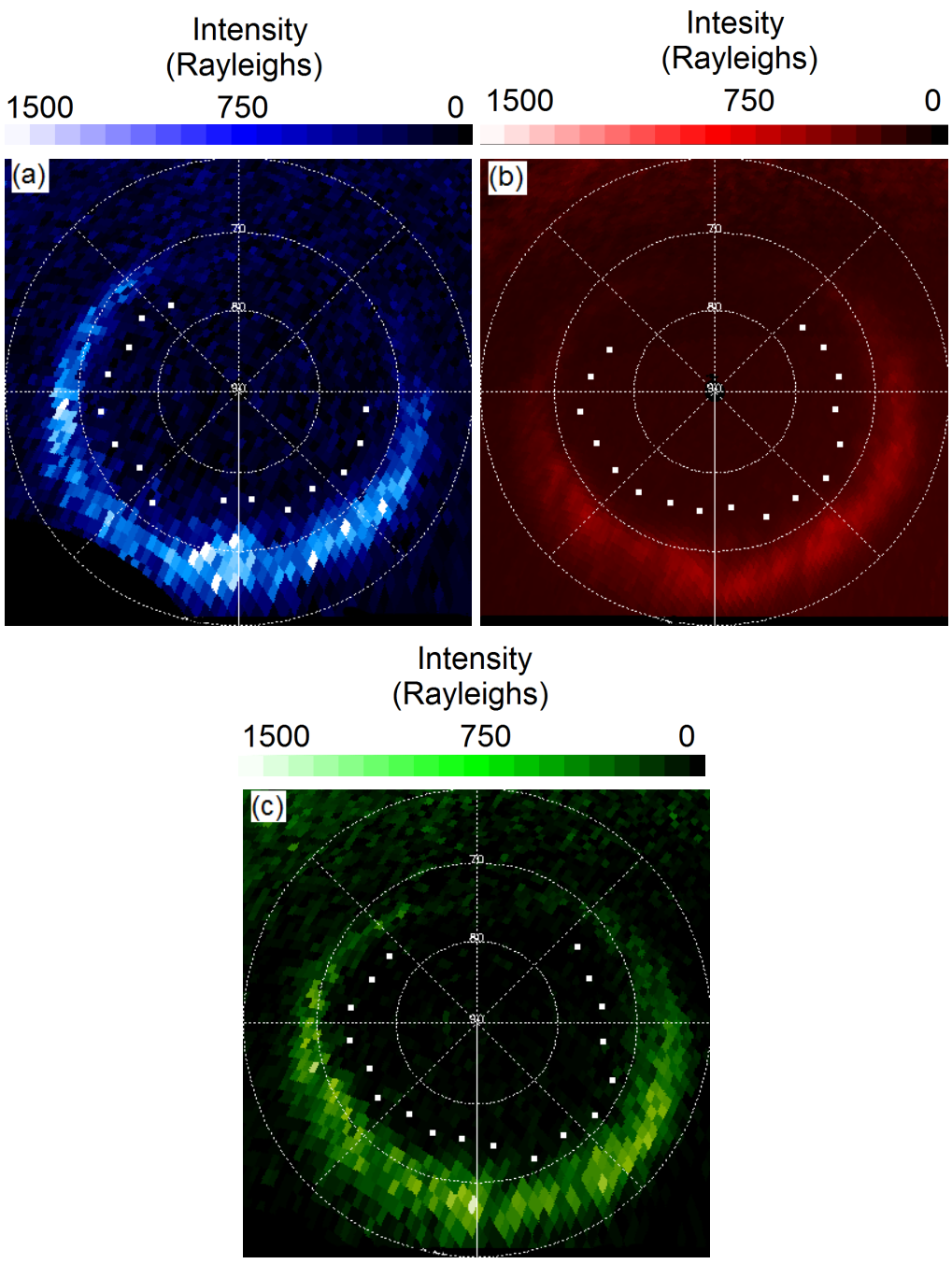

Figure 2.9: Images of UV aurora detected by FUV SI-12, WIC, and SI-13 (a, b, c, respectively) instruments on board the IMAGE spacecraft at 8:16:36 UT on November 04, 2011. Auroral intensity is color coded where the brightest color indicates the most energetic particle precipitation region. The lines of constant latitude are in 10 degree increments from 60° to 90°, with noon at the top and midnight at the bottom. The white dots represent the OCB positions at each MLT, as described in the text.

sition. Multiple threshold values are tested to determine the SWB and in this thesis a value of 200 m/s is used as the threshold value in determining the OCB proxy. Moreover, sometimes it is difficult to find the OCB proxy via the SWB due to lack of backscatter in the region of low spectral widths. However, the nature of the SWB depends on the MLT [50].

An attempt to determine an OCB proxy is depicted in Figure 2.10 which shows the field of view of the Doppler spectral width of the most meridional beams in the Northern Hemisphere at 8:14–8:16 UT, November 04, 2001 with a 200 m/s threshold value. A boundary between low spectral width and high spectral width above 200 m/s is considered to be an OCB proxy. Doppler spectral width echoes detected from Hankasalami and Goose Bay radars in the morning and noon sectors could not determine OCB due to lack of sufficient backscatter at the transition from low to high spectral widths.

2.6.5 Multi-Spacecraft Solar Wind Observation

The solar wind conditions can be obtained from the Advanced Composition Explorer (ACE) spacecraft. The ACE spacecraft was launched on August 25, 1997, to continuously study the energetic particles in the solar wind using six high-resolution sensors and three monitoring instruments. The dataset of the solar wind dynamic pressure was taken from the OMNI database which comprises solar wind measurements from a variety of spacecraft time-delayed to the magnetopause. The resolution of IMF data from the ACE spacecraft is 16 seconds while the resolution of OMNI database is 1 minute. The dynamic pressure of the solar wind is $(\rho V^2)_{sw}$ where ρ and V are the density and velocity of the solar wind, respectively. The smaller dynamic pressure of the solar wind will result in a lower reconnection rate between southward IMF and the Earth's Field.

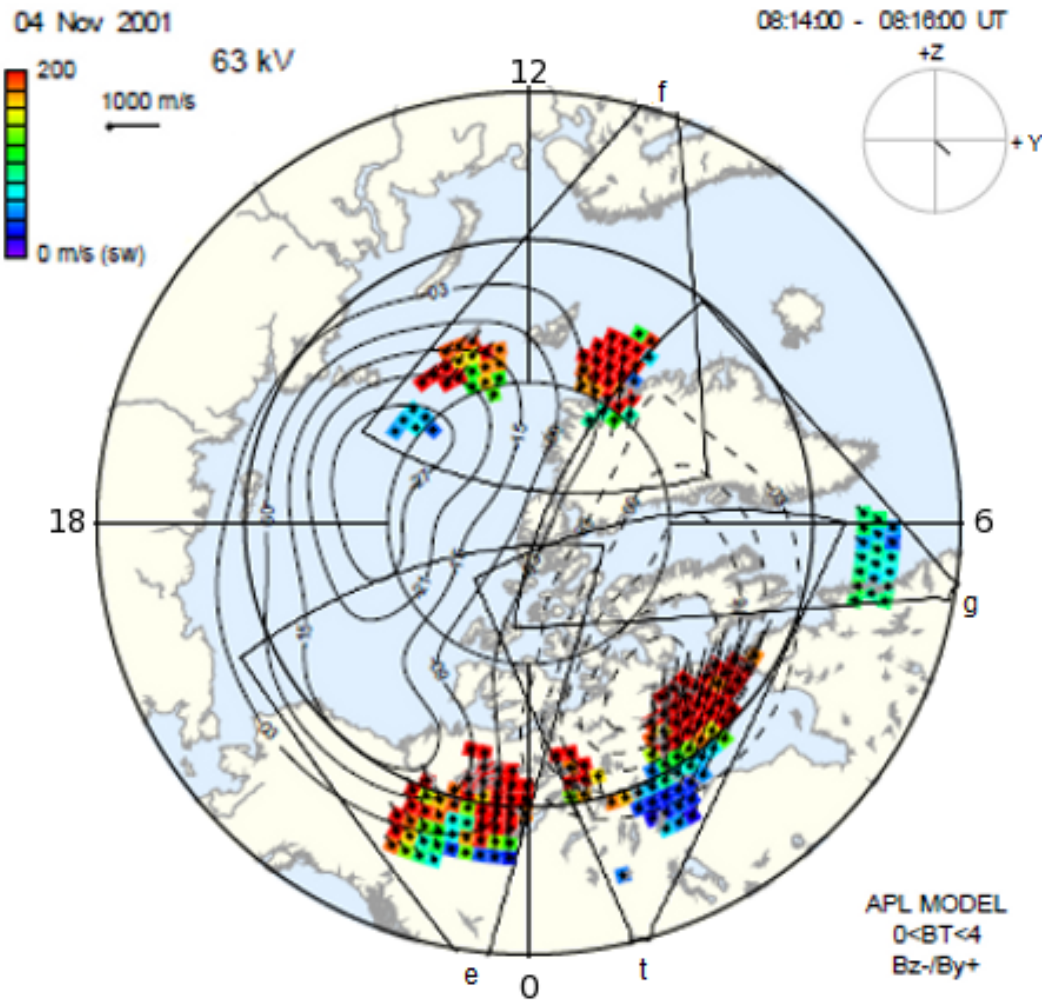

Figure 2.10: Field of view of the most meridional beams from four SuperDARN radars in the Northern Hemisphere at 8:14-8:16 UT, November 04, 2001, with a Doppler spectral width boundary taken at a 200 m/s threshold value. Geomagnetic latitudes from 60° to 80° latitude are shown with solid black lines, and radial lines represent MLT meridians at midnight, morning, noon, and evening, with noon at the top and midnight at the bottom. The four radars, Pykkvibær, Hankasalami, Goose Bay, and Saskatoon are labeled e, f, g, and t, respectively.

Chapter 3

Evaluation of the SuperDARN directional derivative technique for identifying the open-closed field line boundary during a southward interval of the interplanetary magnetic field

The open-closed field line boundary (OCB) will be identified by utilizing directional derivatives of SuperDARN ionospheric convection flow over a four and a half hour interval on Nov 04, 2001, during which the interplanetary magnetic field was southward with a magnitude between -2nT and -6nT and the dynamic pressure varied from 1.1 nPa to 3.1 nPa; the technique is discussed in section 2.5.1 in Chapter 2. The OCB proxy associated with the peak in the directional derivative of flow is evaluated via comparison with other indicators of the OCB such as the poleward boundary of ultraviolet emissions from three FUV detec-

tors onboard the IMAGE spacecraft, SuperDARN spectral widths, and satellite particle precipitation measurements from the low-altitude Defense Meteorological Satellite Program (DMSP) spacecraft. Good comparison is found between the location of the peak in the directional derivative of SuperDARN flow and the poleward boundary of ultraviolet emissions and the particle precipitation boundary (PPB) measured by the DMSP spacecraft; however, the Doppler spectral width boundary (SWB) is found to be unreliable as an OCB proxy during the interval.

3.1 Solar Wind Conditions

Figure 3.1 shows the solar wind conditions as measured from the Advanced Composition Explorer (ACE) spacecraft for the interval 7 UT to 12 UT on November 04, 2001. The average propagation delay from ACE has been estimated to be $\sim$ 74 minutes based on an average solar wind speed 318 km/s during the interval, however, the ACE spacecraft data are not time lagged in the Figure 3.1. The dynamic pressure is taken from OMNI and therefore is delayed to the magnetospher. The solar wind conditions were fairly steady during this interval. The IMF B_z component was negative, ranging from -2 to -5 nT, for most of the period of observation and positive for only a short period of time. The interplanetary magnetic field (IMF) B_y component was positive, ranging from 2–5 nT, throughout the period of observation, with some short-lived negative values. The dynamic pressure was fairly steady, hovering around 1.5 nPa for the entire interval. The dataset of the solar wind dynamic pressure was obtained from the OMNI database.

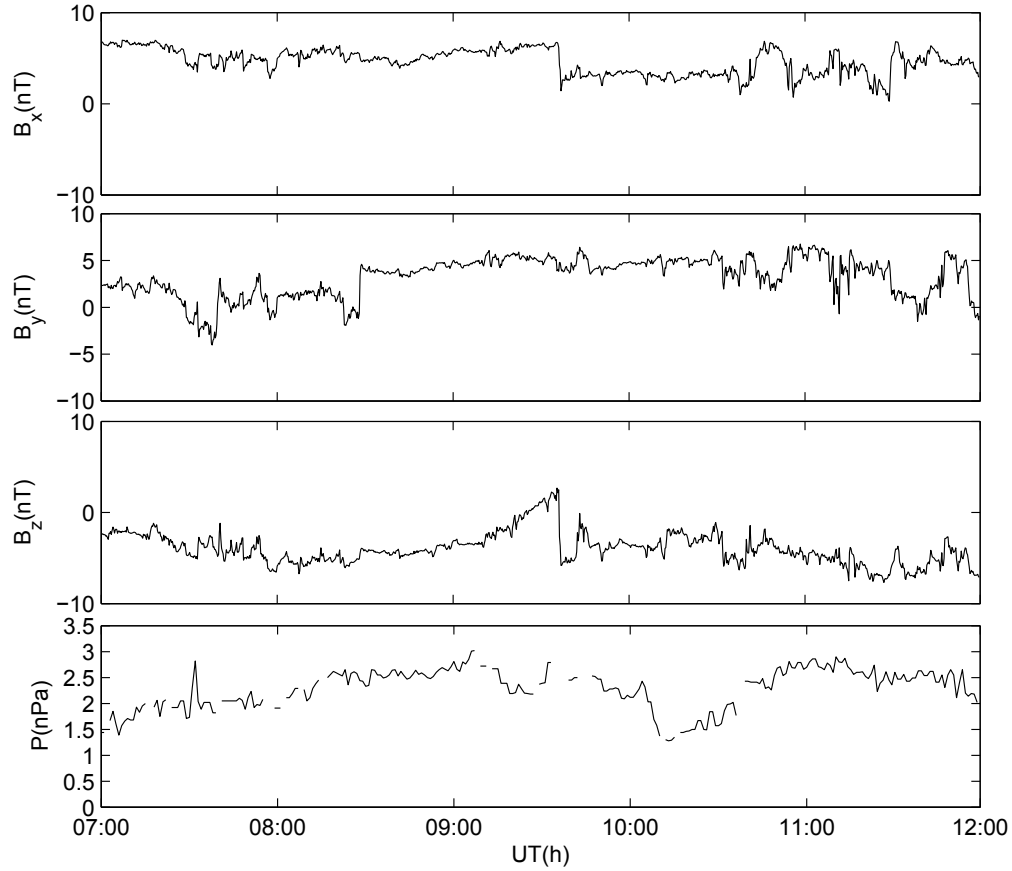

Figure 3.1: Interplanetary magnetic field (IMF) condition on November 04, 2001. The top three panels show the IMF measured by the ACE spacecraft with no time delay. The fourth panel represents the solar wind dynamic pressure delayed to the magnetosphere; data were acquired from the OMNI database and comprise measurements taken from the Geotail spacecraft.

3.2 Comparisons of SuperDARN OCB with other Techniques

To determine if positive maxima in the convection flow directional derivatives can be used as indicators of the OCB, we compare OCB derived from the peak in the directional derivative of flow results for this event to the three

other OCB techniques outlined in Chapter 2. For illustration comparisons are shown at select universal and magnetic local times during the four hour event interval. A statistical comparison between the OCB locations determined via the SuperDARN flow directional derivative technique and the IMAGE FUV poleward boundaries is included.

3.2.1 Comparison of OCB derived from SuperDARN and IMAGE FUV

Figure 3.2 shows 4 snapshots in time, at one hour intervals, of the SuperDARN convection flow directional derivative map including the identified OCB locations shown as plus signs. For comparison, these SuperDARN derived OCB locations are overlaid with the IMAGE FUV OCB proxy locations in Figure 3.3.

The figures are presented in the same format as that in Figures 2.4, with uniform magnetic latitude (starting from 60^o) and a magnetic local time coordinate system, with magnetic midnight located at the bottom and noon at the top of each image. The time points are indicated at the top-right of each panel. Note the time-points for SuperDARN and IMAGE are not identical but are as close as possible. In all panels in Figure 3.3 the points labeled as red-crosses, blue-pluses, green diamonds, and black-boxes correspond to OCB proxies determined from WIC, SI-12, SI-13, and the peak in the directional derivative of the SupeDARN flow, respectively. Due to data gaps in the SuperDARN backscatter and weak FUV emissions observed by IMAGE it is not possible to identify OCB proxy at all magnetic local times. This is the reason for data point gaps in Figure 3.3. For example, at 07:44:00 UT for SuperDARN (07:43:53 UT for IMAGE spacecraft), the OCB could not be measured from SuperDARN in the noon to dusk sector (12.5–19.5 MLT) and early morning sector (3.5–5.5 MLT) while ultraviolet emissions could not be recorded between 10.5 and 14.5 MLT.

During this particular event, the peak in the directional derivative of flow measured from SuperDARN could not be determined in the dusk sector as there are little or no backscatter data from radars at these MLT and the low order of fit is more dependent on the observed backscatter, as described in section 2.5.1. Similarly, ultraviolet emissions could not be used to determine the OCB proxy in the dayside region during the interval.

For the Universal time points shown in Figure 3.3, the directional derivative of SuperDARN flow OCB locations are in fairly good agreement with the OCB measured from the IMAGE FUV detectors in the midnight to dawn to noon magnetic local time sectors. However, in the pre-midnight sector the SuperDARN OCB is significantly equatorward of the IMAGE OCB proxies particularly at the earlier Universal time points. For example, at 08:44 UT (top right panel of Figure 3.3) the SuperDARN OCB is approximately 8° equatorward of the IMAGE OCB proxies at 21.5, 22.5 and 23.5 MLT. In the corresponding directional derivative of the convection flow speed map, shown in the top right panel of Figure 3.2, there is a secondary peak in the directional derivative of flow at higher latitudes in the pre-midnight region consistent with the IMAGE OCB proxies. Also note that this secondary peak falls within the dawn convection cell. This suggests that the directional derivative of SuperDARN flow OCB determination in the pre-midnight sector is more complicated than at other local times, to be discussed in Chapter 5.

To provide a more detailed comparison of the OCB proxies determined from the SuperDARN flow directional derivative technique, the Doppler SWB, and the IMAGE FUV poleward boundaries, the temporal evolution of the OCB proxies at select magnetic local times are shown in Figures 3.4 and 3.5. Figure 3.4 shows the temporal evolution of the magnetic latitude of the OCB during the midnight (0.5 MLT), post-midnight (2.5 MLT) and morning (7.5

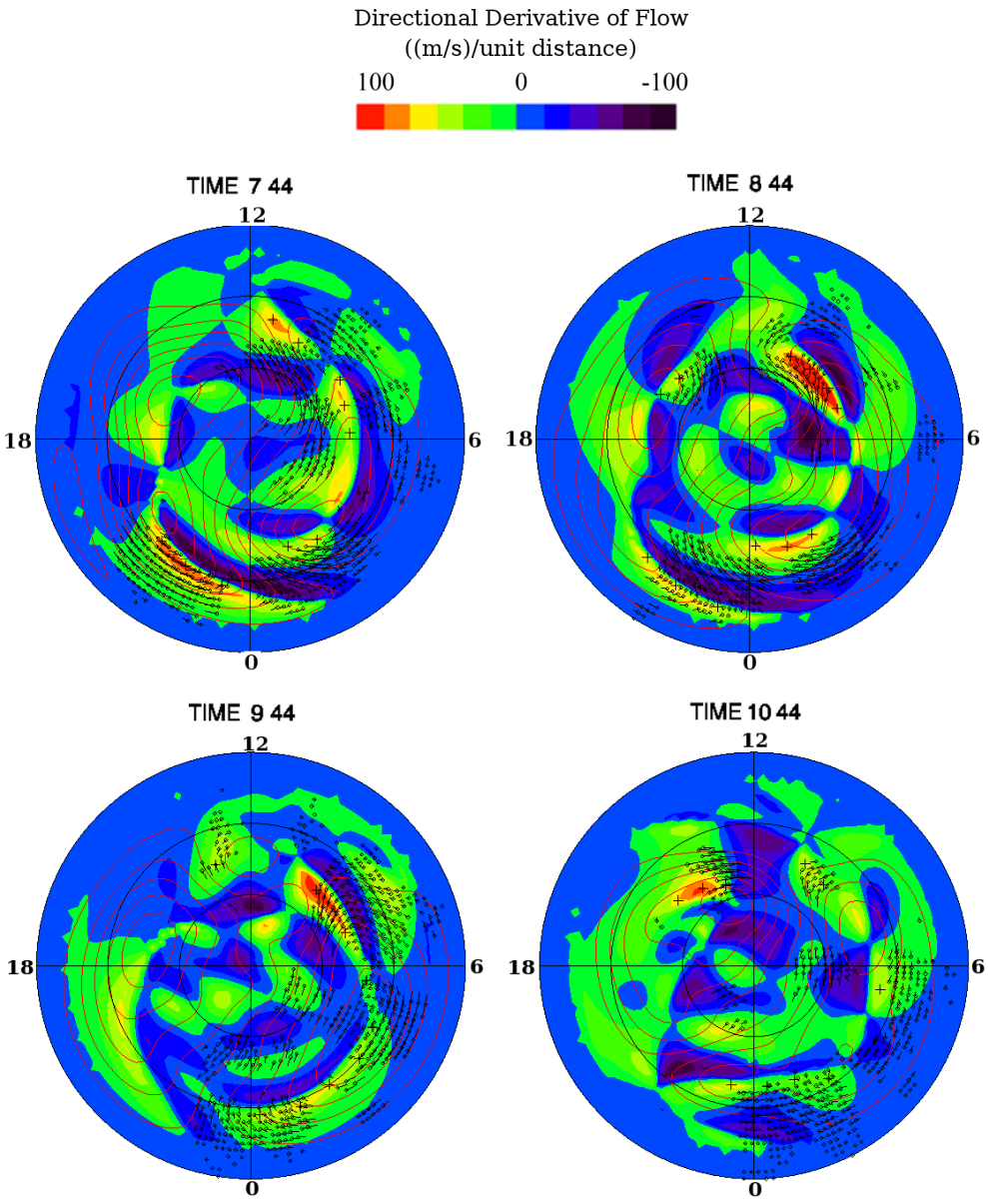

Figure 3.2: SuperDARN convection flow directional derivatives taken at 1 hour intervals from 07:44-10:44 UT on November 04, 2001 in magnetic latitude (MLAT)–magnetic local time coordinates. The directional derivative of flow is color-coded according to the color scale. Solid black circles represent 60°, 70°, and 80° MLAT, and radial lines represent MLT meridians at midnight, morning, noon, and evening, with noon at the top and midnight at the bottom. The square dots at the ends of the vectors indicate the vector locations and the lines show the vector direction and magnitude. The red contours at dusk (dawn) are associated with negative (positive) values of electrostatic potential. The magnitudes of the potential contours start from 3 kV with 6 kV increment between lines. OCBs are labeled with a plus sign along the magnetic meridian.

MLT) sectors, while Figure 3.5 corresponds to the afternoon (15.5 MLT), and pre-midnight (21.5 MLT), and midnight (23.5 MLT) sectors. The six different MLTs were chosen based on having the highest amount of data in each quarter of the sector. Although the temporal resolution of the instruments is two minutes, 10 minute averages of the OCB locations have been plotted in Figures 3.4 and 3.5. The reason for averaging the OCB locations over 10 minute intervals is to make the plots easier to view by reducing the number of plotted points and to provide an estimate of the measurement error in the OCB locations by taking the standard deviation over the 10 minute intervals. The standard deviations were typically 0.35°, 0.62°, 0.73°, 0.68°, 0.49° for the SuperDARN flow directional derivatives, WIC, SI-12, SI-13, and SuperDARN SWB OCB proxies, respectively.

The OCB proxy from the directional derivative of SuperDARN convection flow in general follows the temporal evolution of the FUV detectors (Figure 3.4 and Figure 3.5). It is worthwhile to note that although the OCB proxies measured from the strong directional derivative in the premidnight sector (from 21.5 to 23.5 MLT) at 08:44 UT were located around 65° for the 2 minute time points, the latitudinal location does not appear in Figure 3.5 as the OCB proxies are 10 minute averages and the peak in the directional derivatives were located $\sim$ 74° for other time points in the 10 minutes intervals.

It is interesting to note that both SuperDARN and IMAGE show similar variations in the OCB latitudes with time. At 15.5 MLT (upper panel of Figure 3.5), it is evident that the OCB location is fairly steady around 75° magnetic latitude. Latitudinal motion of the OCB is significant ($\sim$ 8° latitude) at midnight, as seen from the OCB measurements at 0.5 MLT and 23.5 MLT during the interval. This indicates that the boundary was varying at midnight but steady on the day side of the Earth (at 7.5 and 15.5 MLT, lower panel of Figure 3.4

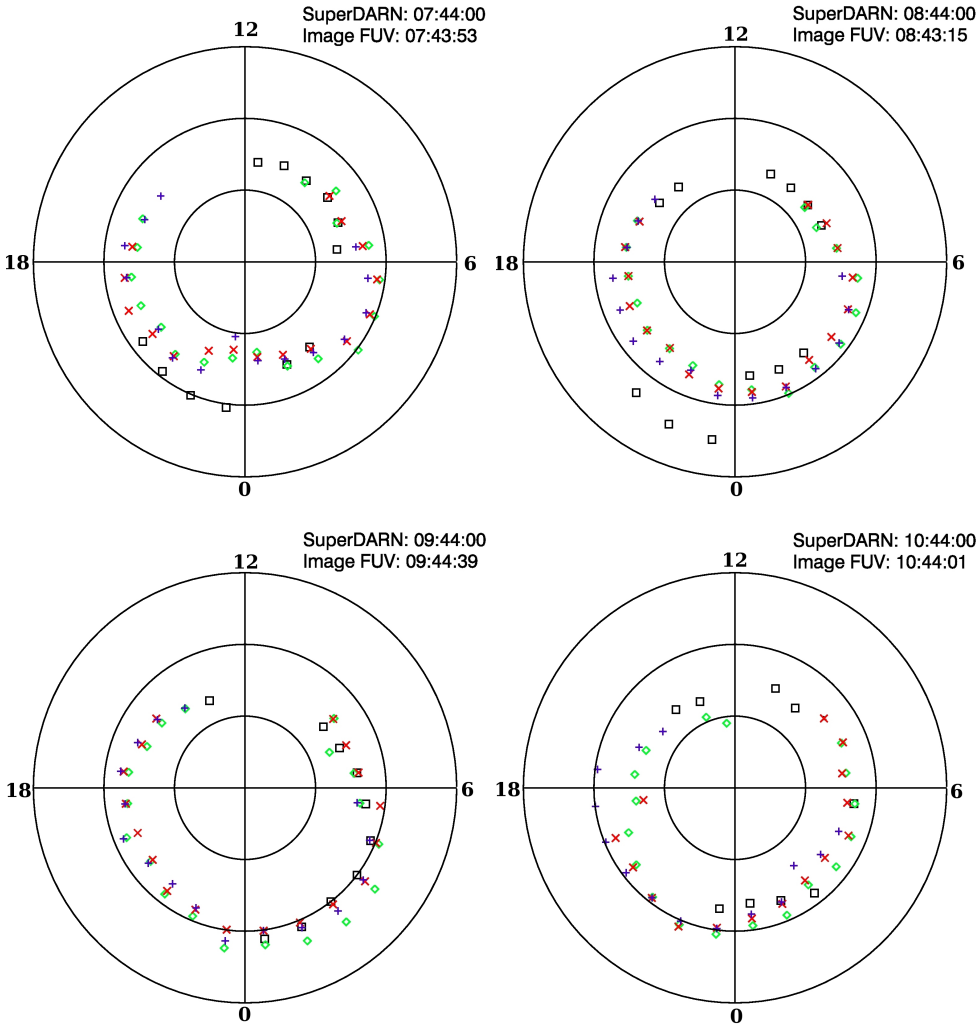

Figure 3.3: OCBs defined by the SuperDARN convection flow directional derivative (black-box), the WIC (red-cross), the SI-13 (green-diamond), and the SI1-2 (blue-plus) taken at 1 hour intervals from 07:44-10:44 UT on November 04, 2001. All panels are presented in magnetic latitude (MLAT)–magnetic local time coordinates. Solid black circles represent 60°, 70°, and 80° MLAT, and radial lines represent MLT meridians at midnight, morning, noon, and evening, with noon at the top and midnight at the bottom. The top-right corner of each panel indicates the time at which the OCB was measured from the poleward boundary of the UV emission and the IMAGE FUV detectors and SuperDARN.

and upper panel of Figure 3.5, respectively). Both Figure 3.4 and Figure 3.5 show that the OCB was initially poleward and moved equatorward from 08:00 UT to 10:00 UT at midnight. The equatorward motion of the OCB during the interval between 8 UT to 10 UT indicates an expansion of the polar cap. A poleward motion of the OCB indicates a contraction of the polar cap at midnight starting after $\sim$ 10 UT. The contraction of polar cap in the nightside may be associated with the change in IMF B_z. For example, at 0.5 MLT the the latitudinal location of OCB measured from the SuperDARN flow directional derivatives went from $\sim$ 67.5° at 10:14 UT to $\sim$ 73.5° at 10:50 UT (top panel of Figure 3.4) while the IMF B_z increased from $\sim$ -3.5 nT to $\sim$ 2.5 nT during the interval (third panel of Figure 3.1).

In a few cases, SuperDARN OCBs were either poleward (08:20–08:40 UT at 0.5 MLT) or equatorward (09:50–10:10 UT at 0.5 MLT) of IMAGE FUV measurements, albeit $\sim$ 2° magnetic latitude difference. Although the latitudinal locations of the SuperDARN OCBs varied $\sim$ 3° latitude between the interval of 08:10 and 08:20 UT, OCB measurements from the SuperDARN convection flow directional derivative indicate that the boundaries agree with the IMAGE OCB proxies at almost all magnetic local times.

Figures 3.4 and 3.5 indicate that the directional derivative of SuperDARN convection flow technique is more reliable than the SWB to determine the location of the OCB during this interval as the SWB OCB proxy is significantly equatorward of the IMAGE FUV OCB. The SuperDARN flow directional derivative and SWB techniques will be compared further in section 3.2.2.

To further investigate the similarity of the latitudinal variations of the OCB with time for the different techniques, the correlation coefficients between the directional derivative of SuperDARN flow technique and each of the IMAGE

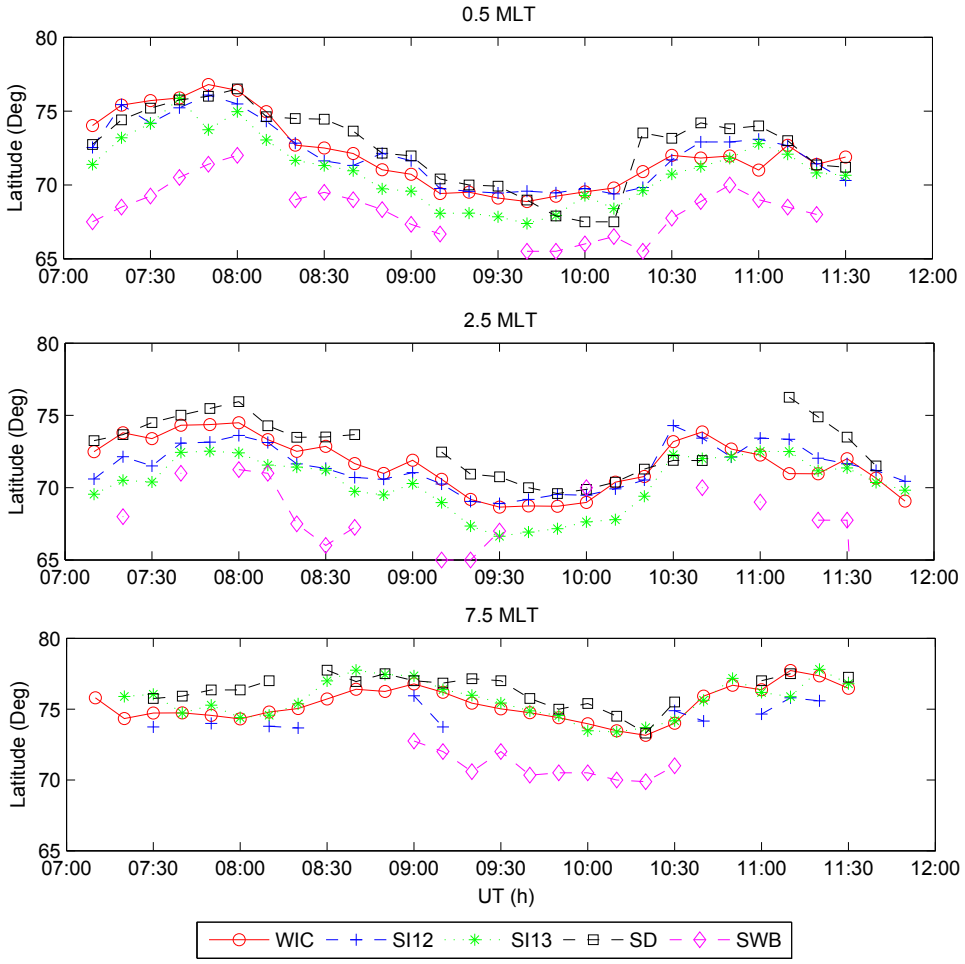

Figure 3.4: Temporal evolution (with 10 minute intervals) of latitudinal locations of the OCB measured from the three IMAGE FUV detectors, the SuperDARN flow directional derivatives, and the SWB. The upper, middle, and lower panels show OCB locations at 0.5 MLT, 2.5 MLT, and 7.5 MLT sectors respectively. The latitude ranges on the Y-axis are between 65° and 80° magnetic latitude. In each case, OCBs measured from three ultraviolet cameras are labeled 'red-circle' (corresponding to WIC), 'blue-plus' (corresponding to SI-12), and 'green-star' (corresponding to SI-13). The directional derivative of SuperDARN flow measurements and Doppler SWBs are superimposed as 'black-box' and 'magenta-diamond' shapes.

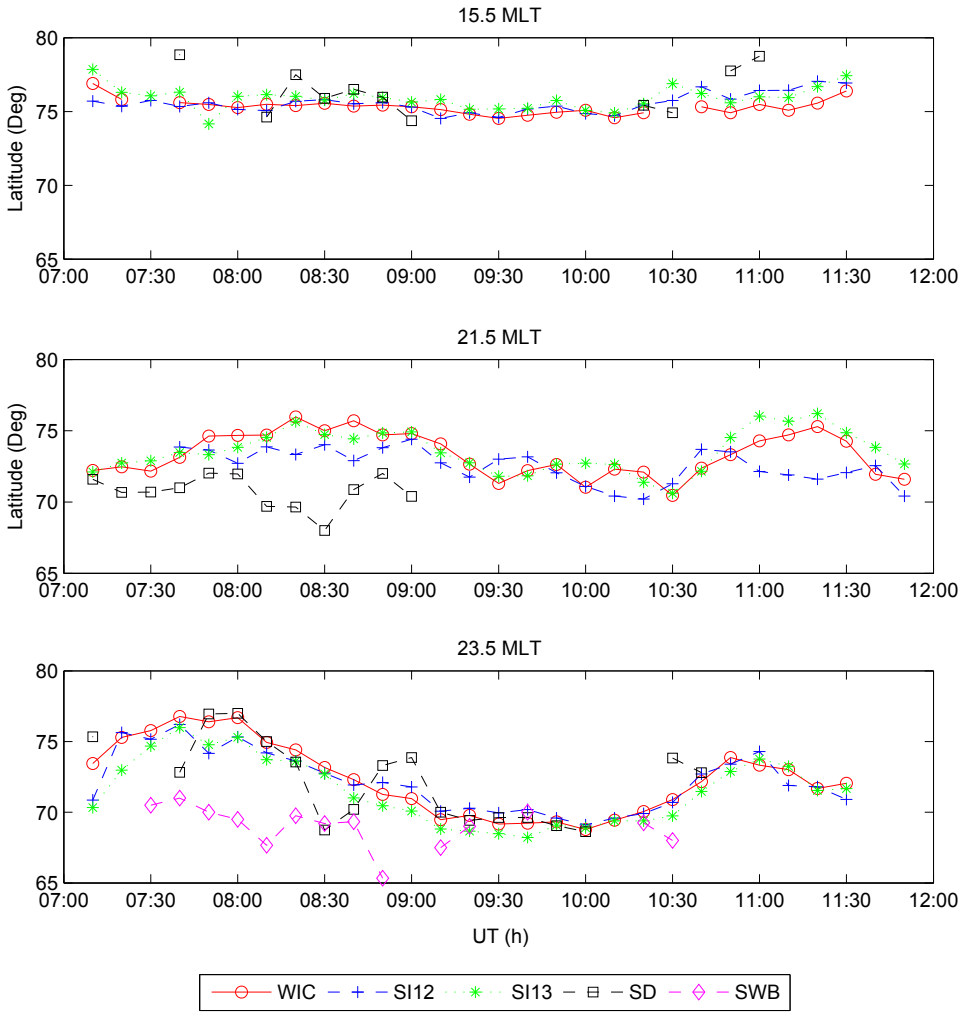

Figure 3.5: Temporal evolution (with 10 minute intervals) of the latitudinal location of the OCB measured from the three IMAGE FUV detectors, the SuperDARN convection flow directional derivatives, and the SWB. The upper panel shows the afternoon (15.5 MLT) sector, middle panel shows the pre-midnight (21.5 MLT), and the lower panel shows the midnight (23.5 MLT) sector OCB locations during the specific period of time. The figure is presented in the same format as that in Figure 3.4.

FUV OCB proxies are calculated at each MLT and are shown in Figure 3.6 (a). The correlations are high, above values of 0.5, at all MLTs with data coverage except at 4.5 and 5.5 MLT where coefficient values are 0.4 and 0.3, respectively. Correlation coefficients are missing from 8.5 MLT to the pre-midnight sector due to insufficient data for statistical analysis. The highest correlations of 0.75 are found with the WIC data, typically corresponding to the Lyman-Birge-Hopfield (LBH) region of the UV spectrum ($\sim$ 140–180 nm). To provide a measure of how close the agreement is between the different techniques, the square root of the mean of the squares of the deviations between the SuperDARN flow directional derivative OCB locations and the three IMAGE OCB proxies are calculated at each MLT. The lower panel of Figure 3.6 shows these root mean square deviations which were calculated using the 10 minute data point averages as shown in Figures 3.4 and 3.5. SuperDARN-WIC pair data are marked 'WIC' (red-circle), SuperDARN-SI-12 pair data are marked 'SI-12' (blue-plus), and SuperDARN-SI-13 pair data are marked 'SI-13' (green-star). The root mean square deviations range from 0.8° to 3° magnetic latitude with the WIC instrument typically having the lowest root mean square deviation with SuperDARN. Relatively higher root mean square deviation values are observed in the pre-midnight sector, a trend that was also evident in Figure 3.3 (07:44 UT and 08:44 UT), and Figure 3.5 (at 21.5 MLT). The lowest root mean square deviation occurred in the morning (6.5 and 7.6 MLT). This is also evident in figure 3.4., where the SuperDARN OCB was either co-located close to the OCB at 7.5 MLT detected from the WIC imager during the entire interval.

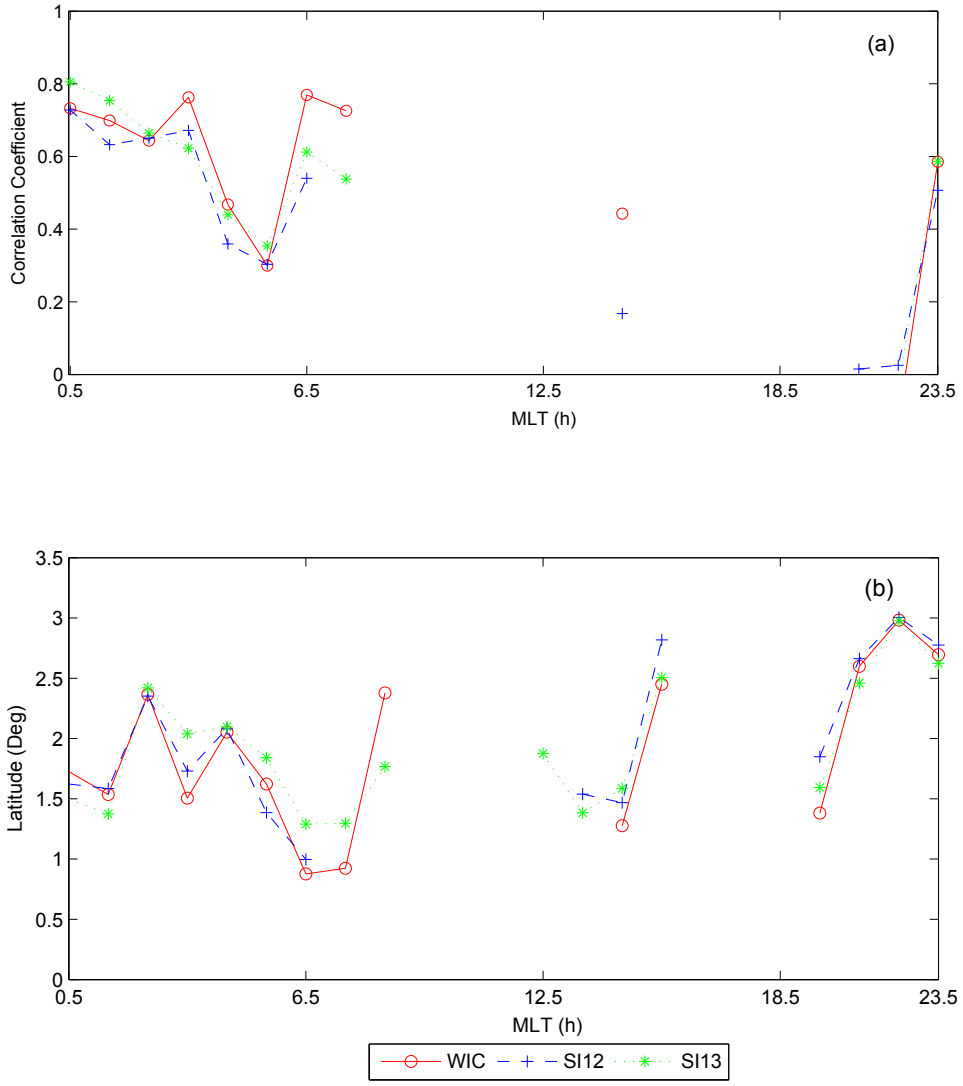

Figure 3.6: Correlation coefficients (panel a) and root mean square deviation (panel b) between SuperDARN and the three IMAGE FUV detectors at each MLT. In each case, the points labeled 'red-circle,' 'blue-plus,' and 'green-star' correspond to WIC-SuperDARN, SI-12-SuperDARN, and SI-13-SuperDARN correlations. In the lower panel, the root mean square deviations are measured in magnetic latitude.

3.2.2 Comparison of OCB Proxies Derived from Doppler SWB, SuperDARN, and IMAGE FUV

One example time point for determining Doppler SWB from this event is described in chapter 2, section 2.6.4. OCB proxies from Doppler SWBs are compared with the peak in the directional derivative of SuperDARN flow and IMAGE FUV data in four different MLT sectors in Figures 3.4 and 3.5. It is evident from the figures that OCB proxies derived from Doppler SWBs are in general at much lower latitudes, which agrees with previous studies [53]; [54] while OCB derived from the peak in the directional derivative of SuperDARN flow technique agree well with OCB proxies derived from IMAGE FUV detectors. The average latitudinal difference from the Doppler SWB with the IMAGE FUV measurements was 4° equatorward with a high of 7° (measured at midnight).

Since only meridional beams are used to determine Doppler SWBs, the data coverage may not be the same as data obtained with the SuperDARN convection flow directional derivative technique. For example, the Doppler SWB could not be determined at 15.5 MLT and 21.5 MLT (Figure 3.5) and few data were present for other local times.

3.2.3 Comparison OCB Proxies with the DMSP PPB

Although the DMSP spacecraft particle precipitation technique is the most accurate way to measure the OCB, the boundary is sampled infrequently and measurements could not be compared statistically. As a single location of the OCB could be identified by the DMSP satellites during each overflight, only four OCB locations were identified. Moreover, the OCB locations are not precisely at the points measured by the ultraviolet detectors and SuperDARN.

Figure 3.7 shows the location of the OCB measured from DMSP spacecraft, multi wavelength observations of the ultraviolet detectors, and SuperDARN HF radar observations at particular UT/MLT. For simplicity, we take the closest MLT and UT with the range of ± 0.5 MLT and ± 2 min, respectively.

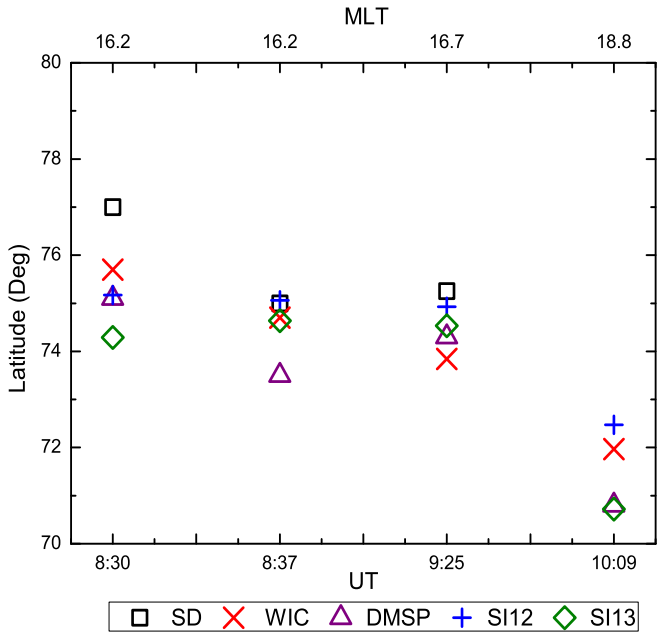

Figure 3.7: Latitude of DMSP particle precipitation boundary over time. 'Box,' 'triangle,' 'red-cross,' 'blue-plus,' and 'green-diamond' correspond, respectively, to OCBs measured by the SuperDARN convection flow directional derivative, the PPB detected by DMSP spacecraft, the poleward boundary of UV emission from the WIC, SI-12, and SI-13 detectors.

From the four observations it appears that the OCB measured from the spectrographic imagers are well matched with DMSP measurements in most cases. However, previous studies showed the SI-12 OCBs to be generally well matched with DMSP PPB in the predawn sector and SI-13 and WIC OCBs in agreement in the remaining MLT [92]. We observed that all of the ultraviolet detectors OCBs agree within $\sim 1^{\circ}$ with the DMSP OCB from 16 MLT to 19 MLT. The OCB proxy estimated by SuperDARN flow directional derivative is situated at

higher latitude and the SuperDARN had no backscattering during the fourth observation. Due to the relatively low number of DMSP-SuperDARN OCB proxies, it is difficult to compare the results statistically. However, the observations indicate that the latitude difference between the SuperDARN OCB proxy and the PPB detected by the DMSP is small, only 1.67° poleward on average.

3.3 Conclusions

In this Chapter it has been shown that at certain local times when the IMF B_z component is negative and B_y is slowly varying and positive, the positive maxima in the directional derivative of SuperDARN flow can be a good indicator of the open-closed field line boundary. We present case study observations of the OCB using space- and ground-based instruments and compare our technique of estimating the location of the open-closed sepratrix at all magnetic local times with existing techniques in all sectors based upon data from November 04, 2001.

It has been shown that the peak in the directional derivative of SuperDARN flow can be used as a reasonable OCB proxy during the southward IMF condition. This conclusion is supported by the high correlations and small root mean square deviations found between the SuperDARN flow directional derivative measurements of the OCB and the UV OCB proxies from multiple wavelength bands. Since the OCB measurement from the wide-band and spectrographic imagers of the IMAGE spacecraft are roughly co-located with a 2–3° magnetic latitude difference, the IMAGE FUV detectors can be used interchangeably to estimate the OCB position. During the interval of interest, OCB indicators at midnight show an initial poleward motion followed by an equatorward motion of the night side OCB and then another interval of poleward motion (Figures

3.4 and 3.5) which can be associated with changes in IMF B_z and solar wind dynamic pressure. Frey et al., (2004) [94] detected two substorm onsets at 10:13 UT, and 10:54 UT. Therefore the equatorward motion from $\sim$ 8 UT to $\sim$ 10 UT is an extended growth phase prior to substorm. The method of identifying substorm onset will be discussed in chapter 4. However, the observations indicate that the relationship of the Doppler SWB to the OCB is ambiguous in the midnight and dawn sectors which are also evident from a previous result [53]; [49]. The OCB measured using in situ particle measurement, albeit not globally applicable, also indicates that the locations of the OCB estimated from the SuperDARN flow directional derivatives were approximately co-located (at least to within 1–2° latitude) in the MLT sectors traveled by DMSP spacecraft during the case study. The results indicate that OCB proxies from the SuperDARN convection flow directional derivatives agree well with the satellite measurement techniques during the southward IMF condition. Our overall understanding of the relationship of the OCB with the maximum in the directional derivative of SuperDARN flow indicates that the proposed technique can be a potential candidate to estimate the OCB and has the ability to determine the OCB instantaneously and globally. Therefore the directional derivative of SuperDARN convection flow technique will be examined further in Chapters 4 and 5 during other intervals of southward IMF that correspond to substorm onset.

Chapter 4

Identifying the Night Side Open-Closed Field Line Boundary during a Substorm Onset

The convection flow directional derivative technique was tested and compared with other methods of detecting the open-closed field line boundary (OCB) during a substorm growth phase in chapter 3. In this chapter the position of the open-closed field line boundary (OCB) derived from the peak in the directional derivative of SuperDARN plasma flow is compared with the results from ultraviolet imagers on IMAGE and Polar spacecraft during two substorm event periods. Doppler spectral width observed by the SuperDARN were not tested as a proxy for locating the OCB during the events, as the method is not trustworthy in the dawn sector and in the midnight region. During the testing interval, the low altitude DMSP spacecraft did not find an OCB as the spacecraft was located at different UT and MLT. Therefore this technique is not discussed in this chapter.

This study aims to detect the OCB during two substorm events. Selection of the substorm intervals is presented in section 4.1. Observations of the auroral emission for a time interval of $\sim$ 60 minutes before and after the auroral intensification (sudden brightening) are discussed in sections 4.3.1 and 4.4.1. OCB positions measured with the convection flow directional derivative technique based on SuperDARN data and the data gathered from ultraviolet detectors on spacecraft are compared in section 4.3.1 and 4.4.2. An initial selection of the first event was based on substorm observations estimated from ultraviolet imager and ground magnetometer observations. The second event was reported in a previous study, in which a list of substorm onsets detected with ultraviolet imaging from Polar spacecraft was discussed [88]. The SuperDARN observations were examined in the night sector during the two substorm onset periods to determine the open-closed separatrix.

4.1 Selection of the Substorm Onset Intervals

Ultraviolet imagers and magnetometers can be used to detect the onset of a substorm. Table 4.1 shows two substorm events detected from different observers. Frey et al. (2004) [94] identified 2437 substorm onsets with FUV detectors and Liou (2010) [88] identified 2539 auroral onsets in both hemispheres using Polar UV imaging. The methodologies used to identify substorms with IMAGE far UV detectors and Polar UV detectors are slightly different, although both ultraviolet detectors detect optical auroral brightening to find the substorm onset [88]. Using the IMAGE FUV detectors, Frey et al. (2004) identify a substorm if the auroral bulge expands poleward of the oval over at least 20 minutes in local time [94]. Liou (2010) identify a substorm if the Polar UV imagers detect a sudden brightening of aurora followed by at least $\sim$10 minute growing aouroral intensity, but the identifications do not require poleward expansion

of the auroral oval to determine a substorm. Therefore, Liou's (2010) Polar UV substorm database includes weaker substorm onset events than Frey et al.'s IMAGE FUV database. Nevertheless, both detectors observed substorm onsets on average at $\sim 66^0$ latitude and ~ 23 MLT. The two substorm events are selected from the Frey et al. (2004) [94] and Liou (2010) [88] substorm databases with good SuperDARN scatter on the nightside.

A negative fluctuation of the magnetic H-component of a ground magnetometer is a sign that a substorm is beginning in the region observed [96]; [97]. As shown in Table 4.1, the observed onset time of a substorm can vary depending on the observing instrument. For example, the limited coverage of the Canadian Array for Realtime Investigations of Magnetic Activity (CARISMA) magnetometer chain did not allow observation of the onset of the substorm on February 05, 2000, that was observed by the Polar spacecraft due to their wide view ultraviolet imagers. Most of the CARISMA magnetometers are on a north-south meridian known as the 'Churchill Line' and hence the observations are restricted to certain magnetic local time (MLT). Figure 4.1 shows the fluctuation of the magnetic H-component (measured in nT) detected from 12 magnetometer stations during 04:00 to 08:00 UT on October 14, 2001. The event was discussed earlier by Bristow and Jensen (2007) [98]. CARISMA is part of the Canadian Space Agency's ground based geophysical observatory programme (GO) and operated by the University of Alberta. As shown in Figure 4.1, the Gillam (GILL) station observed a sharp negative bay at 06:18 UT in the midnight sector. Rabbit Lake (RABB) and Fort Churchill (FCHU) stations observed the negative fluctuations later $\sim$ 06:30 UT.

Table 4.1: Substorm onset events

Event date	Identification of substorm onset		Duration of the event to be discussed
	Magnetometer	UV Imager	
October 14, 2001	06:18 (Gill)	06:24 UT (IMAGE)	05:30–07:30 UT
February 05, 2000	Not available	18:41 UT (Polar)	17:30–19:30 UT

During the second substorm event, CARISMA ground magnetometers were on the day side and could not detect the drop of the magnetic H-component during the substorm onset on the night side.

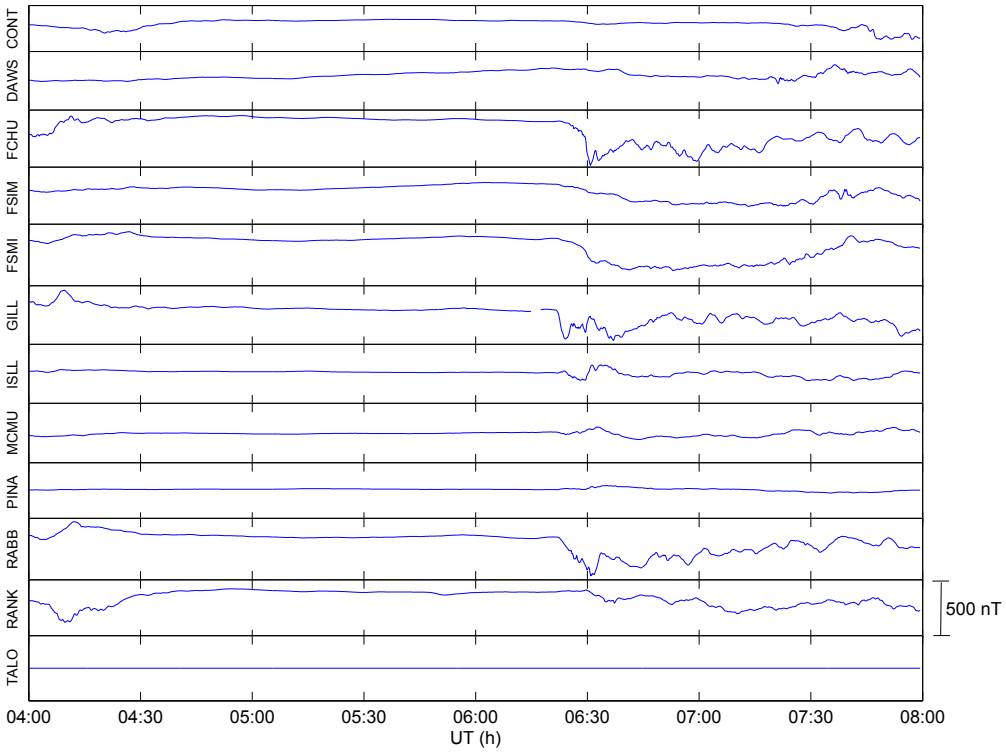

Figure 4.1: Substorm observations from 12 different stations on October 14, 2001. CARISMA magnetometers are shown on the y-axis.

4.2 Solar Wind and IMF Conditions

Solar wind conditions during the two substorm events were observed from ACE spacecraft as shown in Figures 4.2 and 4.3. Figure 4.2 shows the interplanetary magnetic field (IMF) between 04:30 and 06:30 UT on October 14, 2001, as detected from ACE spacecraft located some 221 R_e upstream from the Earth during the interval of interest. The average solar wind velocity was 446 km/s in the x direction in the solar magnetospheric (GSM) coordinate system. Hence, the average propagation delay from the ACE spacecraft to the magnetosphere has been estimated to be $\sim$ 53 minutes. The dynamic pressure is taken from OMNI and therefore is delayed to the magnetosphere while the ACE data are not time lagged. The IMF B_z component was southward for the whole interval. The IMF B_y component was slightly negative during the substorm onset, except at $\sim$ 04:45 UT for a few minutes when it displayed slight positive fluctuations (it reached a maximum of $\sim$ 2 nT). The dynamic pressure was steady for the entire event with an average value of $\sim$ 0.9 nT. Overall, The IMF y and z component was steady with a range of -5 to 2 nT.

IMF observations from ACE spacecraft are shown in Figure 4.3 during the second substorm event. The interval was chosen from 16:30 UT to 18:30 UT on February 05, 2000. The time delay of the event was 54 minutes. Hence the data from the OMNI database are time lagged while the ACE spacecraft data are not time delayed. During the event, the IMF B_z component was strongly negative, approximately -12 nT. IMF B_y was positive till 16:50 UT, with a value of around 5 nT. After 16:50, IMF B_y fluctuated from positive to negative and remained negative. The solar wind dynamic pressure varied from 4.98 nT to 11.95 nT during the interval. Fifteen minutes before the onset began, the pressure went down to 5 nPa. Overall, the solar wind dynamic pressure was higher than in the previous substorm event with stronger IMF components.

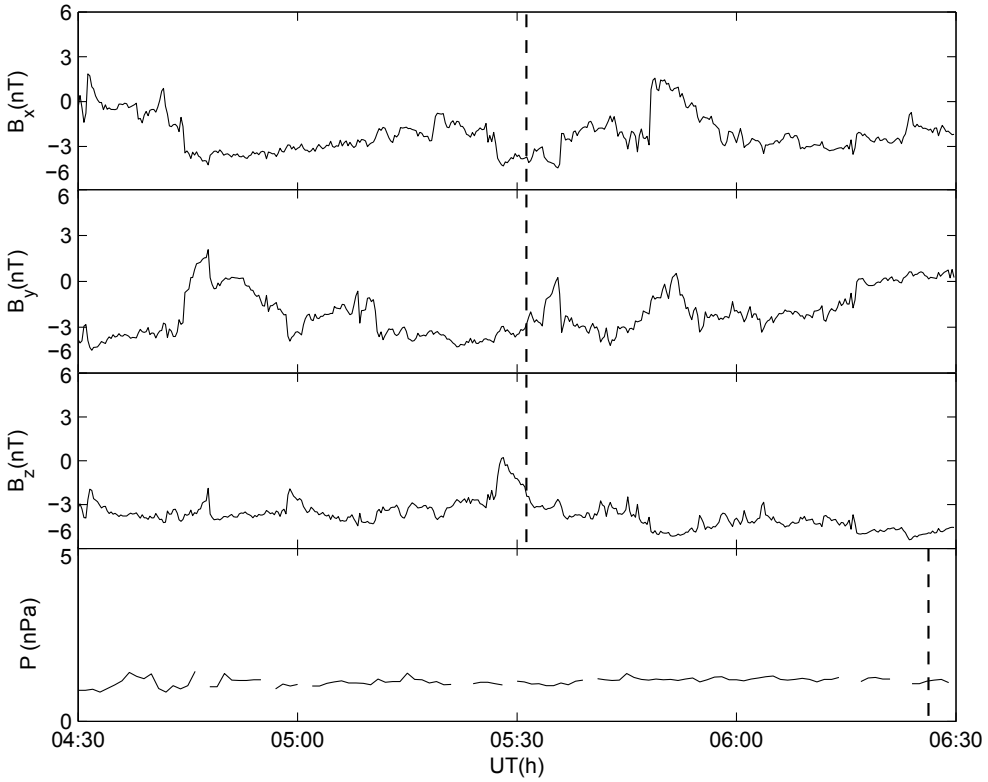

Figure 4.2: Interplanetary magnetic field (IMF) condition on October 14, 2001. The top three panels show the IMF measured by the ACE spacecraft with no time delay. The fourth panel represents the solar wind dynamic pressure with 53 minute time delay; data were acquired from the OMNI database and comprise measurements taken from the Geotail spacecraft. The vertical dash line corresponds the onset time during the interval while in the forth panel, onset time is located at 06:24 UT as the dynamic pressure is already delayed to the magnetosphere.

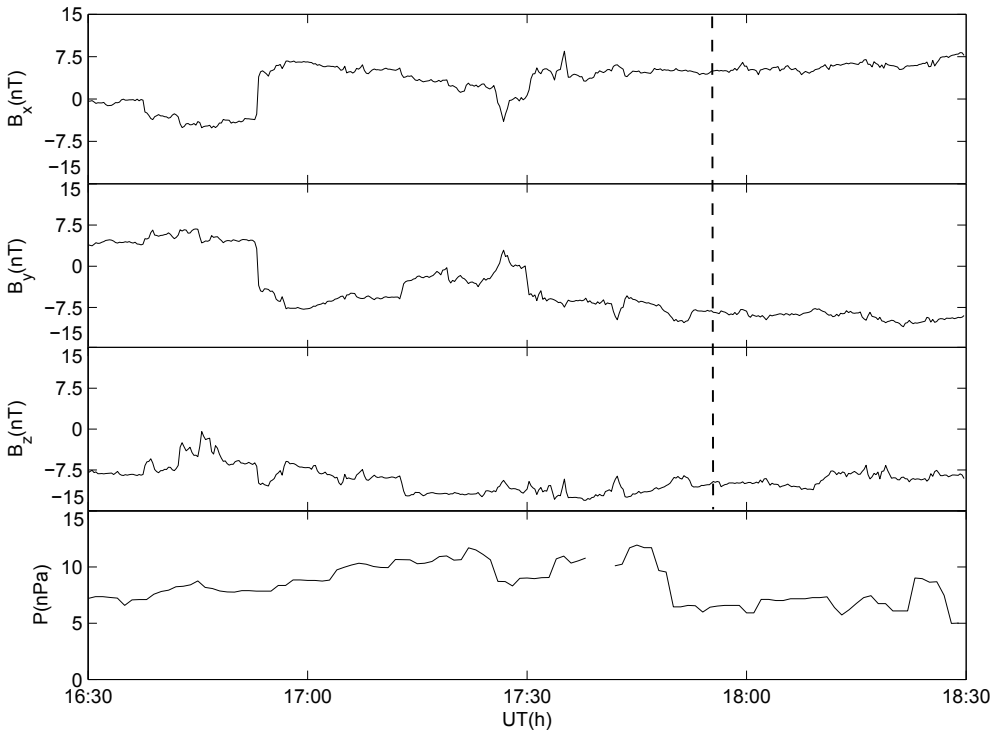

Figure 4.3: Interplanetary magnetic field (IMF) condition on February 05, 2000. The top three panels show the IMF measured by the ACE spacecraft with no time delay. The fourth panel represents the solar wind dynamic pressure with 54 minute time delay; data were acquired from the OMNI database and comprise measurements taken from the Geotail spacecraft. The vertical dash line corresponds the onset time during the interval while in the forth panel, onset time is located at 18:41 UT (not shown).

4.3 First Substorm Onset

4.3.1 Observations of the Auroral Emissions

During the first substorm interval on October 14, 2001, nine SuperDARN radars, namely, Kodiak, Prince George, Saskatoon, King Salmon, Pykkvibær, Hankasalami, Goose Bay, Kapuskasing, and Stokkseyri were available. Figure 4.4 shows the convection velocity map at 06:30-06:32 UT. During this event the SuperDARN ionospheric backscatter was good except in the local afternoon and dawn sectors.

The SuperDARN convection maps are derived at 2 minute intervals for the duration of the event. From these maps the directional derivatives of plasma flow speed are calculated and the OCB locations measured using the technique outlined in Chapter 2.

IMAGE FUV detectors observed the first (October 14, 2001) substorm onset at about 06:24 UT. During the first substorm event, the spectrographic imagers (SI-12 and SI-13) measured the proton precipitation and energetic electron precipitation, respectively while the wideband imaging camera (WIC) data was not available. The OCB location observed by IMAGE FUV detectors was obtained from the British Antarctic Survey website. The temporal resolution of IMAGE FUV detectors is about 2 minutes, similar to the SuperDARN temporal resolution.

Figures 4.5 and 4.6 depict SuperDARN radar observations and UV aurora measurements from the spectrographic imagers of the IMAGE spacecraft from 06:00 UT–07:00 UT in a magnetic local time and a magnetic latitude coordinate system. The figures are arranged horizontally into three triplets of panels,

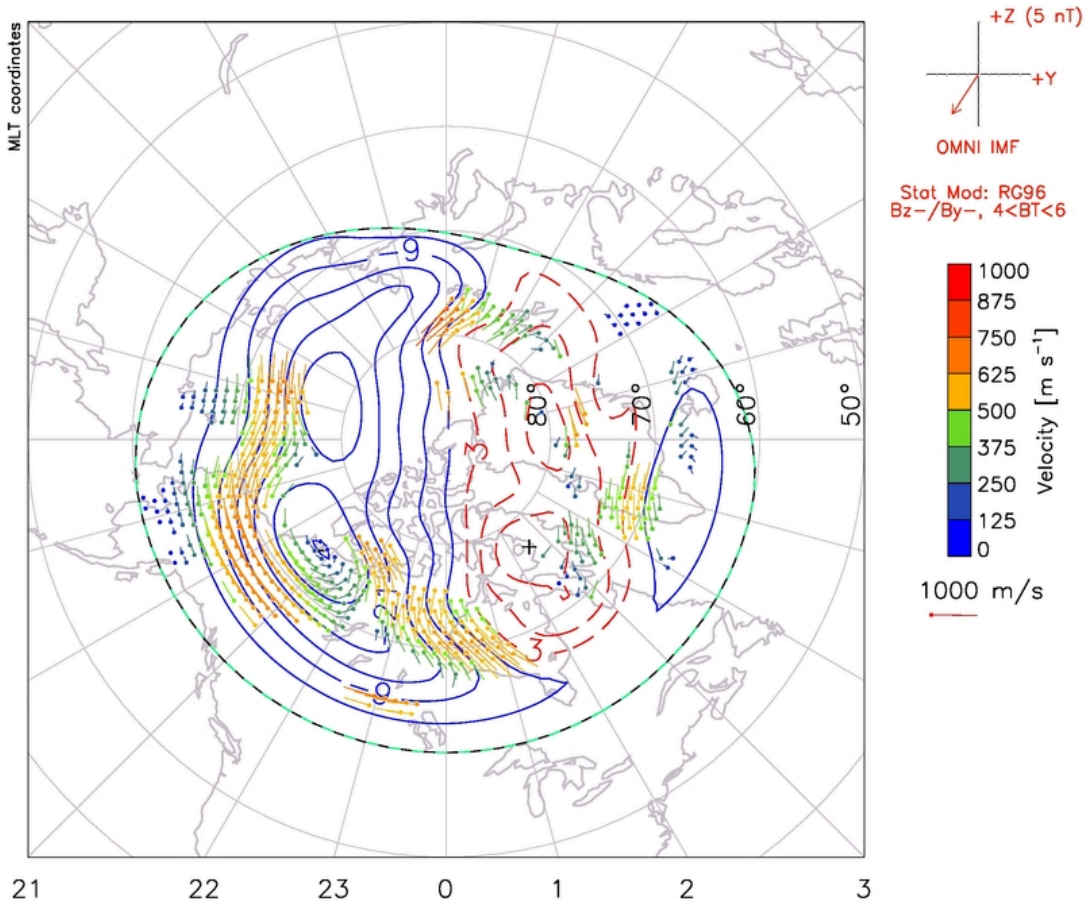

Figure 4.4: Global convection map of the nine SuperDARN radars used in the first substorm interval, October 14, 2001, at 06:30–06:32 UT. The order of fit is 8. Geomagnetic latitudes are shown with black circles from 50° to 80° latitude. Radial co-ordinates represent magnetic latitude differences starting from 50° and the radial lines represent MLT (magnetic local time) meridians, with noon at the top and midnight at the bottom. The dots at the beginning of the vectors indicate the vector locations, the lines show the vector direction, and the colors and length of the lines show the vector magnitude. The velocity scale is shown at the right side of the figure. Solid (dotted) contours are associated with negative (positive) values of electrostatic potential. IMF condition is at the top-right corner of the figure. [`superdarn.org`]

each separated by 10 minutes. Within each trio, the left column shows SI-12 intensity measurements, the middle column presents UV aurora in the 130–140 nm band from the SI-13 detector. OCB locations determined by the ultraviolet imagers are indicated by filled white dots. Contour plot of the directional derivatives of the convection flow speed as a function of magnetic latitude and local time are shown in the right column of Figures 4.5 and 4.6. As in Figures 2.3 and 3.2 in chapters 2 and 3, respectively, a rainbow color band is used to indicate the level of the directional derivative of plasma flow. Red indicates a large positive plasma flow directional derivatives whereas violet indicates a large negative flow directional derivative. Positive peaks in the directional derivative of flow are used as indicators of the SuperDARN OCB and are identified by the black plus signs. During the interval, an OCB could not be determined at 0.5 MLT due to a lack of data coverage in the vicinity of the maximum flow directional derivative along the 0.5 MLT meridian. The OCBs measured in the dawn and dusk sectors are compared and discussed in section 4.3.2.

The upper panel on Figure 4.5 shows images of ultraviolet emissions from spectrographic detectors (on the left) recorded at 06:01:49 UT, nearly simultaneous with the convection flow directional derivative observations at 06:00 UT measured by the SuperDARN (on the right). As shown in Figure 4.5 and 4.6, auroral intensity increases at substorm onset with the brightest UV emission recorded at $\sim$ 06:30 UT in the midnight sector (upper left panel in Figure 4.6) with a peak intensity of 1500 Rayleigh. Due to the substorm auroral bulge, the location of the OCB in the post-midnight sector moves poleward from $\sim 70^{\circ}$ to $\sim 74^{\circ}$ magnetic latitude. Meanwhile, in the dusk region, thinner and further equatorward auroral emissions were observed from the SI-13 channel from $\sim$ 06:30 UT.

The simultaneous observations from SuperDARN radars presented in Figure 4.5

and 4.6 indicate a convection flow directional derivative distribution. The peak intensity of the convection flow directional derivative in the dusk region was at higher latitude ($\sim 80°$) at the beginning of the interval (at 06:00 and 06:10 UT) and moved equatorward ($\sim 70°$) from 06:20 UT. Primary and secondary peaks in the directional derivative of flow are observed in the dusk sector at 06:10 and 06:20 UT (middle and lower panel on figure 4.5). The occurrence of multiple peaks in the directional derivative of flow at two different latitude will be discussed in chapter 5. The OCB could not be measured at 0.5 MLT from 06:20–06:40 UT, as the location of the peak of plasma flow and the location of the measured plasma vectors were different.

4.3.2 Comparison of OCB Locations Derived from the SuperDARN and Two Spectrographic Imagers

To further demonstrate the location of the OCB and compare the findings from the two techniques during the October 14, 2001, substorm, Figures 4.7 and 4.8 present the temporal evolution of the OCB in dawn and dusk sectors, respectively, determined from the directional derivative of SuperDARN flow calculations and the IMAGE FUV instrument. Each figure is divided into five panels, each of which shows the temporal evolution of the OCB at a particular MLT. The temporal resolution of the OCB is 2 minutes. Boundaries detected by SI-13 ($\ldots*\ldots$) and SI-12 (—+—) cameras were collocated during the interval, except during the substorm onset (where a maximum of 5° disagreement was recorded at 4.5 and 6.5 MLT). In the pre-midnight to dawn sector (22.5 - 4.5 MLT) in figure 4.6 and 4.7, it is evident that the IMAGE FUV boundaries moved poleward after the onset, except at 6.5 MLT.

Prior to 06:00 UT either SuperDARN or UV imagers could not measure boundaries continuously to make any comparison in the dawn sector. SuperDARN

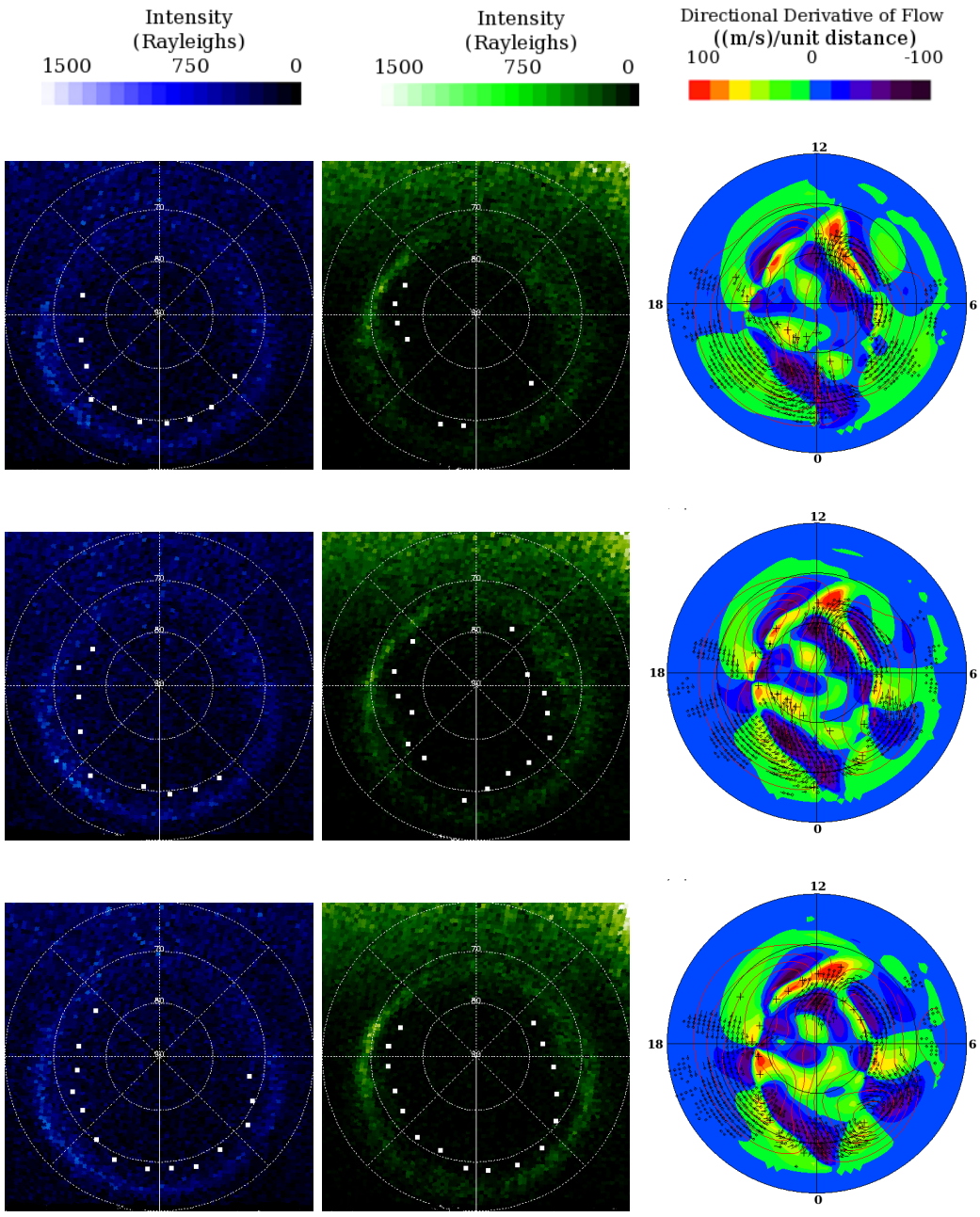

Figure 4.5: Images of the UV aurora taken at 06:00, 06:10, 06:20 UT (from top to bottom) on October 14, 2001 by the IMAGE SI-12 detector (left column) and SI-13 detector (middle column). Directional derivatives of SuperDARN Convection flow at the closest times to the auroral images are presented in the right column. Solid circles represent 60°, 70°, and 80° MLAT, and radial lines represent MLT meridians at midnight, morning, noon, and evening, with noon at the top and midnight at the bottom. Auroral intensity and flow directional derivatives are color coded according to the color scale located at the top of the panel.

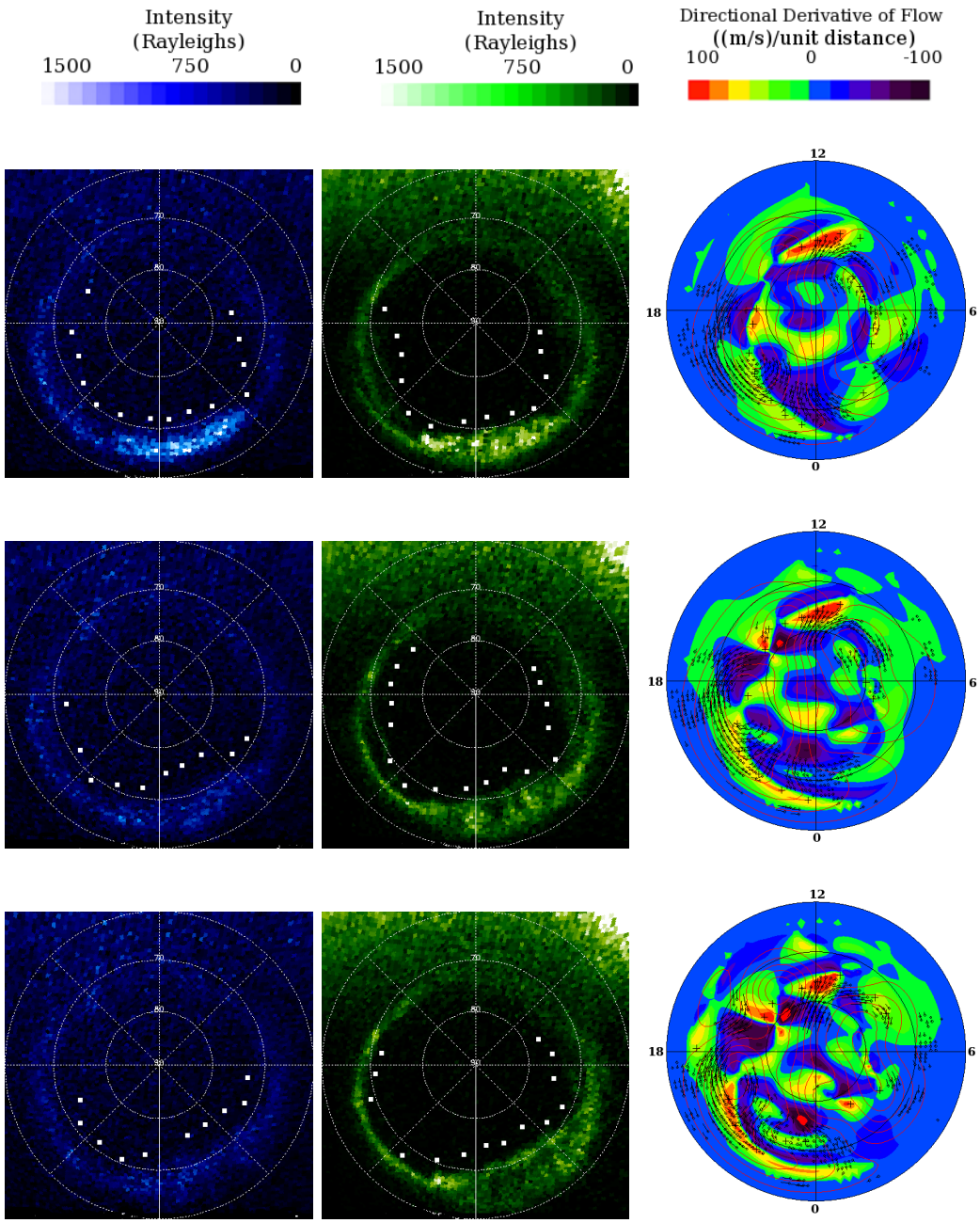

Figure 4.6: Images of the UV aurora taken at 06:30, 06:40, 06:50 UT (from top to bottom) on October 14, 2001 by the IMAGE SI-12 detector (left column) and SI-13 detector (middle column). Directional derivatives of SuperDARN Convection flow at the closest times to the auroral images are presented in the right column. Solid circles represent 60°, 70°, and 80° MLAT, and radial lines represent MLT meridians at midnight, morning, noon, and evening, with noon at the top and midnight at the bottom. Auroral intensity and flow directional derivatives are color coded according to the color scale located at the top of the panel. Note that the red color inside the black contours is an issue with the contour plot routine in IDL.

could not measure the boundaries continuously during the interval. At 1.5 and 2.5 MLT, SuperDARN could not measure boundaries during 06:20 to 06:50 UT, and 06:14 to 07:08 UT, respectively. SuperDARN could measure few boundaries at 3.5 MLT during the interval. On or after the onset, almost no SuperDARN boundaries were identified from 4.5 to 6.5 MLT. The OCB determined from the directional derivative of SuperDARN convection flow calculations (—o—) agrees well with spectrographic measurements at 1.5 and 6.5 MLT. At 2.5 MLT, SuperDARN boundaries agree with spectrographic imagers after the onset interval while the disagreement with IMAGE FUV measurements was on average $\sim 4^{\circ}$ poleward during the first hour of the interval. SuperDARN boundaries were located at higher latitude than IMAGE FUV boundaries at 3.5 and 4.5 MLT.

Temporal evolution of the OCB are compared between SuperDARN and spectrographic detectors between the dusk and pre-midight sector in Figure 4.8. Between 19.5 and 21.5 MLT, OCBs were collocated before and after the substorm onset and both moved equatorward after the onset. At midnight (at 22.5 and 23.5 MLT), IMAGE FUV boundaries moved $\sim 4^{\circ}$ poleward and then remain fairly steady while the SuperDARN boundaries remain many degrees equatorward of the FUV OCB during substorm expansion until 06:46 UT when they move 6° poleward to become collocated with the IMAGE FUV boundary. The event will be discussed in Chapter 5 in more detail. The SuperDARN OCB was 1–2° more poleward than the OCB measured from the spectrographic detectors prior to 06:00 UT at 21.5 and 22.5 MLT. Overall, the temporal evolution of the OCB measured with SuperDARN data agrees well with data from the spectrographic detectors.

Data from the IMAGE cameras disagree regarding the position of the OCB on the night side of the Earth at 1.5 and 2.5 MLT, only from 07:00–07:30

UT (Figure 4.7), possibly because the SI-12 camera detects high energy proton precipitation while the SI-13 camera detects electron precipitation. OCB locations derived from SuperDARN data accord with locations derived from SI-13 detectors during the 07:00–07:30 interval. Overall, Figures 4.7 and 4.8 indicate intervals of good agreement between OCB locations derived from the SuperDARN flow directional derivative technique and IMAGE FUV detectors, particularly with the SI-13 camera which is a reliable proxy for OCB measurement [49].

OCBs determined in the post-midnight – dawn sector indicate that the boundaries moved poleward in the post-midnight – dawn sector (1.5 MLT–4.5 MLT) while boundaries in the dusk sector from 19.5 to 21.5 MLT moved equatorward before and after substorm onset and remained constant $\sim$ 10 minutes after the onset. Nevertheless, the SuperDARN OCB followed the trend line of the OCB measured by the spectrographic imagers.

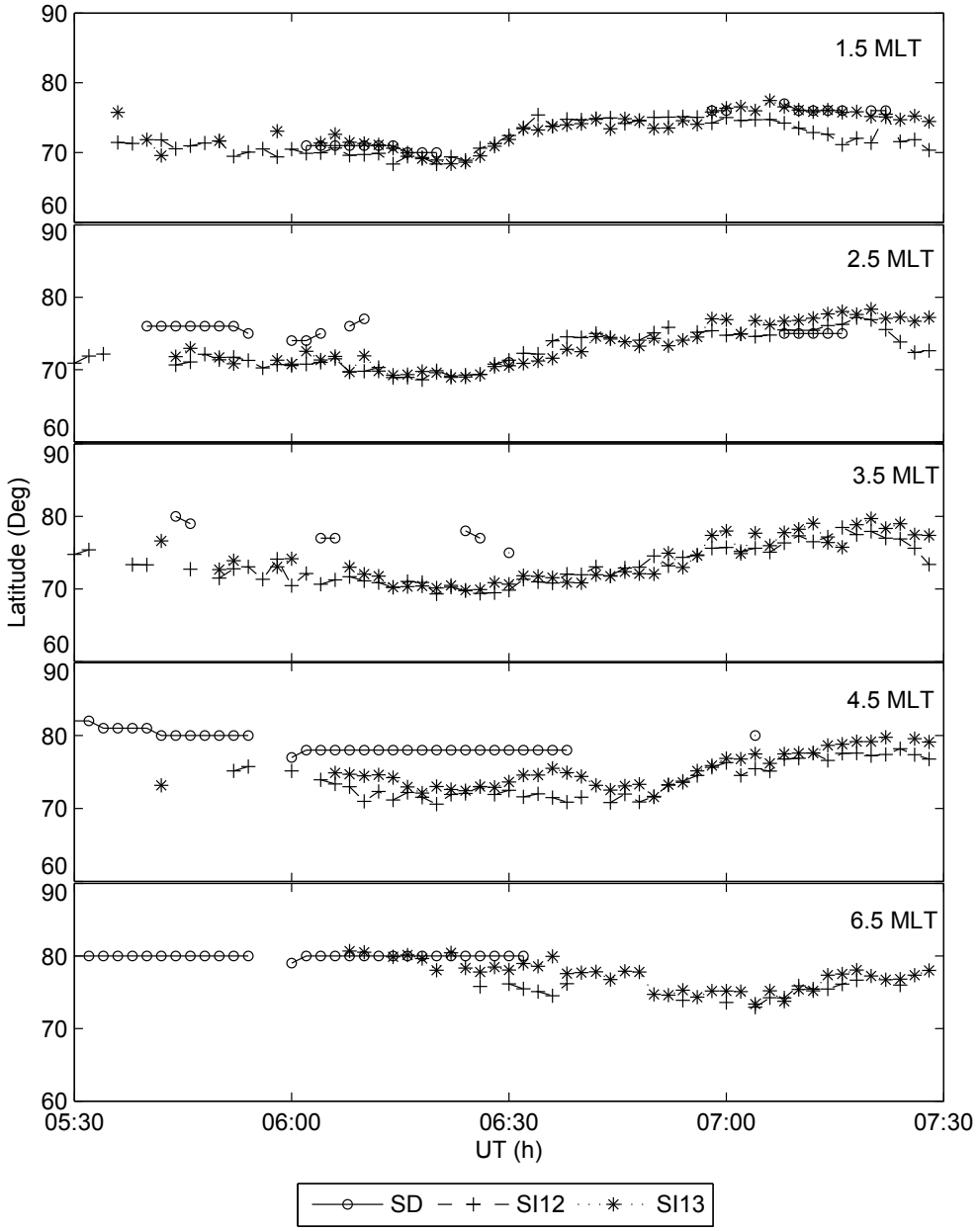

Figure 4.7: Temporal evolution of the OCB in the dawn sector on October 14, 2001. (—+—), (. . . *. . .), and (—o—) represent IMAGE camera SI-12, IMAGE camera SI-13, and SuperDARN flow directional derivative technique, respectively.

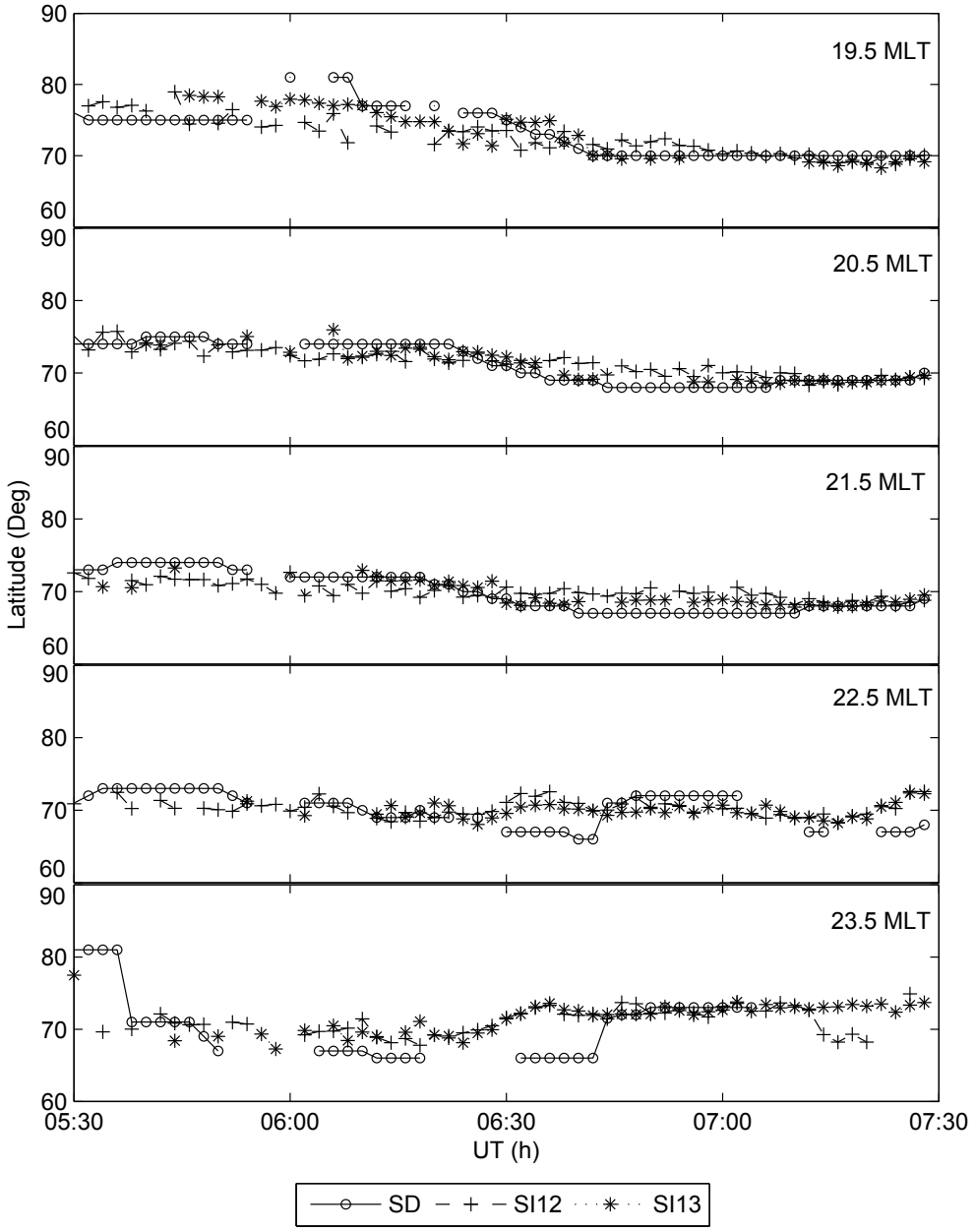

Figure 4.8: Temporal evolution of OCB at dusk – pre-midnight sector on October 14, 2001. (—+—), (. . . *. . .), and (—o—) represent IMAGE camera SI-12, IMAGE camera SI-13, and SuperDARN flow directional derivative technique, respectively.

4.4 Second Substorm Onset

4.4.1 Observations of Auroral Emissions

Figure 4.9 shows the convection potential map derived from the seven SuperDARN radars available during the substorm interval on February 05, 2000, namely, Kodiak, Saskatoon, pykkvibær, Hankasalami, Goose Bay, Kapuskasing, Stokkseyri. During the interval, plasma flow vectors were detected by the SuperDARN in the dusk sector. At the beginning of the interval, the flow vectors were measured on the day side of the Earth from 6.5 MLT to $\sim$ 20.5 MLT. As time went by, flow vectors and the corresponding OCB could be estimated only in the dusk sector ($\sim$ 12.5 to $\sim$ 23.5 MLT). The discussion is limited to the dusk sector because this sector was monitored continuously during the interval. The February 05, 2000 substorm was identified by Polar UV imagers at $\sim$ 18:41 UT. LBH (Lyman-Birge-Hopfield) long filter was used to determine the OCB during the interval. These LBH images were recorded every $\sim$ 37 s. The energy flux of precipitating electrons, measured by the LBH long filters were calibrated in photon flux units (photon/cm^{2}s). A full width half maximum (FWHM) technique, as discussed in Chapter 2, was used to determine the OCB from Polar UV emissions. The Polar ultraviolet imager (UVI) observations with LBH long filters are a reliable proxy for detecting the OCB in the dusk sector [89].

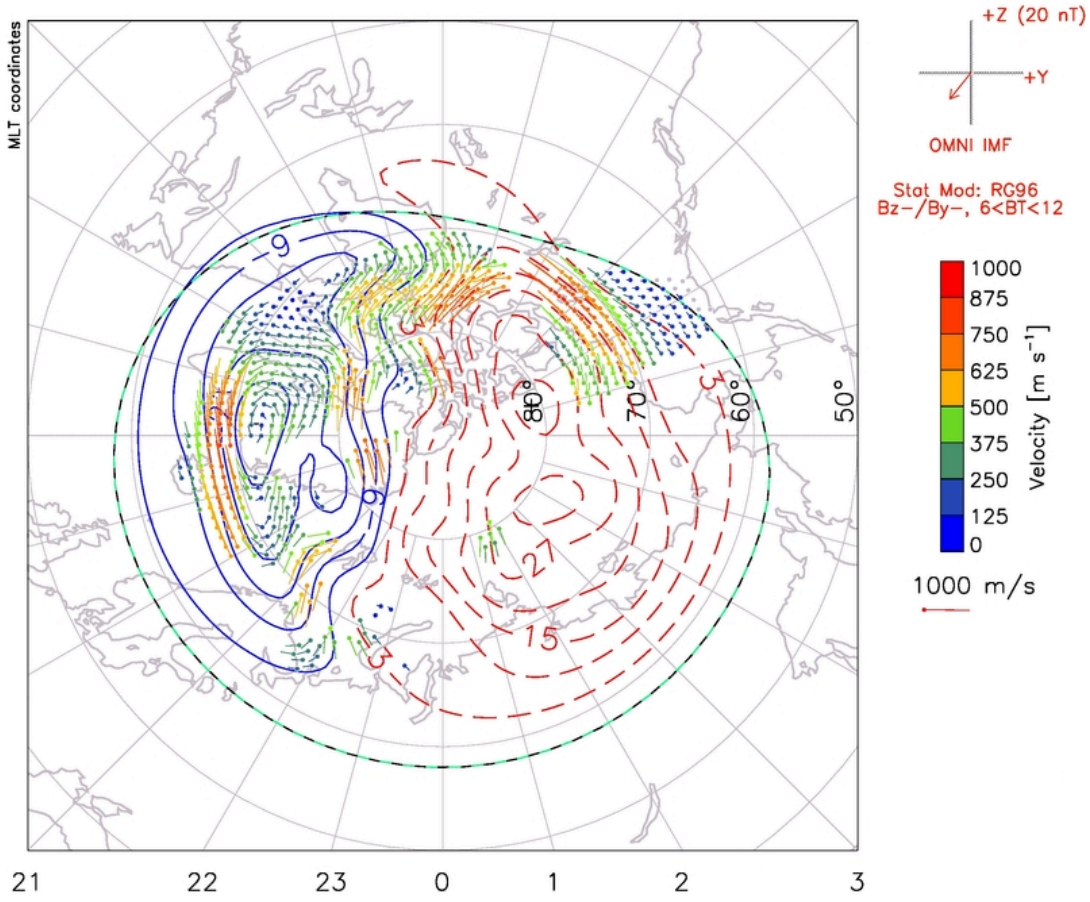

Figure 4.9: Global convection map of SuperDARN radars used to measure the substorm onset on February 05, 2000, from 19:00–19:02 UT. The order of fit is 8. Radial co-ordinates represent magnetic latitude differences starting from 50° and the radial lines represent MLT (magnetic local time) meridians, with noon at the top and midnight at the bottom. The dots at the beginning of the vectors indicate the vector locations, the lines show the vector direction, and the colors and length of the lines show the vector magnitude. The velocity scale is shown at the right side of the figure. Solid (dotted) contours are associated with negative (positive) values of electrostatic potential. IMF condition is at the top-right corner of the figure. [`superdarn.org`]

Figures 4.10 and 4.11 show the SuperDARN observations (right column) and the auroral emission measured by Polar UV imagers with LBH long filters (left column). Polar measurements were taken on February 05, 2000, from 18:30–19:30 UT and the SuperDARN observations were made at the closest times to the auroral images. The figures are formatted at the same magnetic local time and in the same magnetic latitude coordinate system. The contours of magnetic latitudes from 60° to 90° with a 10° increment are plotted with midnight at the bottom and noon at the top. OCBs determined from the measurements are represented by a 'plus sign.'

According to the Polar UV images, the first auroral brightening took place at $\sim$ 18:41 UT around 23.5 MLT. This brightening was followed immediately by an expansion of the auroral bulge in local time between 20 and 3 MLT. A rapid increase in particle precipitation spread in almost all directions. The auroral oval was thinner and more distinct in the dusk sector, between 15 and 21 MLT. By 19:00 UT the polar cap had significantly contracted in size, with the aurora expanded to high latitude in the post-midnight region. Although the peak intensity of the particle precipitation was observed also in the pre-midnight region, the substorm auroral emissions are restricted to dawn sector. The poleward edge of the auroral oval stayed below 70° between 21 and 23 MLT during the interval.

Some studies indicate that a distinction between the OCB and auroral oval arcs is not trustworthy when detected by ultraviolet imagers [99]; [100], particularly during the substorm onset [101]. Figure 4.12 shows the OCB locations observed at 19:20 UT on February 05, 2000 calculated from the single Gaussian peak of the auroral oval.

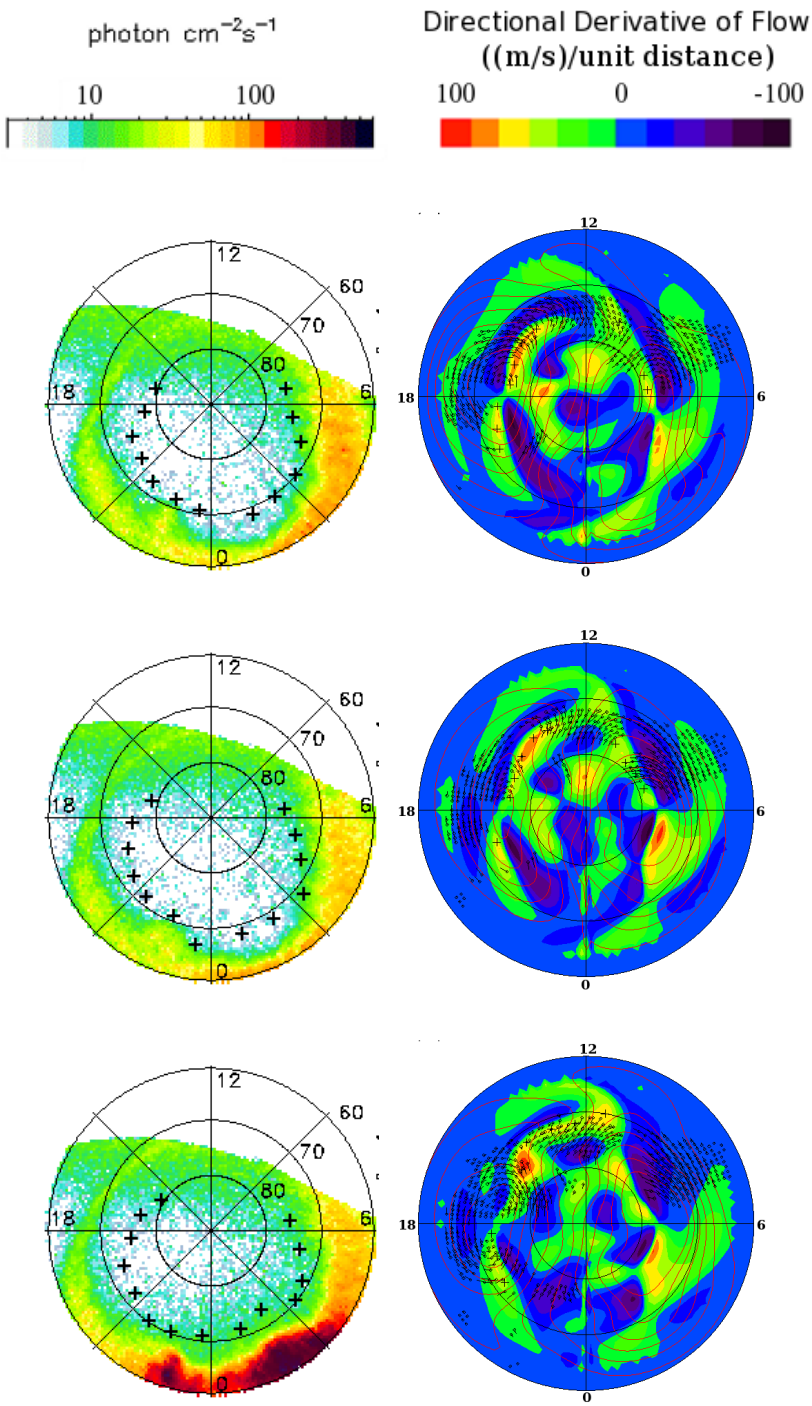

Figure 4.10: Left: Images of the UV aurora taken at 18:30, 18:40, 18:50 UT (from top to bottom) on February 05, 2000 by by LBH long filters on the Polar UVI satellite. Right: Directional derivative of SuperDARN flow at the closest times to the auroral images. Solid circles represent 60°, 70°, and 80° MLAT, and radial lines represent MLT meridians at midnight, morning, noon, and evening, with noon at the top and midnight at the bottom. Auroral intensity and flow directional derivatives are color coded according to the color scale located at the top of the panel.

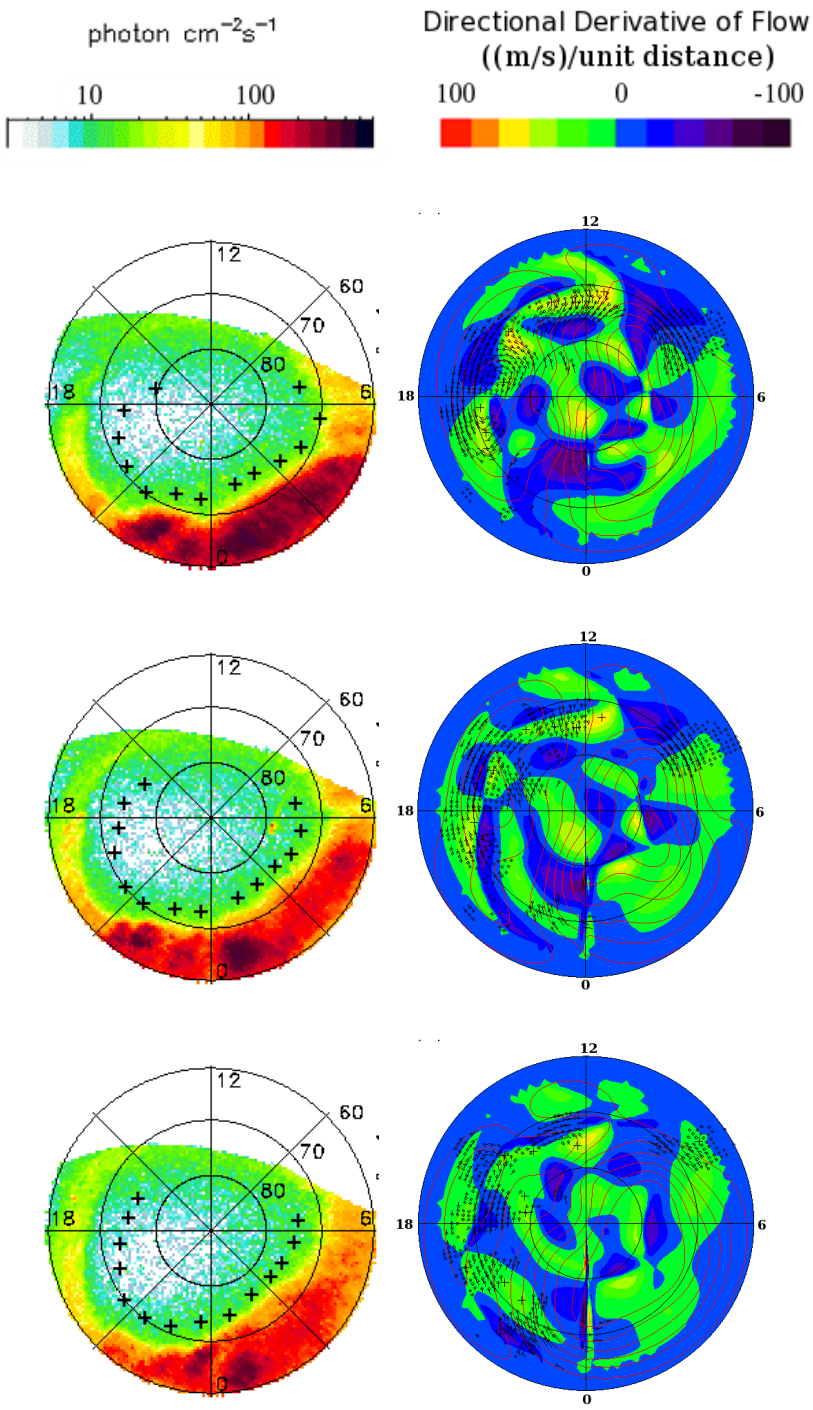

Figure 4.11: Left: Images of the UV aurora taken at 19:00, 19:10, 19:20 UT (from top to bottom) on February 05, 2000 by by LBH long filters on the Polar UVI satellite. Right: Directional derivative of SuperDARN flow at the closest times to the auroral images. Solid circles represent 60°, 70°, and 80° MLAT, and radial lines represent MLT meridians at midnight, morning, noon, and evening, with noon at the top and midnight at the bottom. Auroral intensity and flow directional derivatives are color coded according to the color scale located at the top of the panel.

4.4.2 Comparison of OCB Locations Derived from the SuperDARN and the Polar UV Imager

Figure 4.13 shows a time series of dusk sector OCBs measured during the substorm event on February 05, 2000, with the directional derivative of SuperDARN flow technique (o) and estimated with LBH long filters on the Polar spacecraft UV imager (+). The five panels in the figure represent times ranging from 16.5 MLT to 20.5 MLT, with each panel representing a latitude of 60°–90°. The velocity vectors and the directional derivatives of plasma flow speed measured by the SuperDARN were absent at the midnight sector, therefore the OCB was compared between afternoon and pre-midnight, 17:30–19:30 UT. Each panel shows the temporal evolution of the OCB with 2 minute temporal resolution of SuperDARN data and 37 second temporal resolution of Polar spacecraft LBH long filter data.

The OCB locations from both techniques were at a higher latitude initially in the dusk sector, moved equatorward during the substorm onset, and then remained steady. At increasing magnetic local times, OCB locations are observed at considerably lower latitudes. For example, the OCB location was initially $\sim 84°$ and moved to $\sim 78°$ at 16.5 MLT whereas the OCB location moved equatorward from $\sim 79°$ to $\sim 71°$at 20.5 MLT. It is interesting to see that LBH long filters of Polar UV imager and the the directional derivatives of SuperDARN flow measurement did not find any sudden change in OCB location at substorm onset. However both measurements indicated that the OCB moved to a lower latitude at substorm onset at $\sim$ 18:41 UT.

Boundaries detected by Polar UVI and SuperDARN are in disagreement with a high of 4° recorded at 16.5 MLT. The largest discrepancy occurred before the substorm onset at 16.5 MLT. OCB detected from SuperDARN was $\sim 3°$

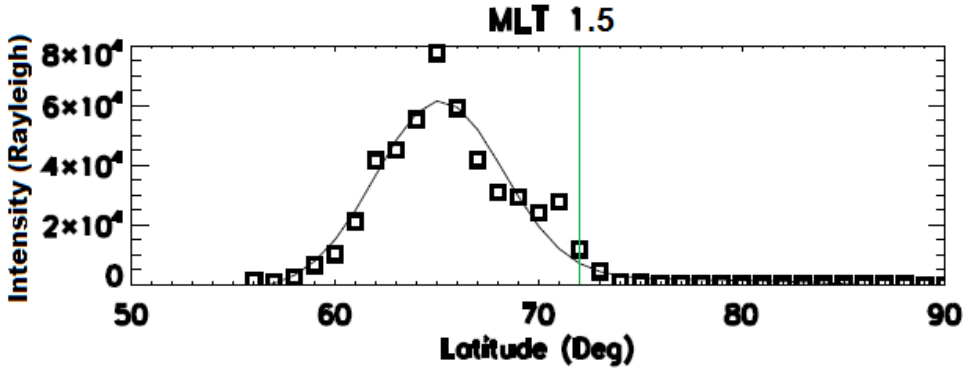

(a)

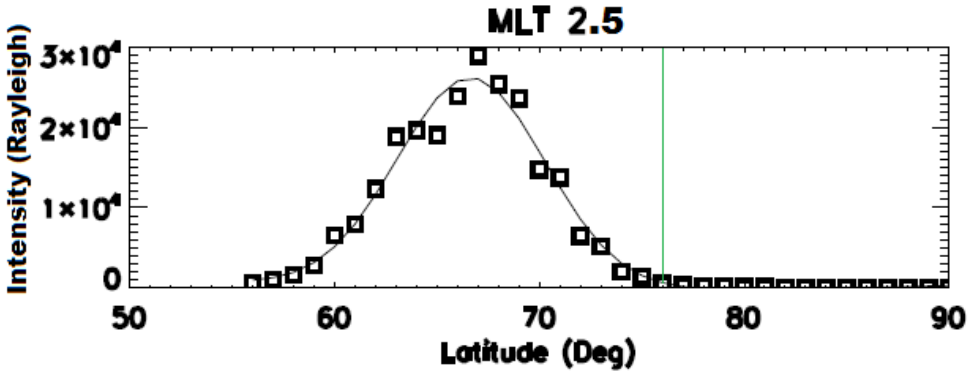

(b)

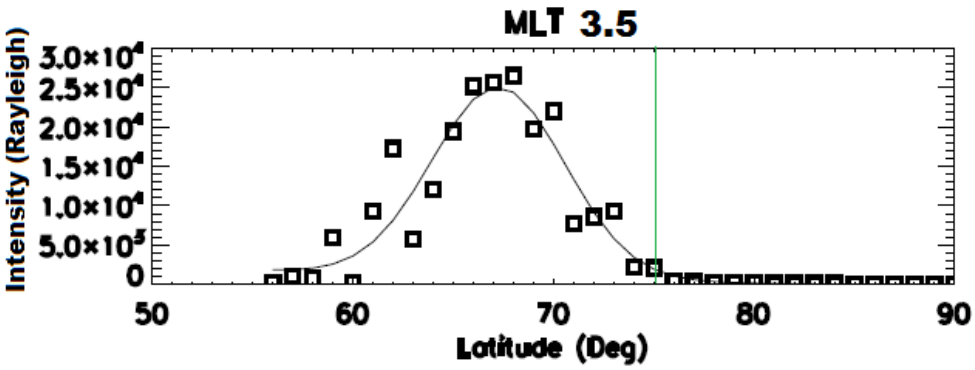

(c)

Figure 4.12: Three latitudinal profiles with OCB locations at 19:20 UT on February 05, 2000. From top to bottom: The location of OCBs are at 72°, 76°, and 75° at 1.5, 2.5, and 3.5 MLT respectively (Green solid lines in all panels).The box represents intensities averaged into a 1-hour MLT sector at different latitudes. The curve represents single Gaussian fit with quadratic background.

equatorward than the ultraviolet measurement. At 19.5 and 20.5 MLT, the SuperDARN OCBs are in agreement with the UVI boundaries. During the substorm onset, the temporal evolution of SuperDARN boundaries followed the trend line of Polar UVI boundaries. During the substorm, the maximum disagreement in the dusk sector was $\sim 2.5^{\circ}$ at 17.5 MLT.

The low order of disagreement between OCB location and the similar trend line of the OCB boundaries between SuperDARN and Polar results indicate that the SuperDARN OCB might be a useful proxy at 19.5-20.5 MLT during a substorm event.

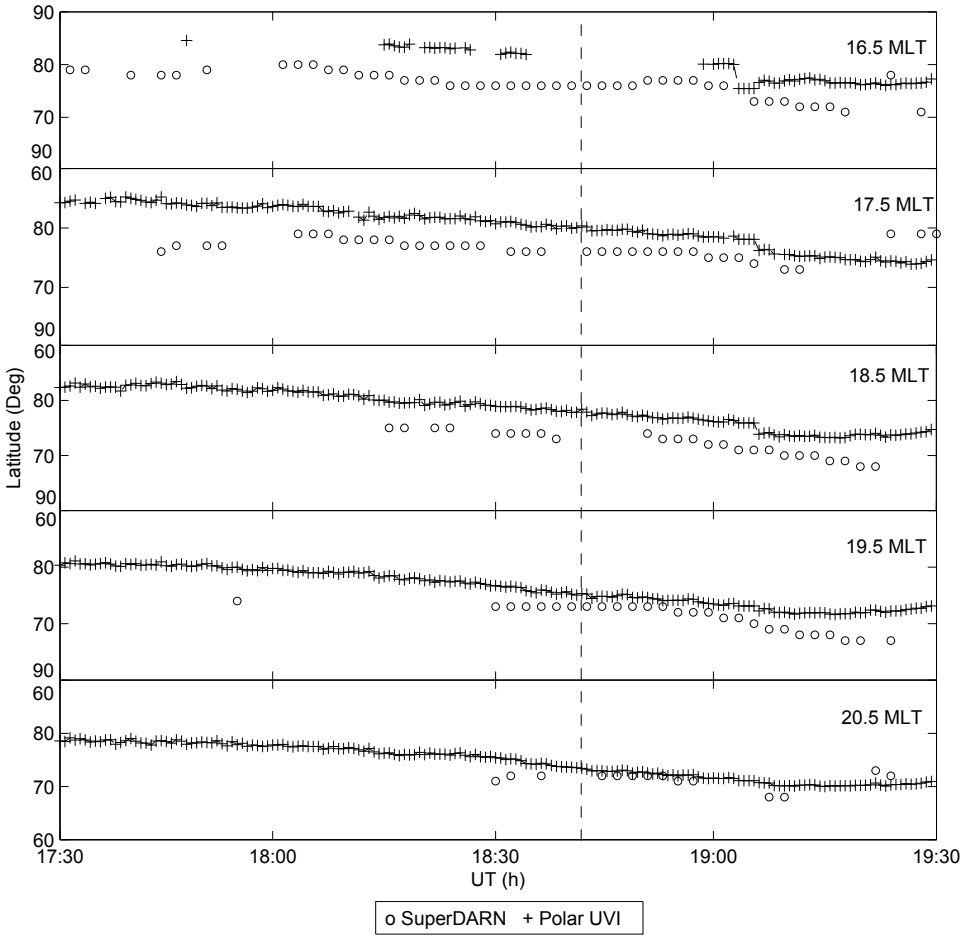

Figure 4.13: Temporal evolution of the OCB in the dusk sector on February 05, 2000. OCB locations were detected by Polar UVI (+) and SuperDARN flow directional derivative (o) techniques. The vertical dash line corresponds the onset time at 18:41 during the interval.

4.5 Conclusions

Ground and space-based OCB observations in the ionosphere during two substorm intervals in which interplanetary magnetic field conditions were different have been presented in this chapter. It was observed that OCB locations determined by the directional derivatives of SuperDARN flow agree with those measured with IMAGE spacecraft spectrographic FUV imagers in the dusk sectors during the substorm interval. Boundaries measured from SuperDARN and LBH long filters on the Polar spacecraft UV imager were in agreement at the 19.5 and 20.5 MLT in the dusk sector during the interval. Data from the two substorm onsets indicated, in general, that when the onset begins, the OCB location moves equatorward in the dusk sector (16.5 MLT–21.5 MLT) and poleward around midnight (between 22.5–23.5 and 1.5–3.5 MLT). It was also evident that the onset time was different for different instruments, though this did not affect the temporal evolution of the OCB observed during the two substorm events.

Some studies indicate that a distinction between the OCB and auroral oval arcs is not trustworthy when detected by ultraviolet imagers [99]; [102], particularly in the presence of a dynamic solar wind [100]. Therefore, OCB locations measured by ultraviolet detectors during a substorm onset, particularly under dynamic IMF conditions, should be viewed with caution.

Chapter 5

Estimating the OCB Location with Multiple Peaks in the Directional Derivative of Flow

Open-closed field line boundaries (OCBs) determined from SuperDARN flow directional derivatives were tested in Chapter 3 and Chapter 4. In the previous chapters, the OCB was determined from the maximum plasma convection flow directional derivatives under various solar wind conditions. The maximum positive value of the flow directional derivatives along any MLT meridian was identified as an OCB. Apart from the maximum positive flow directional derivative along any MLT meridian, a secondary peak is sometimes observed. The occurrence of a secondary peak is the topic of this chapter. Generally, the maximum peak is considered to be an OCB unless there are no data in the vicinity. In this chapter, secondary peaks that appeared during specific events are discussed and their relevance to OCB detection is compared with that of the primary peak and untraviolet detectors.

A secondary peak was most commonly observed in the midnight region. If the convection cells are asymmetric, then the primary and secondary peak of the

plasma flow at different latitudes along the MLT meridians can be observed in the midnight sector. The asymmetry of the dusk and dawn cells occurs primarily at pre-midnight and post-midnight along the MLT depending on the sign of IMF B_y.

The relation between large scale ionospheric convection and IMF conditions has been understood for a number of years [103]; [104]. If IMF B_y and B_z are negative, the shapes of the dusk and dawn cell are crescent and rounded respectively. Under this circumstance, multiple peaks in the flow directional derivatives may occur in the pre-midnight sector. Multiple peaks in the directional derivatives also occur during the positive IMF B_y case where the multiple peaks can occur in the post-midnight sector.

The OCB can also be detected with ultraviolet detectors such as those on the Polar ultraviolet imager (UVI) or the Image far ultraviolet detector (FUV), depending on the availability during the period. Individual time points are discussed from three different events during which multiple peaks in the directional derivative of flow occur. Section 5.1 will deal entirely with the first event. The surrounding intervals and the solar wind condition of the first event are discussed in section 5.1.1 and 5.1.2 respectively. Observations of the auroral emission at the selected time points using the Polar UVI detectors are discussed in section 5.1.3. The surrounding intervals of the second and third events were discussed in Chapter 3 and 4 respectively. Therefore the solar wind condition and the observation of auroral emission during these intervals are not presented here. The occurrences of multiple peaks in the directional derivative of flow are discussed in section 5.2. Four example time points from the first event are at 00:22, 00:40, 01:20, and 01:50 UT on April 20, 1999. In the second event the multiple peaks in the directional derivative of flow occurred at 08:46 UT on November 04, 2001. Two time points, 06:10 and 07:00 UT on October 14,

2001 are discussed in the third event. Comparison is presented between the two measurements, peaks in the directional derivative of SuperDARN convection flow and ultraviolet measurement in section 5.3. A summary and conclusions are presented in section 5.4.

5.1 Selection of the first Event Exhibiting Multiple Peaks in the Directional Derivative of Flow

5.1.1 Selection of the First Event Interval

On April 20, 1999, a substorm onset was detected at $\sim$ 01:30 UT with ultraviolet imaging from a Polar UVI spacecraft. The substorm event was reported in Liou (2010) [88], in which a number of substorm onsets detected from Polar spacecraft were discussed. The two-hour-long Polar UVI and SuperDARN data sets were examined. The duration of the interval to find the multiple peaks in the directional derivative of flow to be discussed in this chapter is between 00:00 UT and 02:00 UT on April 20, 1999.

All of the UV images from the Polar spacecraft were taken with LBH (Lyman-Birge-Hopeld) short (LBHS) and long (LBHL) band filters in wavelength ranges from 130–140 nm and 160–180 nm, respectively. Each image taken with LBHS and LBHL filters was integrated for over 19 seconds, and the time between successive images was three minutes.

The discussion is limited to the night sector because the flow vectors were measured in the pre-midnight and post-midnight region. The auroral activity

on the Earth's night side measured with ultraviolet imagers is compared with the primary and secondary peaks in the directional derivative of plasma flow in section 5.2.

5.1.2 Solar Wind and IMF Conditions During the First Event Interval

Fig 5.1 shows interplanetary magnetic field (IMF) observations from the Advance Composite Explorer (ACE) spacecraft during the interval of 23:00 UT on April 19, 1999, to 01:00 UT on April 20, 1999. The top three panels of Figure 5.1 present the magnetic field conditions of the solar wind in three directions during the interval with 16 second temporal resolution. The fourth panel shows the 1 min time resolution of the dynamic pressure of the solar wind. The ACE spacecraft was located 273 R_e upstream of the Earth and measured an average solar wind velocity in the x direction of 456.5 km/s in the geocentric solar magnetospheric (GSM) coordinate system. Hence, the average propagation delay from ACE has been estimated to be around 53 minutes, however, the ACE spacecraft IMF data are not time lagged in Figure 5.1. It is noted that, due to the time delay, the IMF observation from the ACE at 00:37 UT is equivalent to a substorm onset at $\sim$ 01:30 UT measured by the Polar UVI spacecraft. After 23:20 UT the IMF B_z was mostly southward with some northward fluctuations. The IMF B_z component was negative during the onset. Approximately 8 minutes after the substorm onset (around 00:45 UT) the IMF B_z component turned northward with some southward fluctuations for a short interval. During most of the period, the IMF B_y component was positive. The dynamic pressure was steady between 2 and 4 nPa. In summary, the IMF condition during the interval, including during the substorm onset period, was mostly southward with a steady dynamic pressure.

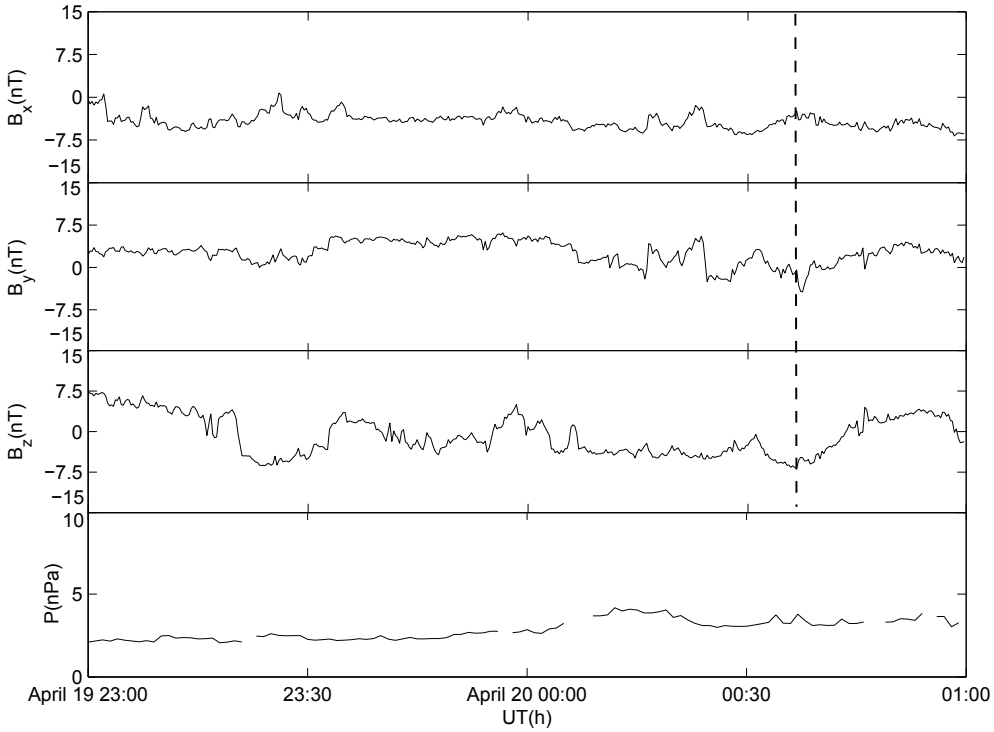

Figure 5.1: Interplanetary magnetic field (IMF) condition during the substorm interval on April 20, 1999. The top three panels show the IMF measured by the ACE spacecraft with no time delay. The fourth panel represents the solar wind dynamic pressure with 53 minute time delay; data were acquired from the OMNI database and comprise measurements taken from the Geotail spacecraft. The verticle dash line indicates the substorm onset time at 00:37 UT during the interval while in the forth panel, onset time is located at 01:30 UT (not shown) as the dynamic pressure is already delayed to the magnetosphere.

5.1.3 Auroral Observations during the First Event

During the interval, six SuperDARN radars were engaged in measuring the plasma velocity in the northern oval. Figure 5.2 shows the convection velocity map at 01:30- 01:32 UT. As in previous chapters, the temporal resolution of SuperDARN data is two minutes during the interval. Throughout the interval, ionospheric plasma flow measurements from the coherent scatter radars were available in the night sector.

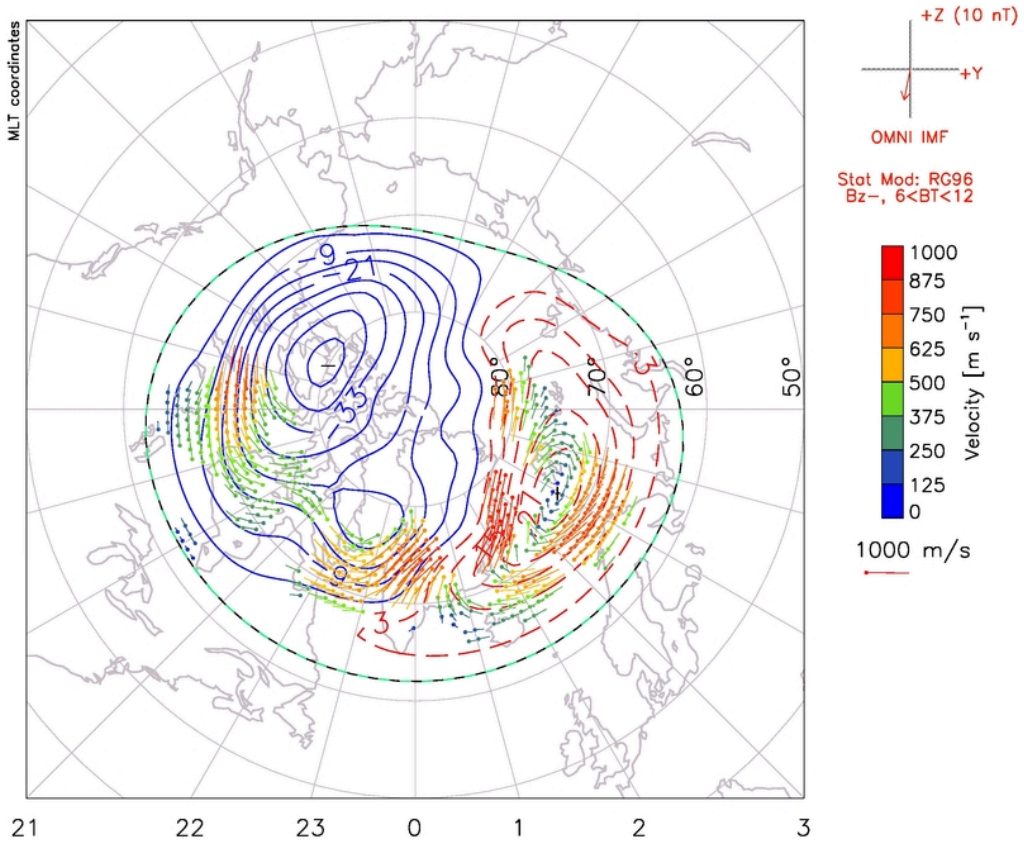

Figure 5.2: Global convection map of the SuperDARN radars during the substorm interval, April 20, 1999, at 01:30–01:32 UT. The order of fit is 8. Radial co-ordinates represent magnetic latitude differences starting from 50° and the radial lines represent MLT (magnetic local time) meridians, with noon at the top and midnight at the bottom. The dots at the beginning of the vectors indicate the vector locations, the lines show the vector direction, and the colors and length of the lines show the vector magnitude. The velocity scale is shown at the right side of the figure. Solid (dotted) contours are associated with negative (positive) values of electrostatic potential. IMF condition is at the top-right corner of the figure. [`superdarn.org`]

Figure 5.3 presents images of auroral activity measured from the LBHL filter of the Polar UVI spacecraft at 00:21:03, 00:39:27, 01:19:19, and 01:49:59 UT in a magnetic local time-magnetic latitude coordinate system. All of the images are presented in a uniform magnetic latitude-MLT coordinate system, with a minimum of 60° magnetic latitude. Auroral intensity is color coded according

to the color scale shown at the top of the figure. For clarity, dark red indicates high auroral intensity which was seen particularly at $\sim$ 01:20 and $\sim$ 01:50 UT in the dusk and midnight sector. The evidence of auroral activity during the substorm onset was reported at 01:31 UT.

Usually during an auroral substorm, the brightest UV emissions occur in the pre-midnight and post-midnight sectors, between 21:00 and 03:00 MLT. The distribution of auroral emissions during the substorm interval indicates exceptional features as the auroral substorm bulge is predominantly in the pre-midnight region. The remnants of the substorm auroral bulge are exhibited in the post-midnight sector during the substorm recovery phase (01:49:59 UT in Figure 5.3). The most poleward location of the auroral oval was recorded below 75° on April 20, 1999.

5.2 Discussion of the occurrence of multiple peaks in the Directional Derivative of Flow

Since SuperDARN OCB is estimated from the velocities measured in an ionospheric two cell convection map, there might be a secondary peak in the directional derivative of flow at different latitudes along the magnetic meridian. First, the occurrence of multiple peaks in the directional derivative of SuperDARN flow at four time points (0:22 UT, 00:40 UT, 01:20 UT, and 01:50 UT) on April 20, 1999 is discussed. The left panel of Figure 5.4 and 5.5 show the occurrence of multiple peaks in the directional derivative of SuperDARN flow at the four time-points while the right panel shows the location of OCB detected from the primary and secondary peaks in the directional derivative of SuperDARN flow and the Polar UVI spacecraft. The latitudinal locations of OCB proxies associated with the primary peak in the directional derivative of

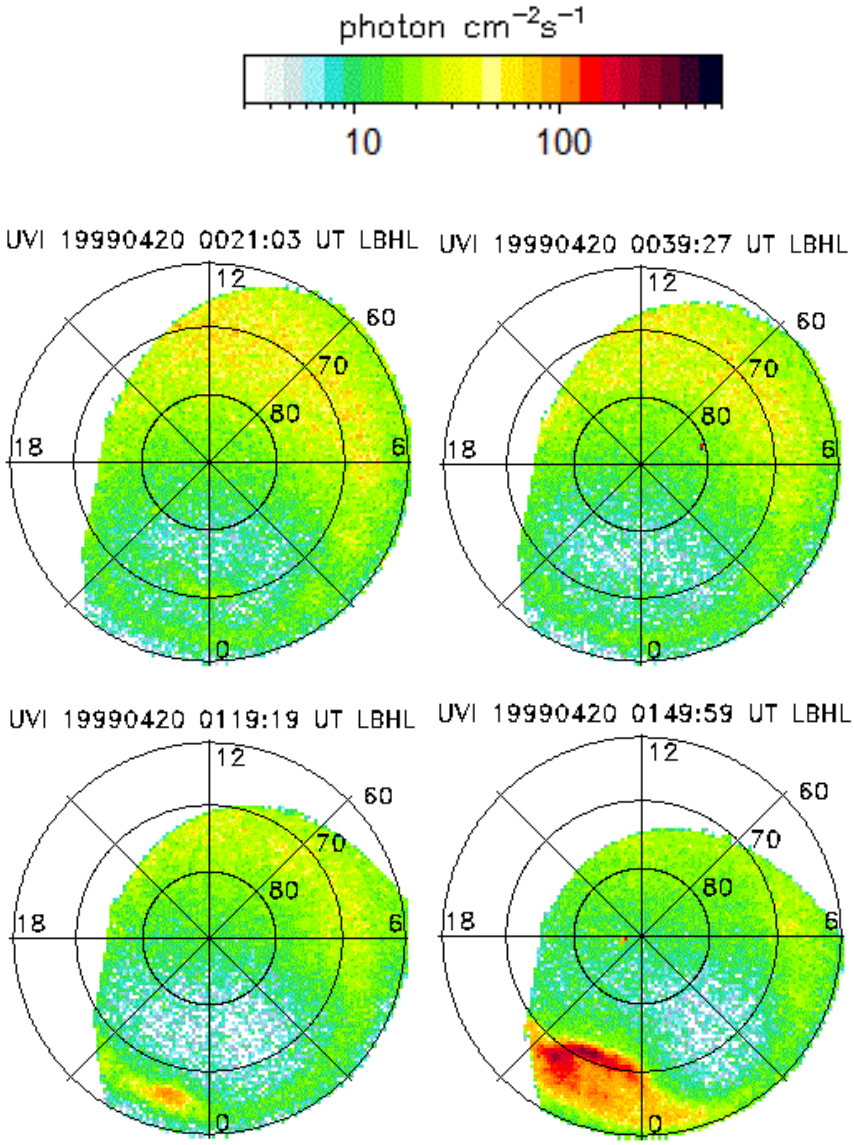

Figure 5.3: Images of the UV aurora in the 164–178 nm band taken at 00:21:03, 00:39:27, 01:19:19, 01:49:59 UT on April 20, 1999 through the LBHL filter of the Polar UVI spacecraft. The time at which the image was taken is indicated above each image. Solid circles represent 60°, 70°, and 80° MLAT, and radial lines represent MLT meridians at midnight, morning, noon, and evening, with noon at the top and midnight at the bottom. Auroral intensity is color coded according to the color scale located at the top of the panel.

SuperDARN plasma flow, LBHS and LBHL filters on the Polar UVI are marked as 'black-box', 'green-diamond', 'blue-plus' respectively. The SuperDARN sec-

ondary peak, if available is marked as 'sky blue-triangle. The asymmetry of the dawn and dusk cells occurs at all time points i.e., the sign of IMF B_y is nonzero. At the first two time points (00:22, and 00:40 UT) the dusk cell is rounded and the dawn cell is crescent shape due to the fact that the IMF B_y is predominantly positive. Therefore multiple peaks in the directional derivative of flow occur mostly in the pre-midnight sector for the first two intervals. At 01:20 UT, the multiple peaks in the directional derivative of flow occur in the post-midnight sector as the IMF B_y is negative in magnitude. IMF is southward for the first three points (00:22, 00:40 and 01:20 UT), while IMF B_z is positive for the fourth time point, at 01:50 UT. The two cell-pattern breaks under the positive IMF B_z component with 5 nT in magnitude (see figure 5.1). Huang et al. showed that if $\left|\frac{B_z}{B_y}\right| \approx 1$ the convection cell appears as three complicated cell pattern [68]. Therefore although B_y is positive at 01:50 UT, the multiple peaks in the directional derivative of flow occurred in the post-midnight instead of the pre-midnight sector under the three convection cell pattern.

The directional derivative of the convection flow speed maps in the left panels of Figure 5.6 and 5.7 show the occurrences of multiple peaks in the directional derivative of SuperDARN flow in the pre-midnight to midnight sectors for the other two events. The timepoints shown correspond to 08:46 UT on November 04, 2001, and two time points at 06:10 and 07:00 UT on October 14, 2001. The right panels show the location of the OCB determined from both the primary and secondary peaks in the directional derivative of SuperDARN flow and the IMAGE FUV spacecraft. The latitudinal locations of OCB proxies determined from the primary peak in the directional derivative of SuperDARN flow, SI-12, SI-13 and WIC filters on the IMAGE FUV are marked as 'black-box', 'blue-plus', 'green-diamond', 'red-cross' respectively (on the right panel). The SuperDARN secondary peak, if available is marked as 'sky blue-triangle. Like the previous time points, the asymmetry of the two convection cells occurs

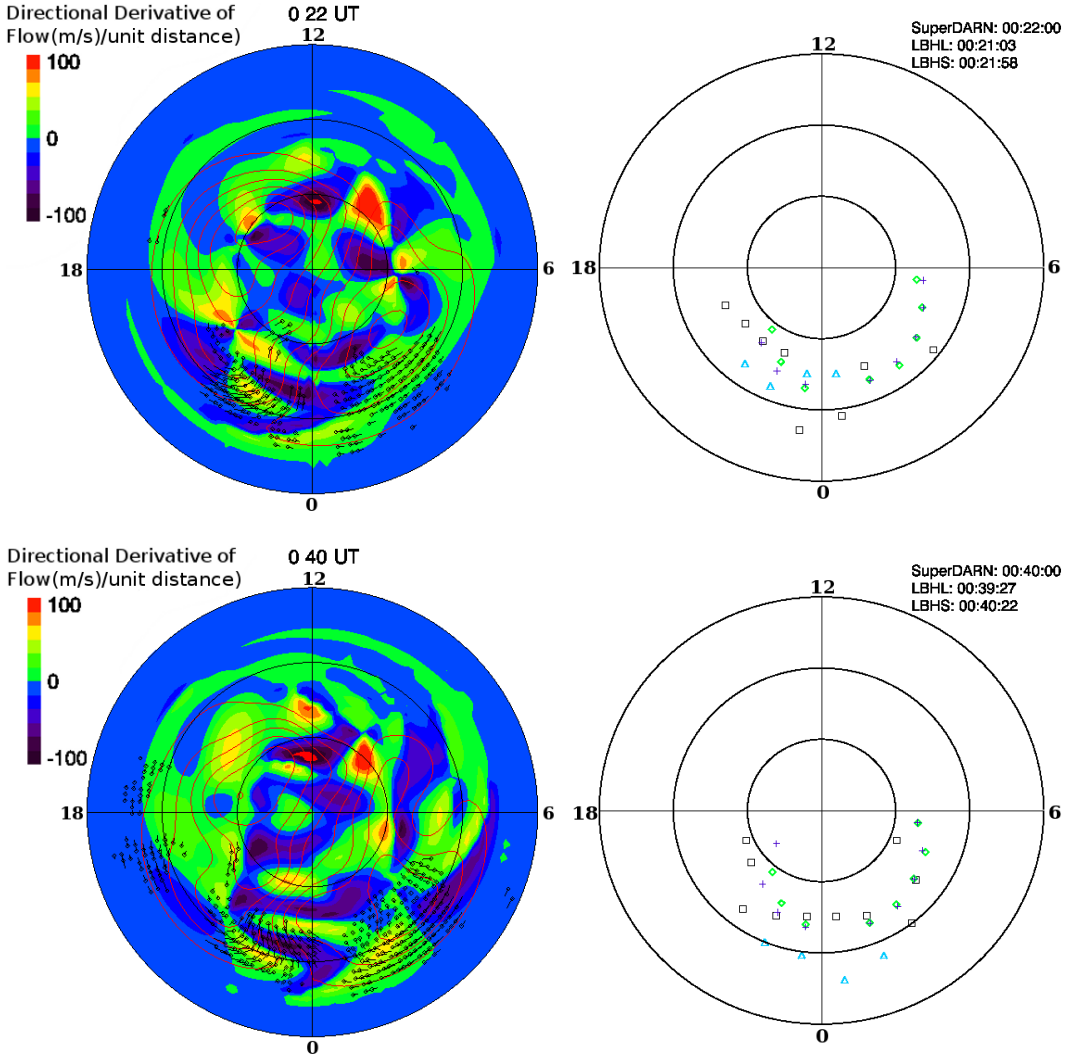

Figure 5.4: Left Panel: Measurements of SuperDARN convection flow directional derivatives taken on April 20, 1999. At the times 00:22 UT and 00:40 UT the directional derivative of the convection flow map shows the locations of positive peaks during the interval. Right Panel: Comparison of OCB derived from Polar UVI and SuperDARN multiple peaks in the directional derivative of flow. SuperDARN OCB (primary peak in the directional derivative of flow) (black-box), SuperDARN secondary peak (if available) (sky blue-triangle), the OCB defined by the LBHS (green-diamond), and the OCB defined by the LBHL (blue-plus). The top-right corner of each panel indicates the time at which the OCB was measured from the Polar UVI detectors and the SuperDARN. Solid circles represent 60°, 70°, and 80° MLAT, and radial lines represent MLT meridians at midnight, morning, noon, and evening, with noon at the top and midnight at the bottom.

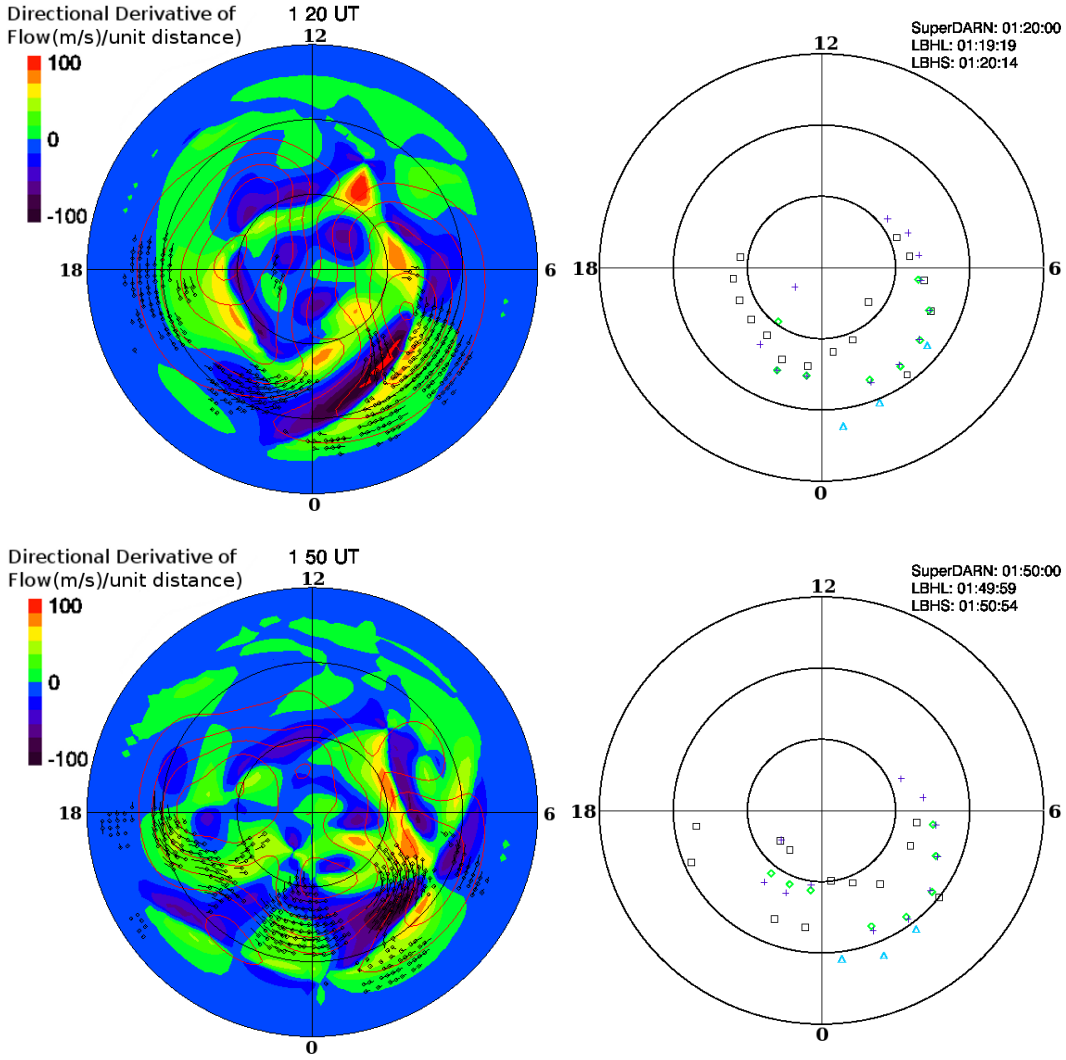

Figure 5.5: Left Panel: Measurements of SuperDARN convection flow directional derivatives taken on April 20, 1999. At the times 01:20 UT and 01:50 UT the directional derivative of the convection flow map shows the locations of positive peaks during the interval. Right Panel: Comparison of OCB derived from Polar UVI and SuperDARN multiple peaks in the directional derivative of flow. SuperDARN OCB (primary peak in the directional derivative of flow) (black-box), SuperDARN secondary peak (if available) (sky blue-triangle), the OCB defined by the LBHS (green-diamond), and the OCB defined by the LBHL (blue-plus). The top-right corner of each panel indicates the time at which the OCB was measured from the Polar UVI detectors and the SuperDARN. Solid circles represent 60°, 70°, and 80° MLAT, and radial lines represent MLT meridians at midnight, morning, noon, and evening, with noon at the top and midnight at the bottom.

when the IMF B_y component is non-zero.

The multiple peaks in the directional derivative of flow occur in the pre-midnight sector at 08:46 UT on November 04, 2001 under a southward IMF condition with a positive IMF B_y component. The primary peak in the pre-midnight sector is embedded in the low-latitude part of the dusk cell that flows westward. The secondary peak is at higher latitude associated with eastward flows within the dawn convection cell. The primary positive peak in the directional derivative of SuperDARN flow in the post-midnight sector is located at a similar latitudinal location within the dawn convection cell as the secondary peak in the pre-midnight region.

Although the IMF B_y component is negative for both time points on October 14, 2001 events, the multiple peaks occur predominantly at the pre-midnight region embedded in the crescent-shaped dusk convection cell. At 06:10 UT, the latitudinal location of the secondary peak in the directional derivative of flow are at lower latitude while the primary peak in the directional derivative of flow are at higher latitude ($< 80^\circ$ magnetic latitude between 21.5 to 23.5 MLT) inside the dusk convection cell. At 07:00 UT, primary peak in the pre-midnight sector is embedded within the low-latitude part of the dusk cell that flows westward while the secondary peak is at higher latitude embedded within eastward plasma flow associated with a crescent shaped extension of the dusk cell across midnight.

5.3 Comparisons

To investigate the location of the OCB when multiple peaks in the directional derivative of flow occur at a given MLT, the peaks need to be compared with

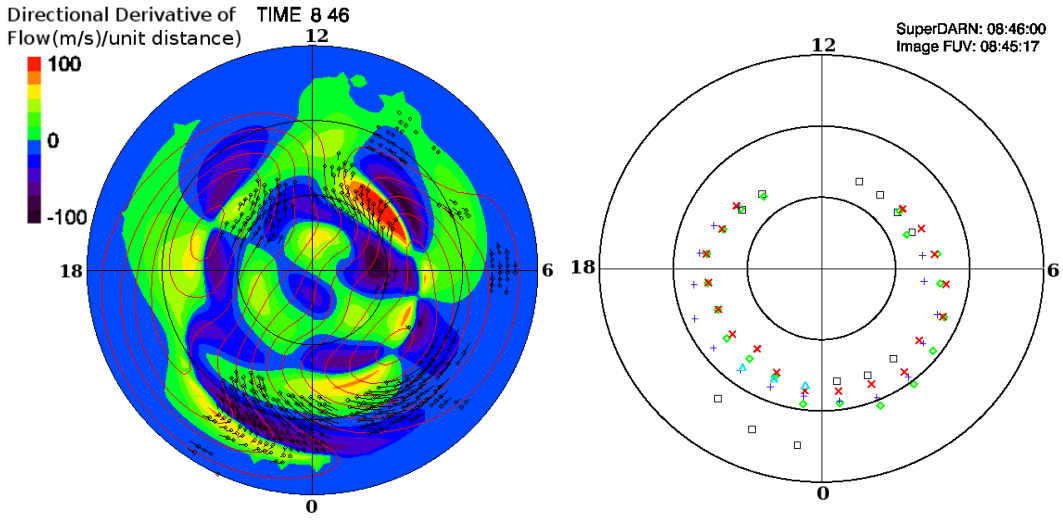

Figure 5.6: Left Panel: Measurements of the directional derivatives of SuperDARN plasma flow taken on November 04, 2001 at the time 08:46 UT (chapter 3 event). Right Panel: OCBs defined by the SuperDARN convection flow directional derivatives (black-box), the WIC (red-cross), the SI-13 (green-diamond), the SI1-2 (blue-plus), and SuperDARN secondary peak (if available) (sky blue-triangle). Solid circles represent 60°, 70°, and 80° MLAT, and radial lines represent MLT meridians at midnight, morning, noon, and evening, with noon at the top and midnight at the bottom.

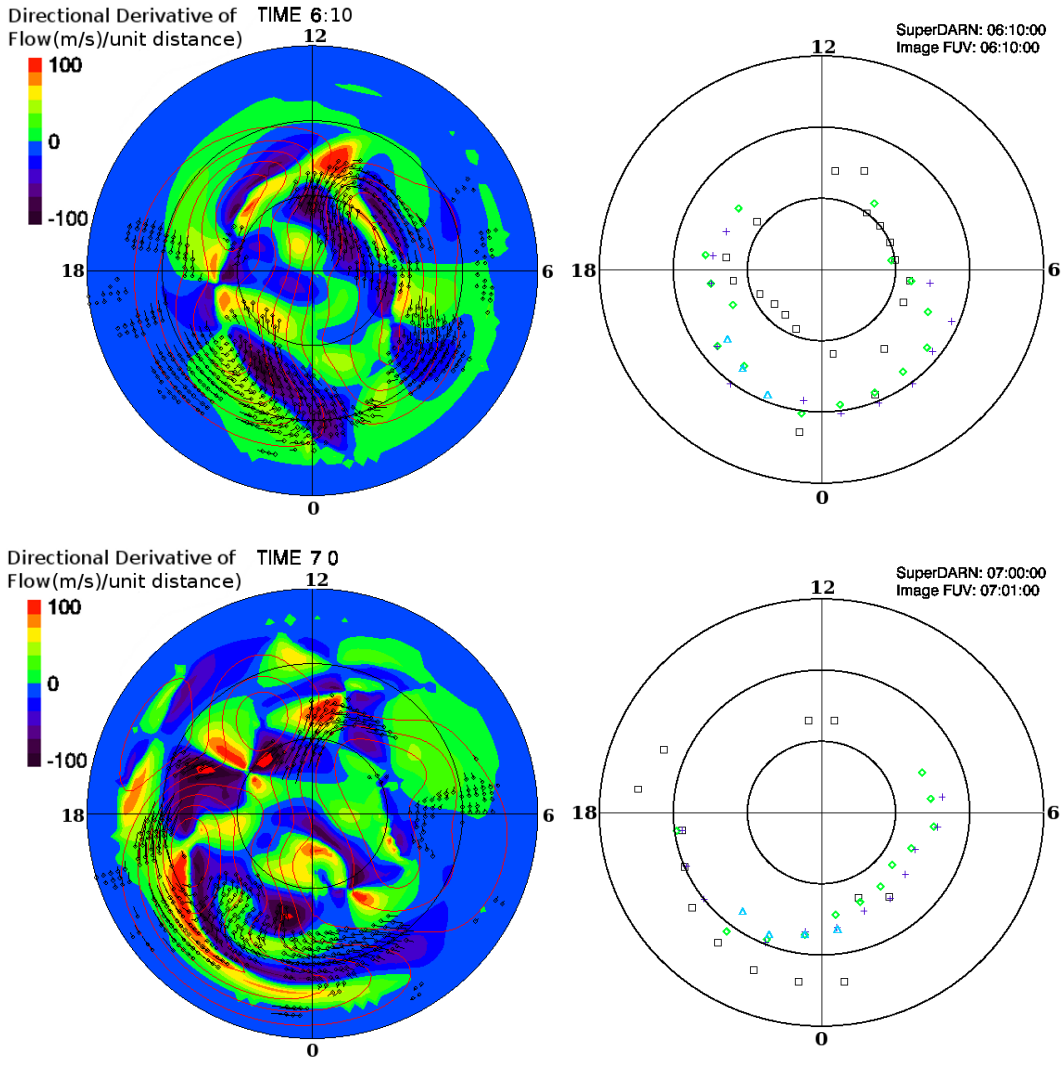

Figure 5.7: Left Panel: Measurements of the directional derivatives of SuperDARN plasma flow taken on October 14, 2001 at the time 06:10 UT and 07:00 UT (chapter 4 events). Right Panel: OCBs defined by the SuperDARN convection flow directional derivatives (black-box), the WIC (red-cross), the SI-13 (green-diamond), the SI1-2 (blue-plus), and SuperDARN secondary peak (if available) (sky blue-triangle). Solid circles represent 60°, 70°, and 80° MLAT, and radial lines represent MLT meridians at midnight, morning, noon, and evening, with noon at the top and midnight at the bottom.

the OCB determined by ultraviolet measurements. As shown in the first time point in Figure 5.4 on the right panel (00:22 UT on April 20, 1999) the higher latitude peak of flow measured by SuperDARN are collocated with the OCBs measured from the Polar UVI spacecraft. OCB could not be measured at 0.5 MLT from the Polar UVI at the time point. Similarly, higher latitude peaks are collocated with ultraviolet measurements at 00:40 UT while lower latitude peaks agreed with UVI boundaries at 01:20 and 01:50 UT, as shown in Figure 5.4 and 5.5. At 08:46 UT on November 04, 2001 (right panel in Figure 5.6), the latitudinal locations of the secondary peak at higher latitudes agrees well with the boundaries determined by the IMAGE FUV detectors. The peak in the directional derivative of flow at lower latitude in the pre-midnight sector is collocated with the IMAGE FUV measurements at 06:10 UT on October 14, 2001 (right panel in Figure 5.7). At 07:00 UT the peak at higher latitude are collocated with the IMAGE FUV measurements at all MLT.

Table 5.1 represents a summary of the occurrence of the multiple peaks in the directional derivative of flow. As from the table, the lower latitude secondary peaks predominantly agrees with the UVI poleward boundary at three time points (01:20, 01:50 UT on April 04, 199 and 06:10 UT on October 14, 2001) and in almost all cases, except for two, the secondary peak agrees with the UVI boundary. The two cases where the agreement is at the higher latitude secondary peak are at 08:46 UT on November 4, 2001 and at 07:00 UT on October 14, 2001. The higher latitude primary peak agrees with UVI measurements for two cases (00:22 UT and 00:40 UT on April 04, 1999). The lower latitude primary peaks are collocated with UVI boundaries in 21.5 MLT at 07:00 UT on October 14, 2001. The comparison indicates that the primary peak may not identify the OCB as the secondary peak predominantly agrees with the ultraviolet measurements.

Table 5.1: Summary of the Occurrence of the Multiple Peaks in the Directional Derivative of Flow

Date	UT	IMF B_z condition	IMF B_y condition	Region of the multiple peaks	Latitudinal location of the peak in agreement with UVI	Type of peak in agreement with UVI
April 04, 1999	00:22	Southward	Positive	Dawn and dusk cell	Higher latitude	Primary peak, except for 23.5 MLT
	00:40	Southward	Positive	Dawn and dusk cell	Higher latitude	Primary peak
	01:20	Southward	Negative	Dusk cell	Lower latitude	Secondary peak
	01:50	Northward	Positive	Dusk cell	Lower latitude	Secondary peak
Nov 04, 2001	08:46	Southward	Positive	Dawn and dusk cell	Higher latitude	Secondary peak
Oct 14, 2001	06:10	Southward	Negative	Dusk cell	Lower latitude	Secondary peak
	07:00	Southward	Negative	Dawn and dusk cell	Higher latitude, except for 21.5 MLT	Secondary peak, except for 21.5 MLT

5.4 Summary

The occurrences of multiple peaks in the directional derivative of flow in the midnight sector during substorm intervals are discussed. During these intervals the IMF is predominantly southward and B_y is significant. The results indicate that multiple peaks in the directional derivative of flow were detected only close to the region where ionospheric convection cells overlapped each other. When the IMF B_y component is positive, the asymmetric convection cells appear to be "orange" -like in the dusk cell and "banana" -like in the dawn cell in the northern hemisphere. Evidence for the relationship between the asymmetry of the ionospheric convection cell and the clock orientation of the IMF were discussed by Ruohoniemi and Greenwald (1995, 1996, 2005) [104]; [63] [105]. Due to the asymmetry, the anti-sunward flow of plasma inside the polar cap

area does not flow parallel to the anti-sunward direction but rather flows towards dusk. This can result in an overlap of the dusk and dawn cells along MLT meridians around midnight and the occurrence of multiple peaks in the directional derivative of flow. Multiple peaks in the directional derivative of flow predominantly occur between the two cell boundaries and within the dawn and dusk convection cell.

The agreement between the latitudinal locations of the primary and secondary peaks in the directional derivative of SuperDARN flow and the poleward boundaries of ultraviolet emissions was also examined. The multiple peaks in the directional derivative of flow discussed in this chapter occurs during substorm intervals in the pre-midnight to post-midnight regions that is associated with IMF B_y asymmetry of the dawn and dusk convection cells. Thus the identification of the OCB with respect to the ultraviolet measurement is not straightforward. The results suggest that the OCB is most often going to be associated with the secondary peak in the directional derivative of flow and thus during such events the primary peak may not be a good proxy for the OCB.

Similar to the midnight sector, multiple peaks in the directional derivative of flow may be observed at noon due to the presences of overlapped convection cells in the noon sector. Further investigations would probably discover multiple peaks in the directional derivative of flow on other MLT meridians.

Multiple peaks in the directional derivative of flow that appear in the presence of other ionospheric convection patterns need to be investigated. For example, during the northward IMF, the two cell convection pattern breaks into a multiple complex cell pattern. The morphology of ionospheric convection in the presence of a strongly northward IMF is not fully understood.

Chapter 6

Concluding Remarks

The overarching goal of this thesis has been to develop new tools for understanding magnetospheric dynamics via an investigation of the directional derivatives of the ionospheric convection flow speed. Ionospheric convection is directly coupled, via the Earth's magnetic field lines, to plasma convection in the magnetosphere which is driven by magnetic reconnection at the magnetopause and magnetotail. This thesis is a case study analysis of the directional derivative of SuperDARN convective flow. The results of this thesis show that maxima in the directional derivative of flow can be a good indicator of the open-closed boundary (OCB) when compared with other OCB proxies such as ultra-violet auroral emission boundaries and particle precipitation boundaries. The accuracy of this new technique depends upon magnetic local time, magnetic activity level, and data coverage.

The identification of new techniques for identifying the OCB is important because current techniques of determining OCB have some limitations. For instance, the most reliable technique, particle precipitation boundary (PPB) from low altitude DMSP spacecraft provide only single point OCB locations during each orbital period and thus cannot determine the OCB globally for all MLT at a specific UT. To overcome this problem, poleward boundaries of ultraviolet

auroral emissions imaged by high altitude spacecraft such as Polar ultraviolet imager (UVI) or the Image far ultraviolet detector (FUV) are used to determine the OCB globally. Multiple cameras on these spacecraft image different ultraviolet energies corresponding to different precipitating particle energies and thus the OCB proxies measured by the different cameras will vary. The accuracy of the ultraviolet image boundaries is also dependent on magnetic local time. Thus it is advantageous to have another means of global OCB determination such as the SuperDARN convection flow directional derivative technique outlined in this thesis.

The directional derivative of SuperDARN flow method for identifying the OCB is based upon the following premise. According to observations, MHD theory and simulations, Plasma flow decreases prior to reconnection and increases after reconnection, hence a positive peak in the directional derivative of flow may be associated with magnetic reconnection between open and closed field lines and thus is a signature of the OCB.

The directional derivative of flow measured from the SuperDARN convection map was tested during an extended substorm growth phase event. The temporal evolution of the SuperDARN directional derivative OCB proxies were compared with the ultraviolet poleward boundary OCB proxy. The result shows that OCB proxies measured from the peak of the directional derivative of SuperDARN flow agreed with the ultraviolet measurements at almost all magnetic local times. Although continuous detection of the boundary could not be measured using the PPB method, data from the satellite particle precipitation measurements from DMSP spacecraft are used to calibrate other OCB proxies. The result indicates that the boundaries measured from the peak in the directional derivative of flow agreed well with the DMSP measurements. In addition the Doppler spectral width boundary (SWB) in the midnight and

dawn sector was tested and the observation indicated that the Doppler SWB does not reliably identify the OCB during the interval.

The OCB proxies were also tested during two substorm events with different solar wind conditions. It is observed that the OCB proxies moved equatorward in the dusk sector and poleward in the midnight sectors at the substorm onset. During the intervals, temporal evolution of SuperDARN boundaries followed the trend line of ultraviolet boundaries. The low order of disagreement and the similar trend line indicate that the SuperDARN OCB might be a useful proxy for the dawn and dusk sector during substorm intervals. However, the OCB measured from the Polar UVI is is significantly poleward of the SuperDARN measurement in the dusk sector during the substorm interval.

The occurrence of the multiple peaks in the directional derivative of flow in the pre- and post-midnight sectors is also observed during the substorm intervals when the IMF B_y component is non-zero. The asymmetry of the two convection cell convection pattern arises and hence the multiple peaks occur. The multiple peaks in the directional derivative of flow are compared with the boundaries measured from the ultraviolet detectors. Usually the secondary peak agrees with the OCB proxies measured from the ultraviolet detectors in the midnight sector during the intervals.

The flow directional derivative technique, therefore, can be used with confidence during the southward IMF steady solar wind condition at almost all MLT. The flow directional derivative is also a reliable indicator of the OCB proxy in the dusk sector during the substorm interval. However, it should be used with caution under the occurrence of multiple peaks in the directional derivative of flow.

The root mean square deviations between the SuperDARN and IMAGE FUV

OCB proxy techniques indicate that absolute differences between the two methods range from 1° to 3°. The degree of difference between OCB proxies is typical of established techniques. Such differences in latitudinal location can be mapped into the magnetosphere. On the nightside, the 2°–3° latitudinal difference, if mapped into the magnetosphere would certainly map to significantly different locations and may reach $\sim 50\ R_e$ along the center of the stretched plasma sheet.

One potential future application of this technique is to use it to determine the polar cap area, which encompasses the region of open field lines. If the directional derivative of SuperDARN flow OCB proxy is available at all magnetic local times then it can be used for such a measurement. The polar cap area is a useful indicator of the degree of solar wind – magnetosphere coupling. When the polar cap area is small the coupling of solar wind mass and energy into the magnetosphere is low, and when the polar cap area is large, particularly during the southward IMF, the coupling is high. For example, during the substorm growth phase the polar cap area expands from $\sim 0.5 \times 10^7\ km^2$ to $\sim 1.5 \times 10^7 km^2$ [106]. The rate of polar cap growth depends on the magnitude of IMF B_z [107]; [108]; [106]; [109].

This new technique could be further evaluated during steady state solar wind events corresponding to IMF conditions other than southward IMF. Evaluating numerous events could allow full statistical study, and combined MHD model or case study events would lead to better understanding the relation between the peaks in the directional derivatives and magnetospheric phenomena.

The primary goals of this thesis therefore have been achieved. This thesis has presented a new experimental technique for identification of the open closed field line boundary. The proposed technique is evaluated with other established

techniques. Determining the open closed field line boundary is a somewhat controversial topic. The space science community has been hesitant to accept OCB proxies except for the low altitude particle precipitation measurement. Since the PPB cannot provide OCB for the entire hemisphere, OCB proxies from ultraviolet detectors are used. Therefore, the SuperDARN flow directional derivative technique might provide an additional reliable proxy for determining the OCB globally. Hopefully the work presented in this thesis will be useful for determining the OCB.

Bibliography

[1] C. T. Russell, R. C. Snare, J.D. Means, D. Pierce, D. Dearborn, M. Larson, G. Barr, and G. Le. The GGS/POLAR magnetic fields investigation. *Space Sc*, 71:563–582, 1995.

[2] W. J. Hughes. *Introduction to Space Physics*. Cambridge University Press, 1995.

[3] M. G. Kivelson and C. T. Russell. *Introduction to Space Physics*. Cambridge University Press, 1995.

[4] W. Baumjohann and R. A. Treumann. *Basic Space Plasma Physics*. Imperial College Press, 1997.

[5] E. N. Parker. Dynamics of the interplanetary gas and magnetic fields. *Astrophysical Journal*, 128:664, 1958. doi: 10.1086/146579.

[6] D. A. Gurnett and A. Bhattacharjee. *Introduction to Plasma Physics: With Space and Laboratory Applications*. Cambridge University Press, 2005.

[7] S. Chapman and V. C. A. Ferraro. A new theory of magnetic storms. *Terrestrial Magnetism*, 36:171–186, 1931.

[8] C. T. Russell. Planetary magnetospheres. *Science Progress*, 75:93–105, 1991.

[9] C. T. Russell and R. J. Walker. Flux transfer events at mercury. *Journal of Geophysical Research*, 90:11,067–11,074, 1985.

[10] E. C. Roelof and D. G. Sibeck. Magnetopause shape as a bivariate function of interplanetary magnetic field B_z and solar wind dynamic pressure. *Journal of Geophysical Research: Space Physics*, 98:2142121450, 1993.

[11] U. Villante. Some remarks on the structure of distant neutral sheet. *Planet Space Science*, 28:723–728, 1975. doi: 10.1016/0032-0633(75)90110-5.

[12] M.B. Moldwin, L. Downward, H.K. Rassoul, R. Amin, and R.R. Anderson. A new model of the location of the plasmapause: CRRES results. *Journal of Geophysical Research*, 107(A11):SMP 2–1–SMP2–9, 2002. doi: 10.1029/2001JA009211.

[13] R. A. Greenwald, K. B. Baker, J. R. Dudeney, M. Pinnock, T. B. Jones, E. C. Thomas, J.-P. Villain, J.-C. Cerisier, C. Senior, C. Hanuise, R. D. Hunsucker, G.Sofko, J. Koehler, E. Nielsen, R. Pellinen, A. D. M. Walker, N. Sato, and H. Yamagishi. Darn/SuperDARN: A global view of the dynamics of high-lattitude convection. *Space Science Reviews*, 71:761–796, 1995. doi: 10.1007/BF00751350. URL `http://articles.adsabs.harvard.edu/full/1995SSRv...71..761G/0000761.000.html`.

[14] J. W. Dungey. Interplanetary magnetic field and the auroral zones. *Physical Review Letters*, 6:47–48, 1961. doi: 10.1103/PhysRevLett.6.47. URL `http://link.aps.org/doi/10.1103/PhysRevLett.6.47`.

[15] S.W.H. Cowley and M. Lockwood. Excitation and decay of solar wind-driven flows in the magnetosphere-ionophere system. *Annales Geophysicae*, 10:103–115, 1992.

[16] M. F. Smith and M. Lockwood. Earth's magnetospheric cusps. *Reviews of Geophysics*, 34:233–260, 1996. doi: 10.1029/96RG00893.

[17] P. A. Sweet. The neutral point theory of solar flares. In B. Lehnert, editor, *Electromagnetic Phenomena in Cosmical Physics*, volume 6 of *IAU Symposium*, page 123, 1958.

[18] E.N. Parker. Sweet's mechanism for merging magnetic fields in conducting fluids. *Journal of Geophysical Research*, 62: 509-520. doi::509–520, 1957. doi: 10.1029/jz062i004p00509.

[19] H. E. Petschek. Magnetic field annihilation. *NASA Special Publication*, 50:425, 1964.

[20] B. U. O Sonnerup. Magnetopause reconnection rate. *Journal of Geophysical Research*, 79:1546–1549, 1974. doi: 10.1029/JA079i010p01546.

[21] N. Katz, J. Egedal, W Fox, A. Le, J. Bonde, and A. Vrublevskis. Laboratory observation of localized onset of magnetic reconnection. *Physical Review Letters*, 104:255004, 2010. doi: 10.1103/PhysRevLett.104.255004. URL `http://hdl.handle.net/1721.1/60572`.

[22] G. S. Lakhina. Magnetic reconnection. *Bulletin of the Astronomical Society of India*, 28:593–646, 2000.

[23] K. Schindler. *Magnetic Reconnection in Space and Laboratory Plasmas*. AGU, Washington DC, 1984. doi: 10.1029/GM030p0365.

[24] D. B. Melrose. *Instabilities in space and laboratory plasmas*. Cambridge University Press, Cambridge, 1986.

[25] Z. F. Fu and L. C. Lee. Simulation of multiple X-line reconnection at the dayside magnetopause. *Geophysical Research Letters*, 12:291–294, 1985.

[26] T.G. Forbes and E.R. Priest. On reconnection and plasmoids in the geomagnetic tail. *Journal of Geophysical Research*, 88:863–870, 1983. doi: 10.1029/JA088iA02p00863.

[27] G.S. Lakhina. A kinetic theory of driven reconnection in the earth's magnetotail. *Journal of Geophysical Research*, 97:29612972, 1992. doi: 10.1029/91JA01325.

[28] G. S. Lakhina. On the ion-tearing instability of forced current sheets. *Journal of Geophysical Research: Space Physics*, 98:17409–17414, 1993. doi: 10.1029/93JA00896.

[29] B.U.O. Sonnerup, G. Paschmann, I. Papamastorakis, N. Sckopke, J. R. Asbridge G. Haerendel, S. J. Bame, J. T. Gosling, and C. T. Russell. Evidence for magnetic field reconnection at the earth's magnetopause. *Journal of Geophysical Research*, 86:10,049 – 10,067, 1981.

[30] O. de la Beaujardiere, D. Alcayde, J. Fontanari, and C. Leger. Seasonal dependence of high-latitude electric fields. *Journal of Geophysical Research: Space Physics*, 96:57235735, 1991. doi: 10.1029/90JA01987.

[31] M. Pinnock, G. Chisham, I. Coleman, J. Freeman, M. P. Hariston, and J.-P Villain. The location and rate of dayside reconnection during an interval of southward interplanetary magnetic field. *Annales Geophysicae*, 21:1467–1482, 2003.

[32] G.T. Blanchard, L. R. Lyons, O. de la Beaujardiere, R. A. Doe, and M. Mendillo. Measurement of the magnetotail reconnection rate. *Journal of Geophysical Research*, 101:15,265–15,276, 1996. doi: 10.1029/96JA00414. URL `http://www.agu.org/pubs/crossref/1996/96JA00414.shtml`.

[33] H. S. Fu, Yu. V. Khotyaintsev, A. Vaivads, A. Retino, and M. Andre. Energetic electron acceleration by unsteady magnetic reconnection. *Nature Physics*, 9:426430, 2013. doi: 10.1038/nphys2664.

[34] J. Egedal, W. Daughton, and A. Le. Large-scale electron acceleration by parallel electric fields during magnetic reconnection. *Nature Physics*, 8: 321324, 2012. doi: 10.1038/nphys2249.

[35] S.-I. Akasofu. The development of the auroral substorm. *Planetary and Space Science*, 12(4):273282, 1964. doi: 10.1016/0032-0633(64)90151-5.

[36] G. Rostoker, S. I. Akasofu, R.A. Greenwald J. Foster, Y. Kamide, K. Kawasaki, A.T.Y. Lui, R.L. McPherron, and C.T. Russell. Magnetospheric substormsdefinition and signatures. *Journal of Geophysical Research*, 85:1663–1668, 1980. doi: 10.1029/JA085iA04p01663.

[37] J. C. Samson, L. R. Lyons, P. T. Newell, F. Creutzberg, and B. Xu. Proton aurora and substorm intensifications. *Geophysical Research Letters*, 19:2167–2170, 1992. doi: 10.1029/92GL02184.

[38] V. Angelopoulos, J. P. McFadden, D. Larson, C. W. Carlson, S. B. Mende, H. Frey, T. Phan, D. G. Sibeck, K. H. Glassmeier, U. Auster, E. Donovan, I. R. Mann, I. J. Rae, C. T. Russell, A. Runov, X. Z. Zhou, and L. Kepko. Tail reconnection triggering substorm onset. *Science*, 321: 931–935, 2008. doi: 10.1126/science.1160495.

[39] N. U. Crooker. Reverse convection. *Journal of Geophysical Research*, 97(A12):19,36319,372,, 1992. doi: 10.1029/92JA01532.

[40] M. Lockwood, H. C. Carlson Jr., and P. E. Sandholt. Implications of the altitude of transient 630-nm dayside auroral emissions. *Journal of Geophysical Research*, 98(A9):15,571–15,587, 1993.

[41] G. T. Blanchard, L. R. Lyons, J. C. Samson, and F. J. Rich. Locating the polar cap boundary from observations of 6300 A auroral emission. *Journal of Geophysical Research*, 100(A5):7855–7862, 1995. doi: 10.1029/94JA02631.

[42] L. C. Evans and E. C. Stone. Electron polar cap and the boundary of open geomagnetic field lines. *Journal of Geophysical Research*, 77(28): 5580–5584, 1972.

[43] P. T. Newell and C. I. Meng. Mapping the dayside ionosphere to the magnetosphere according to particle precipitation characteristics. *Geophysical Research Letters*, 19:609–612, 1992. doi: 10.1029/92GL00404.

[44] K. B. Baker, J. R. Dudeney, R. A. Greenwald, M. Pinnock, P. T. Newell, A. S. Rodger, N. Mattin, and C. .-I. Meng. Hf radar signatures of the cusp and low-latitude boundary layer. *Journal of Geophysical Research*, 100(A5):76717695, 1995. doi: 10.1029/94JA01481.

[45] D. N. Baker, A. J. Klimas, T. I. Pulkkinen, and R. L. McPherron. Reexamination of driven and unloading aspects of magnetospheric substrorms. *Journal of Geophysical Research*, 102(A4):7169–7177, 1997. doi: 10.1029/96JA02627.

[46] M. R. Torr, D. G. Torr, M. Zukic, R. B. Johnson, J. Ajello, P. Banks, K. Clark, K. Cole, C. Keffer, G. Parks, B. Tsurutani, and J. Spann. A far ultraviolet imager for the international solar-terrestrial physics mission. *Space Science Reviews*, 71:329–383, 1995. doi: 10.1007/BF00751335. URL `http://dx.doi.org/10.1007/BF00751335`.

[47] S. B. Mende, H. Heetderks, H. U. Frey, M. Lampton, S. P. Geller, S. Habraken, E. Renotte, C. Jamar, P. Rochus, J. Spann, S. A. Fuselier, J.-C. Gerard, R. Gladstone, S. Murphree, and L. Cogger. Far ultraviolet

imaging from the IMAGE spacecraft. 1. system design. *Space Science Reviews*, 91:243–270, 2000.

[48] S.B. Mende, H. Heetderks, H.U. Frey, J.M. Stock, M. Lampton, S.P. Geller, R. Abiad, O.H.W. Siegmund, S. Habraken, E. Renotte, C. Jamar, P. Rochus, J.-C. Gerard, R. Sigler, and H. Lauche. Far ultraviolet imaging from the IMAGE spacecraft. 3. spectral imaging of lyman-α and oi 135.6 nm. *Space Science Reviews*, 91:287–318, 2000.

[49] J. A. Wild, S. E. Milan, C. J. Owen, J. M. Bosqued, M. Lester, D. M. Wright, H. Frey, C. W. Carlson, A. N. Fazakerley, and H. Rme. The location of the open-closed magnetic field line boundary in the dawn sector auroral ionosphere. *Annales Geophysicae*, 22:3625–3639, 2004. doi: 10.5194/angeo-22-3625-2004.

[50] M. Lester, S. E. Milan, V. Besser, and R. Smith. A case study of HF radar spectra and 630.0 nm auroral emission in the pre-midnight sector. *Annales Geophysicae*, 19:327–339, 2001. doi: 10.5194/angeo-19-327-2001. URL `http://www.ann-geophys.net/19/327/2001`.

[51] G. Chisham and M. P. Freeman. An investigation of latitudinal transitions in the SuperDARN Doppler spectral width parameter at different magnetic local times. *Annales Geophysicae*, 22:1187–1202, 2004. doi: 10.5194/angeo-22-1187-2004. URL `www.ann-geophys.net/22/1187/2004/`.

[52] G. Chisham, M. P. Freeman, and T. Sotirelis. A statistical comparison of SuperDARN spectral width boundaries and DMSP particle precipitation boundaries in the nightside ionosphere. *Geophysical Research Letters*, 31: L02804, 2004. doi: 10.1029/2003GL019074.

[53] G. Chisham, M. P. Freeman, M. M. Lam, G. A. Abel, T. Sotirelis, R. A. Greenwald, and M. Lester. A statistical comparison of SuperDARN spec-

tral width boundaries and DMSP particle precipitation boundaries in the afternoon sector ionosphere. *Annales Geophysicae*, 12:3645–3654, 2005. doi: 10.5194/angeo-23-3645-2005. URL `http://www.ann-geophys.net/23/3645/2005/angeo-23-3645-2005.html`.

[54] G. Chisham, M. P. Freeman, T. Sotirelis, R. A. Greenwald, M. Lester, and J.-P. Villain. A statistical comparison of SuperDARN spectral width boundaries and DMSP particle precipitation boundaries in the morning sector ionosphere. *Annales Geophysicae*, 23:733–743, 2005. doi: 10.5194/angeo-23-733-2005. URL `http://www.ann-geophys.net/23/733/2005/angeo-23-733-2005.html`.

[55] G. Chisham, M. Lester, S. E. Milan, M. P. Freeman, W. A. Bristow, A. Grocott, K. A. McWilliams, J. M. Ruohoniemi, T. K. Yeoman, P. L. Dyson, R. A. Greenwald, T. Kikuchi, M. Pinnock, J. P. S. Rash, N. Sato, G. J. Sofko, J.-P. Villain, and A. D. M. Walker. A decade of the Super Dual Auroral Radar Network (SuperDARN): Scientific achievements, new techniques and future directions. *Surveys in Geophysics*, 28:33–109, 2007.

[56] J.-P. Villain, M. Pinnock R. Andre, R. A. Greenwald, and C. Hanuise. A statistical study of the Doppler spectral width of high-latitude ionospheric F-region echoes recorded with SuperDARN coherent HF radars. *Annales Geophysicae*, 20:17691781, 2002. doi: 10.5194/angeo-20-1769-2002.

[57] S. W. H. Cowley. *Excitation of flow in the Earth's magnetosphere-ionosphere system: observations by incoherent scatter radar, in Polar Cap Boundary Phenomena*, volume 509. NATO ASI Series C, Kluwer Academic Dordrecht, Holland, 1998.

[58] B. G. Fejer and M. C. Kelley. Ionospheric irregularities. *Reviews of Geophysics*, 18:401–454, 1980. doi: 10.1029/RG018i002p00401.

[59] E. Nielsen and K. Schlegel. Coherent radar doppler measurements and their relationship to the ionospheric electron drift velocity. *Journal of Geophysical Research*, 90:3498–3504, 1985. doi: 10.1029/JA090iA04p03498.

[60] P.-R. Chen, L. Yi, and E. Nielson. Variations of the mean phase velocity of 1-m ionospheric plasma waves with the plasma electron temperature. *Journal of Geophysical Research: Space Physics*, 100:1647–1652, 1995.

[61] J. M. Ruohoniemi, R. A. Greenwald, K. B. Baker, J. P. Villain, and M. A. McCready. Drift motions of small-scale irregularities in the high-latitude F region: An experimental comparison with plasma drift motions. *Journal of Geophysical Research*, 92(A5):4553–4564, 1987. doi: 10.1029/JA092iA05p04553. URL `http://www.agu.org/pubs/crossref/1987/JA092iA05p04553.shtml`.

[62] J. M. Ruohoniemi and K. B. Baker. Large-scale imaging of high-latitude convection with Super Dual Auroral Radar Network HF radar observations. *Journal of Geophysical Research*, 103(A9):20,797–20,811, 1998. doi: 10.1029/98JA01288.

[63] J. M. Ruohoniemi and R. A. Greenwald. Statistical patterns of high-latitude convection obtained from goose bay HF radar observations. *Journal of Geophysical Research*, 101(A10):21,74321,763, 1996. doi: 10.1029/96JA01584.

[64] S. G. Simon and J. M. Rhuohoniemi. Electrostatic potential patterns in the high latitude ionosphere constrained by SuperDARN measurements. *Journal of Geophysical Research*, 105(A10):23,005–23,014, 2000.

[65] P. H. Reiff and J. L. Burch. Imf B_y-dependent plasma flow and birkeland currents in the dayside magnetosphere: 2. a global model for northward

and southward IMF. *Journal of Geophysical Research: Space Physics*, 90:1595–1609, 1985. doi: 10.1029/JA090iA02p01595.

[66] R. A. Greenwald, W. A. Bristow, G. J. Sofko, C. Senior, J.-C. Cerisier, and A. Szabo. Super dual auroral radar network radar imaging of dayside high-latitude convection under northward interplanetary magnetic field: Toward resolving the distorted two-cell versus multicell controversy. *Journal of Geophysical Research: Space Physics*, 100:1966119674, 1995. doi: 10.1029/95JA01215.

[67] C.-S. Huang, D. M. George, J. Sofko, W. J. Hughes, and T. Moretto. Ionospheric convection response to changes of interplanetary magnetic field B_z component during strong B_y component. *Journal of Geophysical Research: Space Physics*, 105:5231–5243, 2000. doi: 10.1029/1999JA000099.

[68] C.-S. Huang, G. J. Sofko, A. V. Koustov, D. A. Andre, J. M. Ruohoniemi, R. A. Greenwald, and M. R. Hairston. Evolution of ionospheric multicell convection during northward interplanetary magnetic field with $|B_z/B_y|>$ 1. *Journal of Geophysical Research: Space Physics*, 105:27095–27107, 2000. doi: 10.1029/2000JA000163.

[69] N. U. Crooker. An evolution of antiparallel merging. *Geophysical Research Letters*, 13:1063–1066, 1986.

[70] E. Friis-Christensen and J. Wilhjelm. Polar cap currents for different directions of the interplanetary magnetic field in the y-z plane. *Journal of geophysical research*, 80:1248–1260, 1975.

[71] J. C. Dorelli, A. Bhattacharjee, and J. Raeder. Separator reconnection at earth's dayside magnetopause under generic northward interplanetary magnetic field conditions. *Journal of geophysical research*, 112, 2007. doi: 10.1029/2006JA011877.

[72] F. R. Fenrich, J. G. Luhmann, J. A. Fedder, S. P. Slinker, and Russell C. T. A global mhd and empirical magnetic field model investigation of the magnetospheric cusp. *Journal of geophysical research*, 106:18789–18802, 2001. doi: 10.1029/2001JA900040.

[73] W. W. White, G. L. Siscoe, G. M. Erickson, Z. Kaymaz, N. C. Maynard, K. D. Siebert, B. U. O Sonnerup, and D. R. Weimer. The magnetospheric sash and the cross-tail s. *Geophysical Research Letters*, 25:1605–1608, 1998. doi: 10.1029/98GL50865.

[74] G. L. Siscoe, G. M. Erickson, B. U. O Sonnerup, N. C. Maynard, K. D. Siebert, D. R. Weimer, and W. W. White. Magnetospheric sash dependence on IMF direction. *Geophysical Research Letters*, 28:19211924, 2001. doi: 10.1029/2000GL003784.

[75] J. A. Fedder and J. G. Lyon. The solar wind-magnetosphere-ionosphere current-voltage relationship. *Geophysical Research Letters*, 14:880–883, 1987. doi: 10.1029/GL014i008p00880.

[76] J.A. Fedder and J.G. Lyon. The earths magnetosphere is 165 re long: Self-consistent currents, convection, magnetospheric structure, and processes for northward interplanetary magnetic field. *Journal of G*, 100:3623, 1995.

[77] J. Berchem, A. Marchaudon, M. Dunlop, C. P. Escoubet, J. M. Bosqued, H. Reme, I. Dandouras, A. Balogh, E. Lucek, C. Carr, and Z. Pu. Reconnection at the dayside magnetopause: Comparisons of global mhd simulation results with cluster and double star observations. *Journal of geophysical research*, 113, 2008. doi: 10.1029/2007JA012743.

[78] C. T. Russell, J. A. Fedder, S. P. Slinker, X-W. Zhou, G. Le, J. G. Luhmann, F. Fenrich, M. O. Chandler, T. E. Moore, and S. A. Fuselier.

Entry of the polar spacecraft into the polar cusp under northward imf conditions. *Geophysical Research Letters*, 25:3015–3018, 1998.

[79] E. Priest and T. Forbes. *Magnetic Reconnection: MHD Theory and Applications*. Cambridge University Press, Cambridge, 2000.

[80] W. I. Axford and C. O. Hines. A unifying theory of high-latitude geophysical phenomena and geomagnetic storms. *Canadian Journal of Physics*, 39:1433, 1961.

[81] N. Scopke, G. Paschmann, G. Haerendel, B. U. O. Sonnerup, S. J. Bame, T. G. Forbes, J. E. W. Hones, and C. T. Russell. Structure of the low-latitude boundary layer,j. geophys. res., 86, 2099-, 1981. *Journal of geophysical research*, 86:2099, 1981.

[82] F. J. Rich and M. Hairston. Large-scale convection patterns observed by dmsp. *Journal of geophysical research*, 99:3827–3844, 1994.

[83] P.T. Newell and C. Meng. Hemispherical asymmetry in cusp precipitation near solstices. *Journal of Geophysical Research*, 93:2643–2648, 1988. doi: 10.1029/JA093iA04p02643.

[84] P. T. Newell, W. J. Burke, C.-I. Meng, E. R. Sanchez, and M. E. Greenspan. Identification and observations of the plasma mantle at low altitude. *Journal of Geophysical Research*, 96(A1):3545, 1991. doi: 10.1029/90JA01760.

[85] Newell, P. T. and Feldstein, Y. I. and Galperin, Y. I. and Meng, C.-I. Morphology of nightside precipitation. *Journal of Geophysical Research*, 101(A5):10,73710,748, 1996.

[86] P. T. Newell, Y. I. Feldstein, Y. I. Galperin, and C.-I. Meng. Erratum: "Morphology of nightside precipitation" by Patrick T. Newell, Yasha I.

Feldstein, Yuri I. Galperin, and Ching-I. Meng. *Journal of Geophysical Research*, 101:17419–17422, August 1996. doi: 10.1029/96JA02055.

[87] T. Sotirelis and P. T. Newell. Boundary-oriented electron precipitation model. *Journal of Geophysical Research*, 105(A8):1865518673, 2000. doi: 10.1029/1999JA000269.

[88] Kan Liou. Polar ultraviolet imager observation of auroral breakup. *Journal of Geophysical Research*, 115:A12219, 2010. doi: 10.1029/2010JA015578. URL `http://onlinelibrary.wiley.com/doi/10.1029/2010JA015578/abstract`.

[89] J. F. Carbary, T. Sotirelis, P. T. Newell, and C.-I. Meng. Auroral boundary correlations between UVI and DMSP. *Journal of Geophysical Research*, 108(A1):1018, 2003. doi: 10.1029/2002JA009378. URL `http://www.agu.org/pubs/crossref/2003/2002JA009378.shtml`.

[90] R.W. Eastes, R.E. Daniell, and F.J. LeBlanc. Coincident ultraviolet imager and energetic particle sensor observations of the continuous electron aurora. *Journal of Atmospheric and Solar-Terrestrial Physics*, 62:927–934, 2000. doi: 10.1016/S1364-6826(00)00078-X.

[91] K. B. Baker and S. Wing. A new magnetic coordinate system for conjugate studies at high latitudes. *Journal of Geophysical Research: Space Physics*, 94:9139–9143, 1989. doi: 10.1029/JA094iA07p09139.

[92] P. D. Boakes, S. E. Milan, G. A. Abel, M. P. Freeman, G. Chisham, B. Hubert, and T. Sotirelis. On the use of IMAGE FUV for estimating the latitude of the open/closed magnetic field line boundary in the ionosphere. *Annales Geophysicae*, 26:2759–2769, 2008. doi: 10.5194/angeo-26-2759-2008. URL `http://www.ann-geophys.net/26/2759/2008/angeo-26-2759-2008.html`.

[93] N. Longden, G. Chisham, M. P. Freeman, G. A. Abel, and T. Sotirelis. Estimating the location of the open-closed magnetic field line boundary from auroral images. *Annales Geophysicae*, 28:1659–1678, 2010. doi: 10.5194/angeo-28-1659-2010. URL `http://www.ann-geophys.net/28/1659/2010/angeo-28-1659-2010.html`.

[94] H. U. Frey, S. B. Mende, V. Angelopoulos, and E. F. Donovan. Substorm onset observations by IMAGE-FUV. *Journal of Geophysical Research*, 109:A10304, 6 PP., 2004. doi: 10.1029/2004JA010607.

[95] G. Chisham and M. P. Freeman. A technique for accurately determining the cusp-region polar cap boundary using SuperDARN HF radar measurements. *Annales Geophysicae*, 21:983–996, 2003. doi: 10.5194/angeo-21-983-2003. URL `www.ann-geophys.net/21/983/2003/`.

[96] S.I. Akasofu, C. Meng, and D.S. Kimball. Dynamics of aurora, iv, polar magnetic substorms and westward traveling surges. *Journal of Atmospheric and Terrestrial Physics*, 28:489–496, 1966. doi: 10.1016/0021-9169(66)90058-4.

[97] T. H. Morse and G. J. Romick. The fluctuation and fading of auroral arcs preceding auroral substorm onsets. *Geophysical Research Letters*, 9:1065–1068, 1982. doi: 10.1029/GL009i009p01065.

[98] W. A. Bristow and P. Jensen. A superposed epoch study of SuperDARN convection observations during substorms. *Journal of Geophysical Research*, 112(A06232):A06232, 2007. doi: 10.1029/2006JA012049.

[99] C. I. Meng and S. I. Akasofu. The relation between the polar cap auroral arc and the auroral oval arc. *Journal of Geophysical Research: Space Physics*, 81:4004–4006, 1976. doi: 10.1029/JA081i022p04004.

[100] R. K. Elsen, R. M. Winglee, J. F. Spann, G. A. Germany, M. Brittnacher,

and G. K. Parks. The auroral oval boundaries on january 10 1997: A comparison of global magnetospheric simulations with UVI images. *Geophysical Research Letters*, 25:2585–2588, 1998. doi: 10.1029/98GL01066.

[101] M. Brittnacher, M. Fillingim, G. Parks, G. Germany, and J. Spann. Polar cap area and boundary motion during substorms. *Journal of Geophysical Research: Space Physics*, 104:12251–12262, 1999. doi: 10.1029/1998JA900097.

[102] G.A. Germany, J. F. Spann, G. K. Parks, M. J. Brittnacher, R. Elsen, L. Chen, D. Lummerzheim, and M. H. Rees. *Auroral observations from the Polar Ultraviolet Imager (UVI), in Geospace Mass and Energy Flow: Results from the International Solar-Terrestrial Physics Program*, volume 104. American Geophysical Union, Washington, D. C., 1998. doi: 10.1029/GM104p0149.

[103] J. P. Heppner and N. C. Maynard. Empirical high-latitude electric field models. *Journal of Geophysical Research: Space Physics*, 92:4467–4489, 1987. doi: 10.1029/JA092iA05p04467.

[104] J. M. Ruohoniemi and R. A. Greenwald. Observations of imf and seasonal effects in high-latitude convection. *Geophysical Research Letters*, 22:1121–1124, 1995. doi: 10.1029/95GL01066.

[105] J. M. Ruohoniemi and R. A. Greenwald. Dependencies of high-latitude plasma convection: Consideration of interplanetary magnetic field, seasonal, and universal time factors in statistical patterns. *Journal of Geophysical Research: Space Physics*, 110:A09204, 2005. doi: 10.1029/2004JA010815.

[106] S. E. Milan, M. Lester, S. W. H. Cowley, K. Oksavik, M. Brittnacher, R. A. Greenwald, G. Sofko, and J.-P. Villain. Variations in the polar cap area during two substorm cycles. *Annales Geophysicae*, 21

(5):1121–1140, 2003. doi: 10.5194/angeo-21-1121-2003. URL http://www.ann-geophys.net/21/1121/2003/.

[107] S. E. Milan, M. Lester, S. W. H. Cowley, and M. Brittnacher. Dayside convection and auroral morphology during an interval of northward interplanetary magnetic field. *Annales Geophysicae*, 18(4):436–444, 2000. doi: 10.1007/s00585-000-0436-9. URL http://www.ann-geophys.net/18/436/2000/.

[108] S.E. Milan and M. Lester. Interhemispheric differences in the HF radar signature of the cusp region: A review through the study of a case example. *Advance Polar Upper Atmospheric Research*, 15:159–177, 2001.

[109] T. K. Yeoman, P. G. Hanlon, and K. A. McWilliams. A statistical study of the location and motion of the HF radar cusp. *Annales Geophysicae*, 20:275–280, 2002. doi: 10.5194/angeo-20-275-2002.